RELATING DEEP MAGMATIC PROCESSES TO ERUPTIVE BEHAVIOR AT ARC

VOLCANOES THROUGH AN ANALYSIS OF DEEP SEISMICITY

By

Ophelia A. George

RECOMMENDED: _____

_____

_____
Advisory Committee Chair

_____
Chair, Department of Geology and Geophysics

APPROVED: _____
Dean, College of Natural Science and Mathematics

_____
Dean of the Graduate School

_____
Date

RELATING DEEP MAGMATIC PROCESSES TO ERUPTIVE BEHAVIOR AT ARC

VOLCANOES THROUGH AN ANALYSIS OF DEEP SEISMICITY

A

THESIS

Presented to the Faculty

of the University of Alaska Fairbanks

in Partial Fulfillment of the Requirements

for the Degree of

MASTER OF SCIENCE

By

Ophelia George

Fairbanks, Alaska

December 2010

ABSTRACT

In this thesis, the seismicity at depths greater than 15 km beneath two sets of volcanic centers, the Klyuchevskoy Volcanic Group (KVG), Russia and Mount Spurr, Alaska is examined. In both regions, a pulsing pattern of deep seismicity is observed with many cycles following eruptive activity or periods of unrest. The bulk of the seismicity beneath the KVG is comprised of long-period events many of which share a similar appearance. Cross correlation of the waveforms for events occurring between 12/24/2007 and 12/31/2008 show a number of event families occurring over long time spans. New relative locations for these families which better constrain their spatial extent are derived.

The pulsing pattern of seismicity seen here is in close keeping with the expected cyclic nature of melt segregation which occurs as melt leaves the site of generation and ascends to shallower levels. Based on evidence in the data, a model is proposed whereby melt segregation on the time scales necessary to facilitate eruptions is attributable to a pressure response in the deep system induced by the removal of material in the shallow chamber during an eruptive cycle.

TABLE OF CONTENTS

LIST OF FIGURES

LIST OF TABLES

Page

ACKNOWLEDGEMENTS

I would like to thank Drs Michael West, Douglas Christensen and Stephen McNutt for agreeing to serve on my committee and all their input in making this thesis sound.

I would also like to thank the many colleagues and classmates who provided support and assistance over the course of the last two years

Finally, I would like to dedicate this thesis to my mother, Victoria Matthew, and my brother, Kerwin George, without whose constant sacrifice and support this would not have been possible.

INTRODUCTION

Though recent years have seen much progress in the study of deep seismicity, much remains to be discovered about its causes and its relationship to magmatic systems beneath arc volcanoes. In the Earth's crust, there exists a zone, termed the seismogenic zone, in which seismicity is concentrated. In typical tectonic settings, this zone extends from the surface to a depth of about 15 km but may be significantly shallower in volcanic settings due to repeated heating of the crust by the intrusion of magma. The lower boundary of this zone varies from volcano to volcano but tends to occur between 7 and 10 km (Hasegawa et al., 1993). This cutoff point is believed to mark the brittle-ductile transition zone below which the crust is heated enough such that it is unable to support brittle failure. Given the existence of this zone, the occurrence of deep events at depths of 20 kilometers and greater can be considered anomalous.

These events, however, are fairly common in volcanic settings and tend to be dominantly low-frequency earthquakes. Seismic waves generated at these depths tend to have emergent onset, low-frequency content and extended codas. Such signals have been attributed to fluid migration processes (Chouet, 1996) or as a recent study by Ohmi et al. (2004) showed, due to failure in a fluid saturated gauge zone; evidence for fluid existence and migration at these depths is provided by both geochemical and geophysical research methods.

Geochemical modeling of the generation of andesitic and silicic magmas beneath arc volcanoes by Annen et al. (2006), proposed the existence of a "hot zone" between 20 and 30 km depth. In this model, primary basaltic magmas are emplaced as discrete sills at

30 km or greater in the crust. These magmas may be generated either by decompressional melting of the mantle wedge by subduction induced corner flow or by melting triggered by the release of water-rich fluids from the subducting slab. The hot zone is developed due to the release of heat from the crystallizing sills, which are repeatedly emplaced in the crust over time. Melts eventually segregate out of these sills and ascends to the shallow level magma chambers due to compaction and the buoyancy contrast between the melt and the host rock.

A number of models have been proposed to explain the mechanism by which melt becomes segregated from its zone of generation in the lower crust and ascends to shallower levels. Among them are models by Connolly et al. (1997) and Miller et al. (2003) in which permeability of the lower crust is increased by fluid driven micro-fracturing which creates a network of interconnected cracks. From Connolly's laboratory experiments conducted on muscovite-bearing metaquartzite at pressures of 800 MPa and temperatures of 950 - 1126 K (conditions comparable to those which exist in the lower crust) it was found that melt generated by dehydration melting of water-bearing mineral phases first forms at the multi-grain boundaries. The change in phase from solid to liquid leads to an increase in volume which in turn translates to an increase in fluid pressure. When a critical threshold is reached, randomly oriented cracks are generated which may eventually interconnect. It is then possible for fluids to drain out of these localized nucleation sites and ascend.

Another postulated mechanism of melt segregation is through compaction. As they are subjected to the overburden pressure of the overlying rocks, partially molten

rocks in the lower crust become compressed, forcing out the melts contained within. A 2004 study by Vigneresse showed that compaction alone was not sufficient to drive melt segregation on the time scales required by present day activity and that a component of horizontal shear was also necessary. As a result of the compaction and shear instabilities which develop and interact at these nucleation sites, small amounts of melt escape periodically. This periodicity of melt segregation leads to a cyclical pattern in which cycle frequency is dependent on the amount of heat available for additional melting; periods of melt segregation are alternated with relaxation periods during which melt once again accumulates at these sites. In each cycle of melt segregation, about 5% of the melt present is extracted; overall only about 25% of the total melt is extracted as the number of cycles is limited by the fact that progressive removal of melt results in a stiffening of the crust which hinders further melting.

Though magma ascent is not confined to one particular deformational style, regional and local deformation provides the forces which are necessary for magma to overcome the barrier of the brittle/ductile transition zone. Vigneresse (1995) postulates that magma ascent must take place in a locally extensive near field setting as this provides the least tectonic stress for magma to overcome. That is, despite the volcano being located in a regionally compressive setting, the stress regime immediately surrounding the magma conduit must be tensile to facilitate the ascent of the magma past the brittle/ductile transition.

In addition to the geochemical experimental and modeling studies mentioned above, the idea of deep seated magma chambers has been further corroborated by

geophysical evidence. Wiemer and McNutt (1997) identified a region of high b-values beneath Crater Peak, Alaska at depths of 20-40 km. While the global average for b-values in a typical tectonic setting is about 1, values beneath volcanoes are generally higher due to increased material heterogeneity, pore pressure, heat flux and stress states which are common at volcanoes. All these factors except stress have been shown to increase the b-values (see Mogi (1962) or Scholz (1968) for more on b-value experiments). Therefore, the elevated b-values which were found at these depths beneath Crater Peak can be attributed to conditions near a deep seated magma chamber. Similar evidence for magma storage at depth was provided by 3D tomographic studies in other volcanic regions (Khubunaya et al., 2007; Lees et al., 2007; Hasegawa et al., 1993). Both the studies conducted by Khubunaya et al. (2007) and Lees et al. (2007) showed a shared low-velocity zone between 25 to 40 km beneath the Klyuchevskoy Volcanic Group (KVG) while a similar shared low-velocity zone was found by Hasegawa et al. (1993) beneath the volcanoes of northern Japan. Hasegawa found that deep low-frequency events tended to occur in this low-velocity zone either beneath or within close proximity to active volcanic centers.

Utilizing two rich data sets, it is the primary goal of this study to establish a model which relates the processes at depth to the eruptive cycles at arc volcanoes. Data are acquired from two sets of arc volcanoes, Mount Spurr, Alaska and the KVG. Both are well known for their abundance of deep seismicity and so provided an excellent dataset to further the goals of this study. Power et al. (2004), showed Mount Spurr to have had the highest number of deep events in Alaska and the Aleutians since monitoring of these

volcanoes began in 1989. In the case of the KVG, the Kamchatka Branch for Geophysical Surveys (KBGS), one of the agencies responsible for monitoring these volcanoes, considers deep seismicity to be above background only if the number of events exceeds 30 events/day. Though deep seismicity at Mount Spurr has a much higher occurrence rate than at other Alaskan and Aleutian volcanoes, activity here is a mere fraction of that seen beneath the Klyuchevskoy Group.

Cross correlation analysis and double difference relocations, among other techniques are used to narrow down the potential causes of deep volcanic seismicity by analyzing the spatial distribution, temporal patterns, waveform similarity, spectral characteristics and focal mechanisms. The first two chapters of this thesis will be devoted chiefly to the study conducted on data from the KVG. Chapter 1 gives a detailed description of the datasets used in this study, and the waveforms contained therein. Chapter 2 journeys through the process of winnowing down the dense seismicity cloud to elucidate the fine scale structures buried within. It highlights the process of event location using the Antelope suite of programs, cross correlation analysis and double difference relocation of a small subset of events which show a high degree of similarity. In chapter 3, a brief summary of similar analysis done on the smaller Mount Spurr data set will be described.

The map in figure I.1 highlights the location of both sets of volcanoes which will be analyzed in this study.
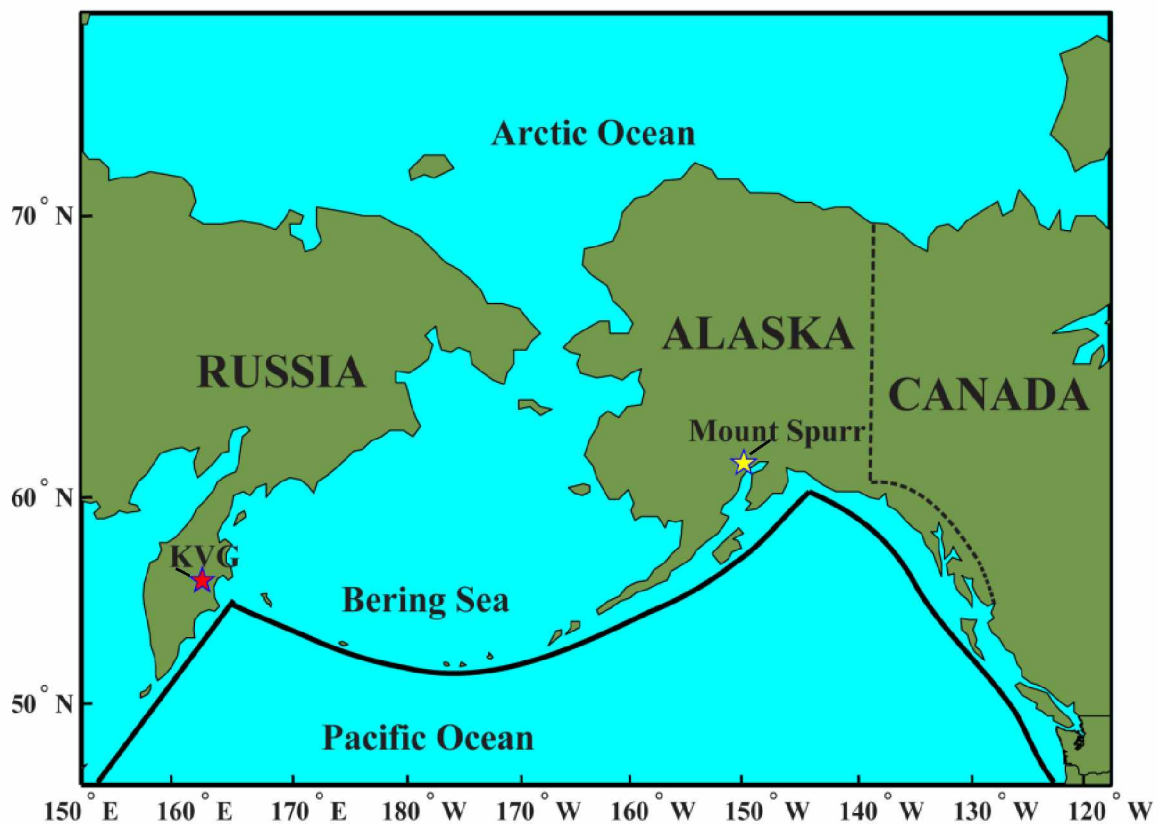
Figure I.1 Map of the northern Pacific indicating the two volcanic regions of interest to this study. The thick black line highlights the location of the Pacific plate boundary which subducts beneath the North American plate in the case of Mount Spurr and the Eurasian plate in the case of the KVG.

Chapter 1 Characterization of deep seismicity beneath the KVG, Kamchatka

1.1 *REGIONAL SETTING*

The data used in this study come from two unique tectonic settings located in the north Pacific. The first and primary data set comes from the Klyuchevskoy Volcano Group (KVG) which is located across the Pacific Ocean from Mount Spurr, the second volcano under study. This group of basaltic to basaltic-andesite stratovolcanoes occupies a unique tectonic setting which is reflected both in their seismicity as well as their geochemical signature. Located in the Central Kamchatka Depression on Russia's Kamchatka Peninsula, just to the west of the Kamchatka-Aleutian Junction, these young cones are marked by a high occurrence of deep events as well as a magmatic chemistry which points to melting of the subducting oceanic slab (Portnyagin et al., 2005).

Such a phenomenon is not usually seen except in the case of very young subducting plates and is taken as an indication of plate rejuvenation of the ~ 90 my Pacific Plate in this section (Manea and Manea, 2007; Davaille and Lees, 2004). The rejuvenated plate behaves as a much younger plate would due to a thermal restructuring as a result of additional heating such as impact by a mantle plume. Melting of the subducting slab in this region is further enhanced by the detachment of a segment of the plate and the resulting mantle flow along its edge just north of the Kamchatka-Aleutian Junction (Levin et al., 2002; Nikulin et al., 2010). A schematic diagram of the Kamchatka-Aleutian Junction taken from Nikulin et al. (2010) is shown in figure 1.1 which illustrates the features described above. In the figure, the term KUMA refers to the

proposed subduction zone migration related to the detachment of the slab; the region labeled (1) is the area from which the slab detached.
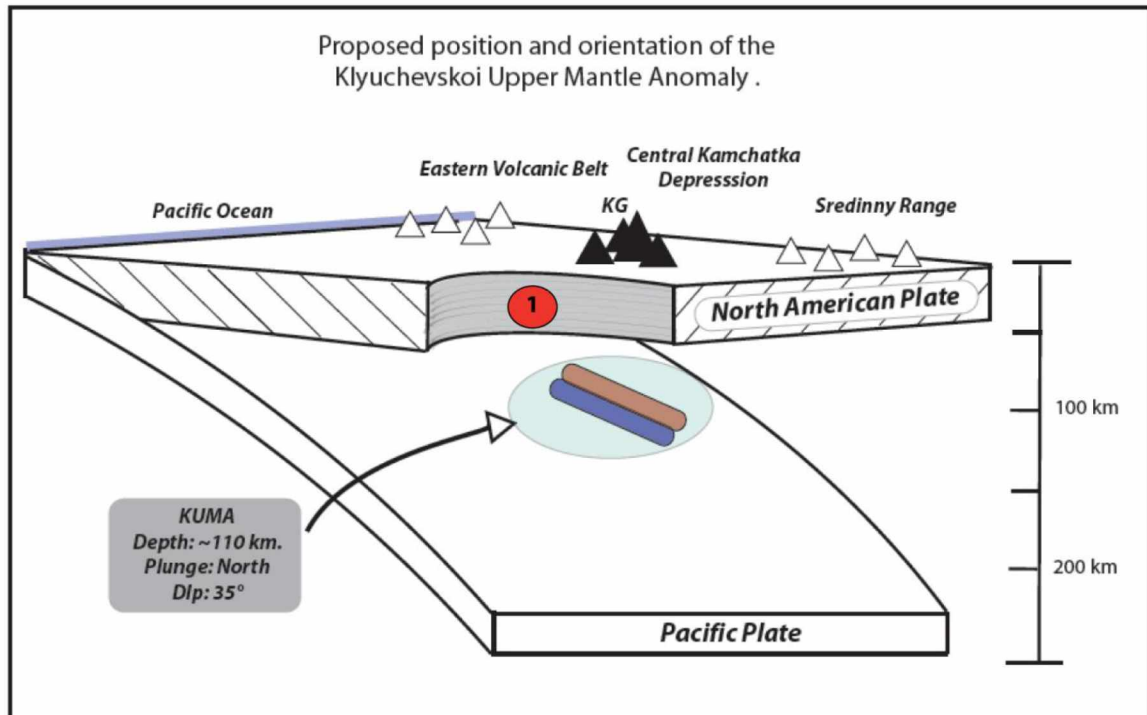
Figure 1.1 Schematic diagram of the Kamchatka-Aleutian junction subduction zone (taken from Nikulin et al. (2010) figure 4). The location of the KVG is shown by the black triangles; the region labeled 1 in the figure is the position from which the slab detached while the arrow points to the upper mantle anomaly associated with this detachment.

1.2 THE DATA

Starting in 2006, a network of broadband, three component seismometers was deployed on Bezymianny Volcano, one of the KVG volcanoes, as part of the Partners in International Research and Education (PIRE) project in Kamchatka. This volcano was chosen because on March 30th 1956, it underwent a sector collapse and subsequent lateral blast similar to what would be seen at Mount St Helens 24 yrs later. The frequency of eruptions at this and other volcanoes in the group make them ideal candidates for investigating possible future behavior of Mt St Helens and other similar volcanoes. Data

from this deployment have been collected over the course of several summer field seasons and are currently being used in a number of different studies. In this study, waveform data from these stations are supplemented with catalog data from the Kamchatka Branch for Geophysical Surveys (KBGS) which includes event locations and origin times as well as P and S wave arrival times for events occurring beneath the KVG. The PIRE network deployed on Bezymianny along with some of the KBGS stations in close proximity is shown in figure 1.2.
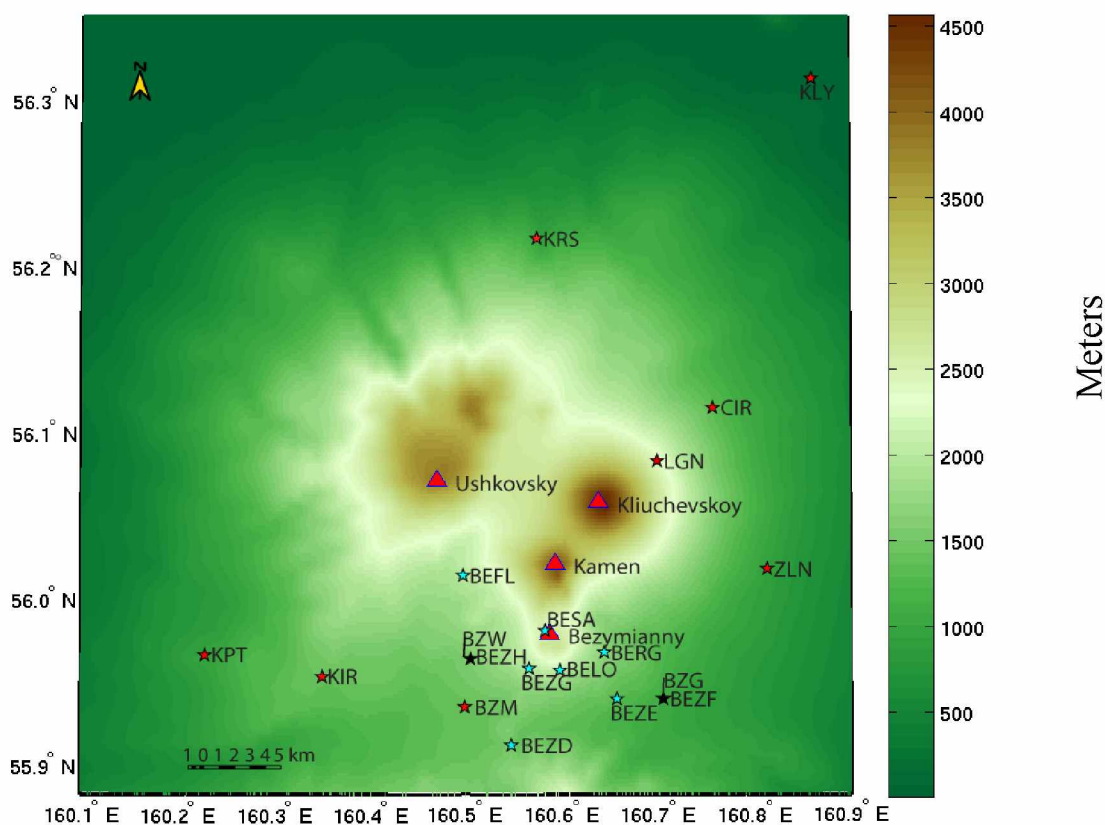
Figure 1.2 Map of operational stations on and around the KVG during the study period. Blue stars indicate PIRE stations, red stars are KBGS operated stations while black stars indicate collocated PIRE and KBGS stations. Volcanoes are indicated by red triangles.

1.3 *ANATOMY OF DEEP LOW FREQUENCY EARTHQUAKES*

1.3.1 Waveform Characteristics

In general, low-frequency earthquakes tend to be dominated by low frequencies, typically less than 5 Hz (Chouet, 1996; Neuberg et al., 2000). The emergent onsets of these earthquakes are usually followed by a long, almost monochromatic coda. The low frequency events in this data set tend to be similar to this description; beneath the KVG, the majority of the deep seismicity catalog is comprised of low-frequency events with a duration between 20 to 25 seconds, emergent onsets, dominant frequencies around 2 Hz and an extended coda following the P and S waves. The term deep long period (DLP) will be used to refer to these events throughout the text in keeping with current terminology.

In a typical event, the P waves last for about 1.5 – 2 seconds and are comprised of 2-3 prominent peaks with maximum peak-to-peak ground displacement amplitude between 5 – 110 nm. Such P waves are seen not only from one event to the next on a given station but across the entire PIRE network; amplitudes tend to remain relatively constant across the network as the inter-station separation is small compared to the event to station distances for these events. Higher amplitude values than the average mentioned above are associated with the few larger magnitude events which make up this deep event catalog. In figure 1.3 the distribution of ground displacement P wave amplitudes for a subset of events is shown both as a function of distance from station BEZD and their relative abundance in the catalog. As can be seen from this figure, few events have ground displacement values which exceed 20 nm (less than 20%).
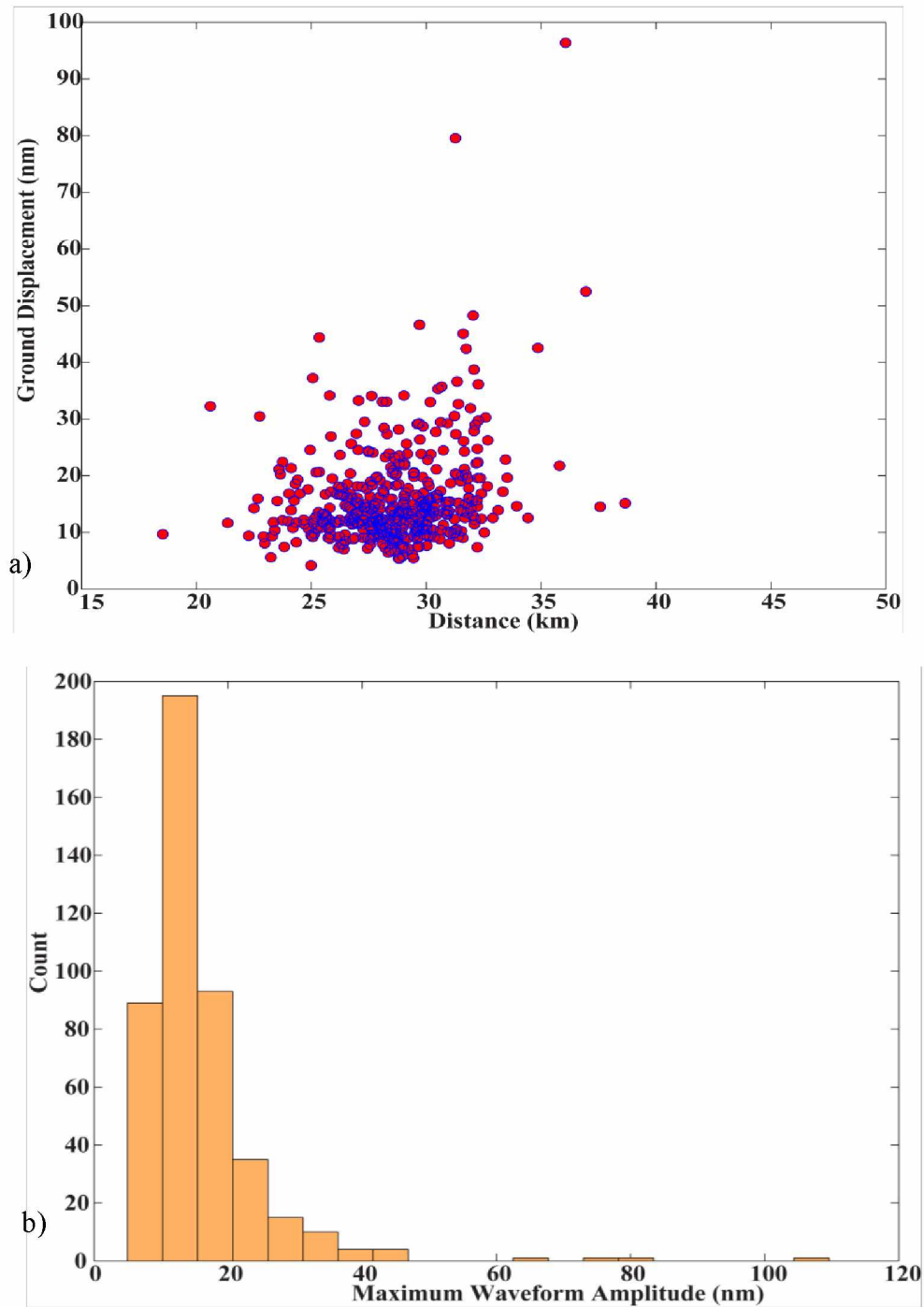
Figure 1.3 Plot of ground displacement amplitude distribution for a subset of KVG DLPs. (a) The distribution of amplitudes with distance is shown - very few of these events produce a ground displacement which exceeds 20 nm and tend to be concentrated at a distance of about 25-33 km. (b) As in (a), the histogram shows that most events in this subset produce a ground displacement of less than 20 nm.

The S waves which make up these DLPs contain some significant differences from those recorded in typical tectonic earthquakes. Amplitudes recorded for these waves are not much larger than those of the P wave portion of the event and typically range between 5 – 120 nm. Dominant frequencies are also about 2 Hz but where the P waves show marked similarity, S waves commonly lack coherence. The duration of these waveforms are typically about 2.5 s except on stations BERG and BEZE whose S waves are about 1.5 seconds and show a high degree of similarity to their P waves. The body waves described above is typically followed by a low frequency wave train which has durations between 16 and 20 seconds. A characteristic deep event recorded here is shown in figure 1.4.
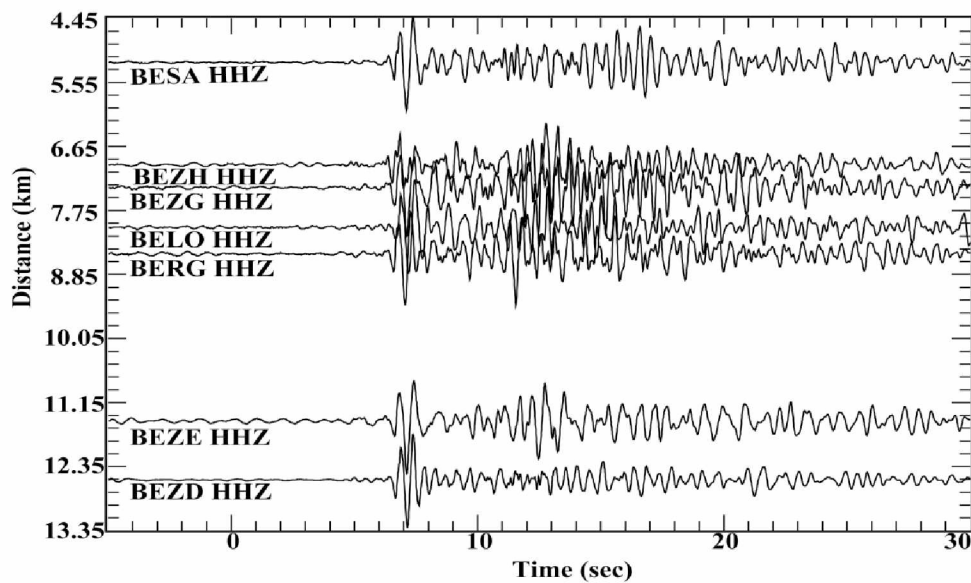
Figure 1.4 A typical deep event occurring beneath the KVG as recorded by stations in the PIRE network. The P waves recorded here show marked similarity across the network while there is a lack of coherence in the S waves. S-P time of ~ 3 seconds as well as the almost simultaneous first arrivals on all stations as seen here is also common for most of the events in this deep data set. The y axis gives distance from the source to the station.

As noted above, a common feature of the deep events beneath the Klyuchevskoy group is the marked similarity between individual events which can be seen across the PIRE network. Waveforms recorded here commonly have similar amplitudes, frequency contents and S-P times of 3-5 seconds. Such patterns validate the classification of these events as low-frequency earthquakes as they point towards the waveform structure seen being caused by source effects as opposed to the diminishing of high frequency energy due to attenuation. Where the low-frequency content of a waveform is due to attenuation, there is usually a larger degree of variability seen in the waveforms between stations and from one event to the next.

1.3.2 Comparing deep long-period events to other seismicity at these volcanoes

The deep events beneath the KVG produce distinct waveforms which are instantly separable from other seismic signals produced here based on visual inspection. Shallow high-frequency events at the KVG are more variable in their appearance. These shallow events tend to show little similarity across the network, have variable S-P times, distinctly different first arrival times from one station to the next and a broadband spectral signal. A sample record section for a shallow KVG event is shown in figure 1.5 which illustrates these points. In figure 1.6, a spectrogram for this event recorded on station BEZD (a) is shown along with a DLP recorded on the same station (b). The shallow event has spectral energy between 1-7.5 Hz while in the DLP event, the bulk of the energy is focused at about 2 Hz.
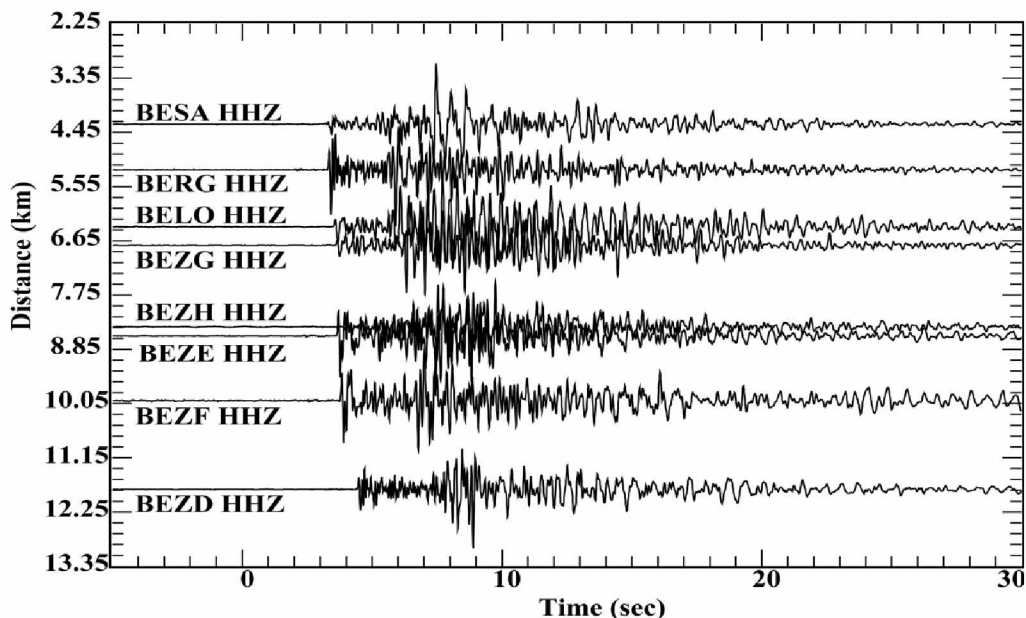
Figure 1.5 Record section of a shallow high-frequency event recorded on the PIRE network. This section shows noticeable differences in the arrival times from one station to the next as well as marked differences in the S-P times - the same is not true for the deep events as shown in figure 1.4.
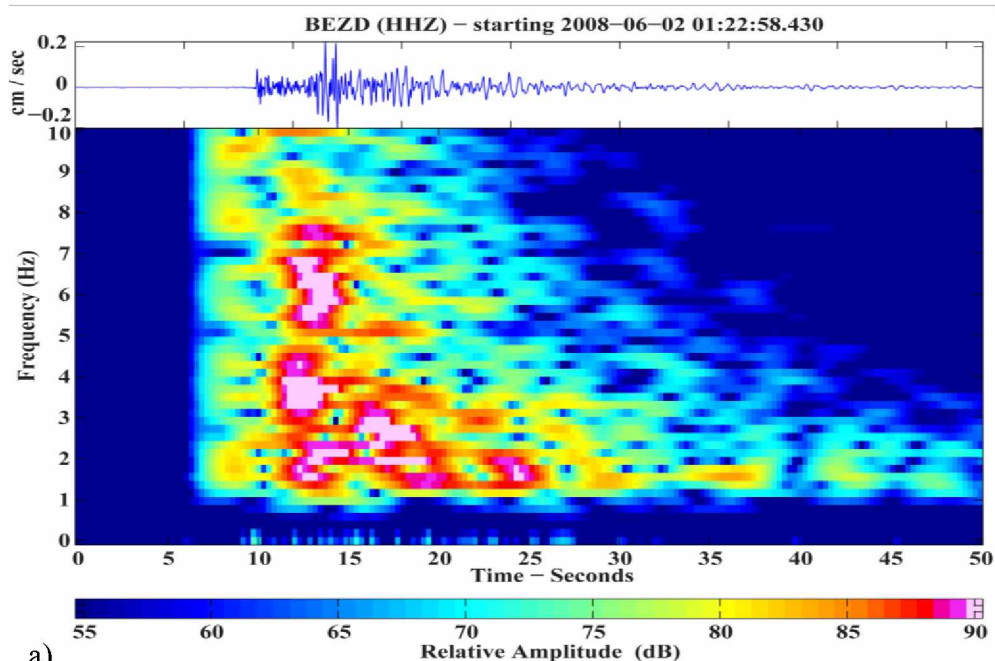
Figure 1.6 Spectrograms of different event classes beneath the KVG. (a) A shallow high-frequency event – the onset of this event shows peak spectral amplitudes over a broad range of frequencies followed by a long low-frequency coda. (b) The DLP shown here has most of its energy concentrated at about 2 Hz.

BEZD (HHZ) – starting 2008–03–19 03:38:09.490

b)
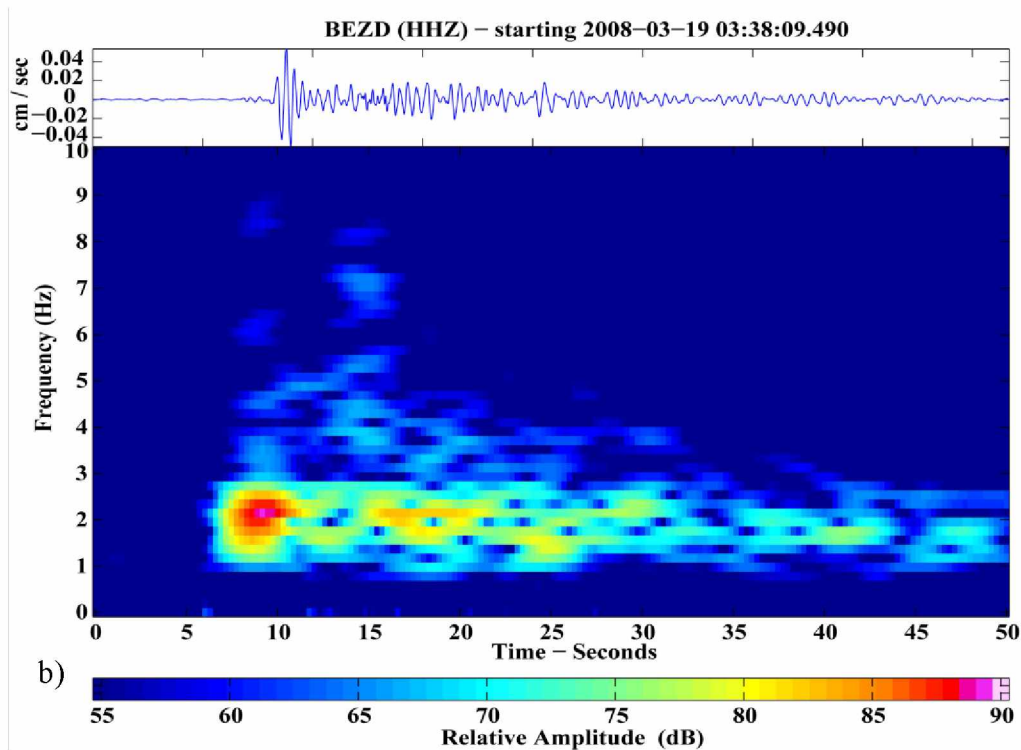
Figure 1.6 continued

1.3.3 Event magnitudes

As is typical of seismic events occurring beneath volcanoes, the deep earthquakes recorded in these data sets are comprised mainly of small events with M_L magnitudes ranging from 1 to 3.5. Though there are a few large events in the set, the average magnitudes recorded for these events are about 1 in both of the settings in this study. The magnitudes quoted here are converted from original KBGS energy classes which are not based on the Richter or M_L magnitude scale but instead on the $\log_{10}$ of the energy of the maximum amplitude S wave (Gorelchik and Storcheus, 2001). To convert from the KBGS magnitude scale (K_s) to the M_S (M_S is the magnitude calculated from maximum surface wave amplitude) scale the following relation is used (Fedatov et al., 2010):

$$M_S = \frac{K_s - 4.6}{1.5}$$
(1.1)

From here the values can be converted to Richter magnitudes (M_L) by the following relation:

$$M_L = \frac{M_S + 3.2}{1.45}$$ (1.2)

These low magnitudes are well in keeping with the real amplitudes measured at stations located on Bezymianny volcano. For instance, deep events located during 2008 typically have P and S wave ground displacement amplitudes between 5 - 110 nm. S/P amplitude ratios for most events hover close to 1.2 and in a few cases, P wave amplitude values exceed those of the S waves for a particular event. Departures from these mean values correspond to the odd event of larger magnitudes (2 M_L and above).

The M_L magnitude scale which is used in this study was developed by Charles Richter in the 1930s and is based on ground displacements. M_L magnitudes can be calculated by the following equation (Lay and Wallace, 1995):

$$M_L = \log_{10} A - 2.48 + 2.76 \log_{10} \Delta$$ (1.3)

Where A is the maximum amplitude of ground displacement in μm and Δ is an epicentral distance correction in km. Using the station location for BEZD coupled with KBGS catalog locations for deep events during the 2007-2008 period and the maximum amplitudes shown in figure 1.3, the magnitude range recorded for that station can be calculated by the above equation. The calculated M_L magnitudes for these events range from 1.7 to 3.1 which is about 0.8 units higher than the converted K_s values. A comparison of the two magnitudes calculated for events from December 2007-2008 is shown in figure 1.7 and 1.8. In figure 1.7 a scatter plot of converted KBGS versus

magnitudes calculated on BEZD is shown while plots (a) and (b) in figure 1.8 were generated from the converted KBGS magnitudes and values calculated from maximum S wave amplitudes recorded on PIRE station BEZD respectively.
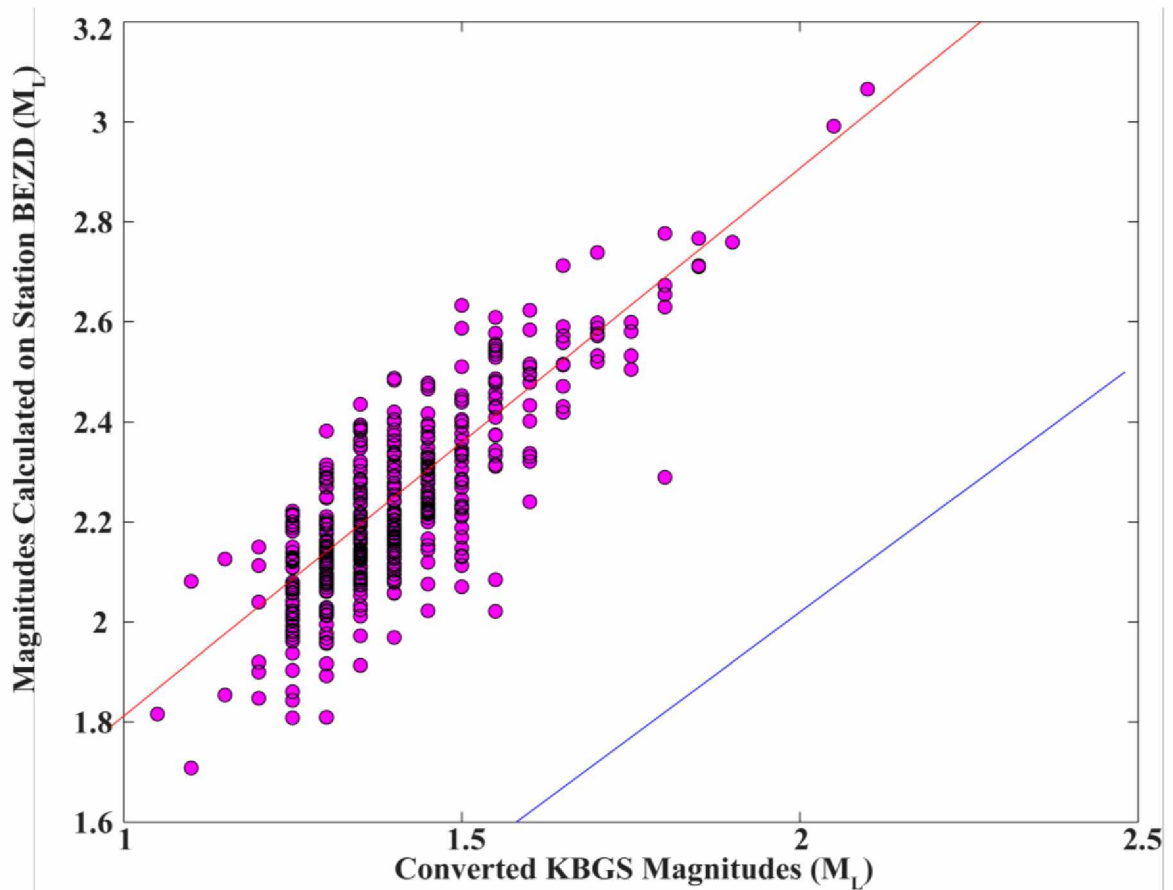
Figure 1.7 Comparative magnitude plot for deep events beneath the KVG during 2008. Converted KBGS magnitudes are plotted against those calculated using station BEZD. While the best fit line for this data (red) closely mirrors the one to one trend line (blue), the BEZD magnitudes tend to run 0.8 units higher than the converted KBGS values.
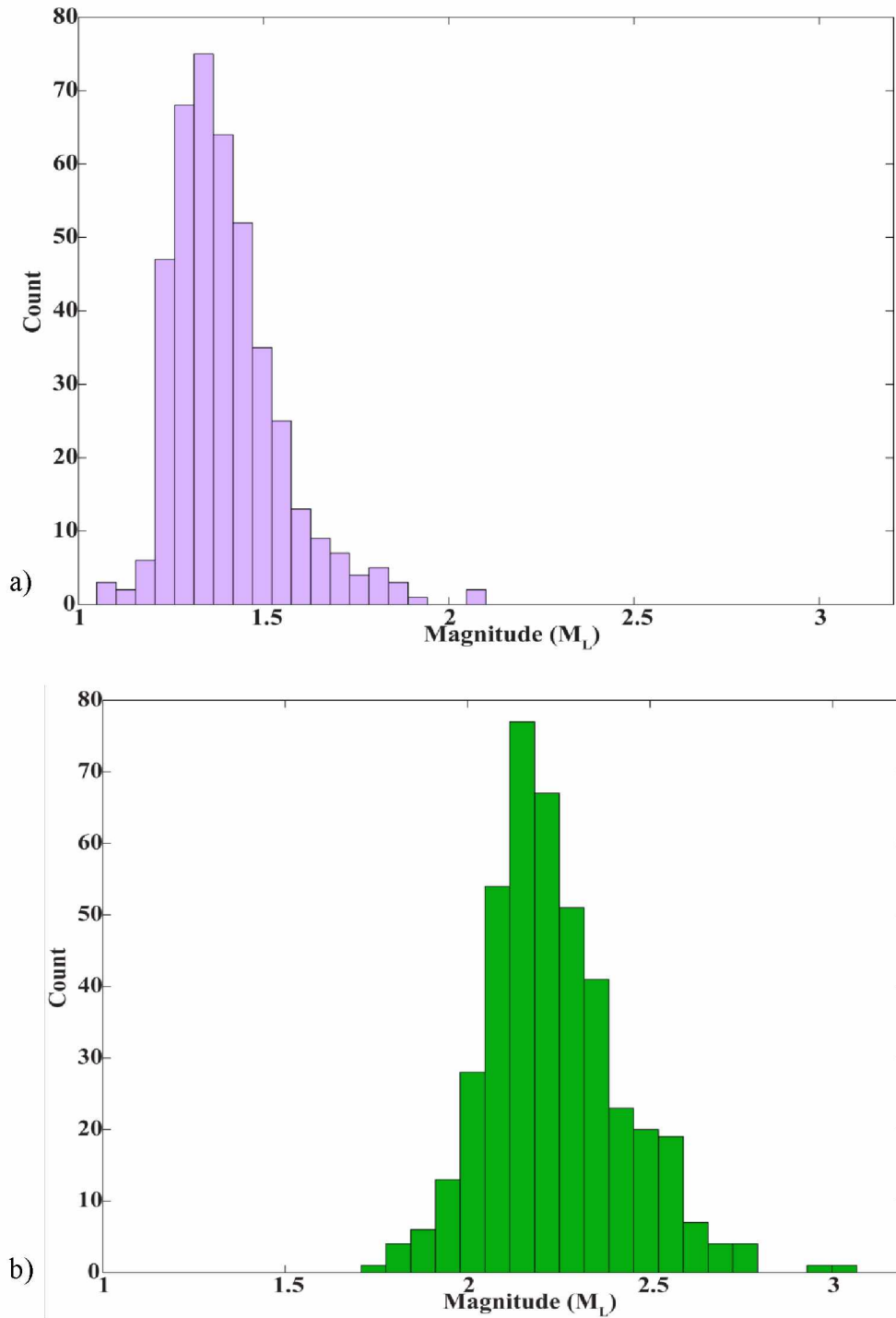
Figure 1.8 Magnitude distribution histograms for the events shown in figure 1.7. (a) Shows the magnitude distribution for values converted from KBGS energy classes. (b) Magnitude distribution calculated using station BEZD. The magnitudes calculated on BEZD show a normal distribution centered about 2.2 while the KBGS values are skewed towards smaller values.

From the plots above, a notable difference between the BEZD calculated values and those converted from the KBGS catalog can be seen. In addition to the fact that BEZD values run 0.8 units higher than the converted ones, BEZD shows a more normal magnitude distribution and values are centered about 2.2 M_L while KBGS values tend to be skewed towards lower values. While it should be noted that catalog magnitude values are the averages of multiple station values and not the result of a single station calculation, a number of other factors may be causing this variation in values. Foremost among these factors are 1) the conversion equations used to derive the M_L magnitudes from KBGS energy classes, 2) site responses, and 3) the distance corrections applied.

Given that only one station was used in the calculation of the PIRE magnitudes above, these values are likely to be largely influenced by particular biases of that station. Signals at this station may be amplified or diminished by conditions which are site specific and would lead to an alteration of the actual event magnitudes. Distance corrections are based on the event locations therefore errors in those locations will bias the calculated magnitudes. Event locations will be addressed further in later chapters.

1.4 PATTERNS OF DEEP SEISMICITY

One of the notable temporal features in both of the study regions is a pulsating pattern of seismicity. Deep events here do not occur continuously, but in large clusters of events which occur daily for a few months and then shut off for months to years (Mount Spurr) before starting up again. A ten year time-depth plot of seismicity beneath the KVG is shown in figure 1.9 along with explosive eruptions of both Bezymianny Volcano (red triangles) and Klyuchevskoy (black triangles).
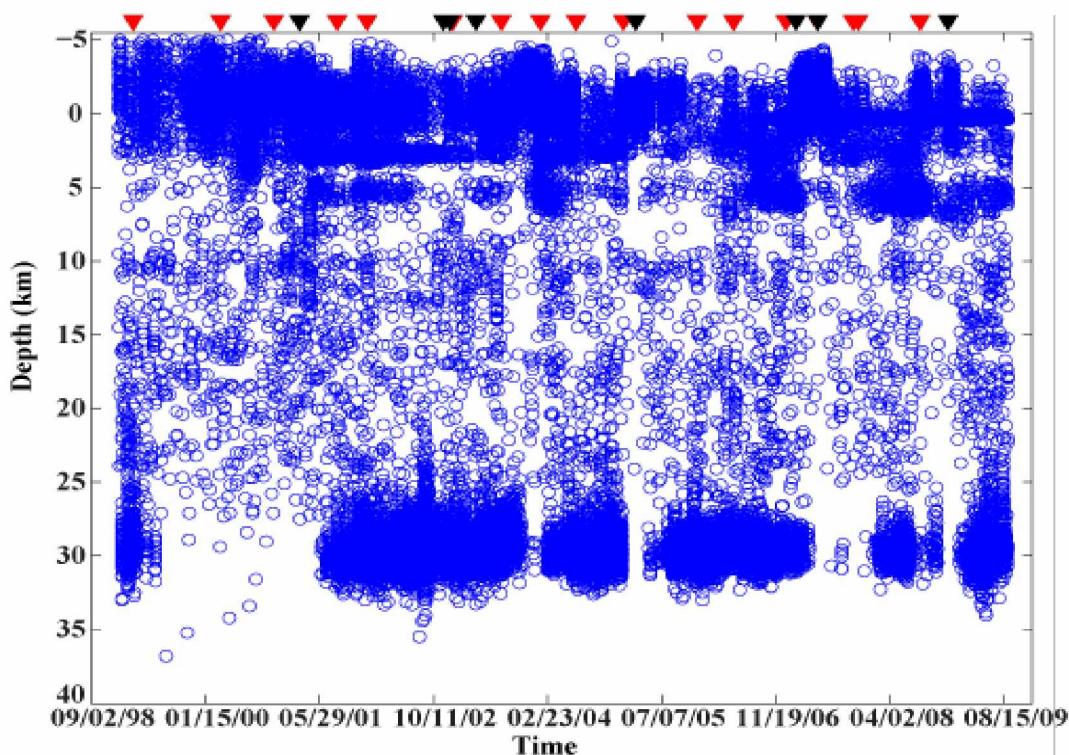
Figure 1.9. Time-depth plot of seismicity beneath the KVG from 1999-2009 (reproduced from the KBGS catalog). Three noteworthy zones of seismicity are prominent in this region at depths of ~ 25-30 km, ~5 km beneath sea level and shallow summit level activity between -5 and 4 km. A large number of eruptions have occurred during lulls in activity at 30 km. Red and black triangles indicate explosive eruptions of Bezymianny and Klyuchevskoy Volcano respectively.

Beneath the KVG, there are three prominent depths at which seismic events are located. Deep events in this region are clustered at ~ 30 km with sparse seismicity occurring between this cluster and the next prominent set of events at 5 km. The third cluster of events occurs at shallow depths (-5 to 4 km) beneath the summits and tends to be associated with eruptive activity.

There is a close correlation between the occurrence of events at depths of about 30 km and those occurring at depths of about 5 km; on many occasions during the period shown in figure 1.9, seismic lulls at a depth of 30 km coincide with sparsity of activity at 5 km. The bulk of seismic activity at this time is instead concentrated at shallow depths

beneath the summit. It should be noted as well, that the majority of eruptions at both Bezymianny and Klyuchevskoy occur during these periods of low seismicity at these depths. It is therefore plausible that the pulsing pattern of deep seismicity is not a true manifestation of some volcanic process but rather, an overshadowing of those signals by an increase in shallow activity. Increases in the number of rock falls coupled with an increase in tremor activity which commonly precedes many volcanic eruptions could easily mask small events such as those that occur at depths of 30 km. These deep events span a magnitude range of 1- 3.5 M_L with the majority of events having magnitudes less than 1.5 M_L.

When the seismicity at depths of 15 km and greater for the period 2006 – 2009 is plotted on a cumulative event plot, the hiatuses in activity are readily apparent (figure 1.10). Each break in activity is followed by a reemergence of seismicity which has a distinctly different rate than the period before it. These rate changes may be attributed to changes in the seismic network or to variations in the actual source processes at depth. The plots in figure 1.11 – 1.13 show a comparison of the seismicity rates per year for each of the periods highlighted in 1.10; rate changes as high as 61% were calculated between the period 2006-2007 (green box) and 2008 (yellow box). When the period 2006-2007 is compared with that in 2009 (blue box), a 43% change in seismicity rate is measured. While the magnitude of completeness, the smallest magnitude earthquake above which the catalog detections are considered reliable, for the catalog at this depth does not change during any of the periods in question there is a significant difference in the number of small magnitude earthquakes (M_L 2 or less) which are recorded in each

period. Many factors may contribute to this occurrence including an increase in the number of small earthquakes, a decrease in background noise levels which could overshadow smaller events or an increase in network coverage and functionality.
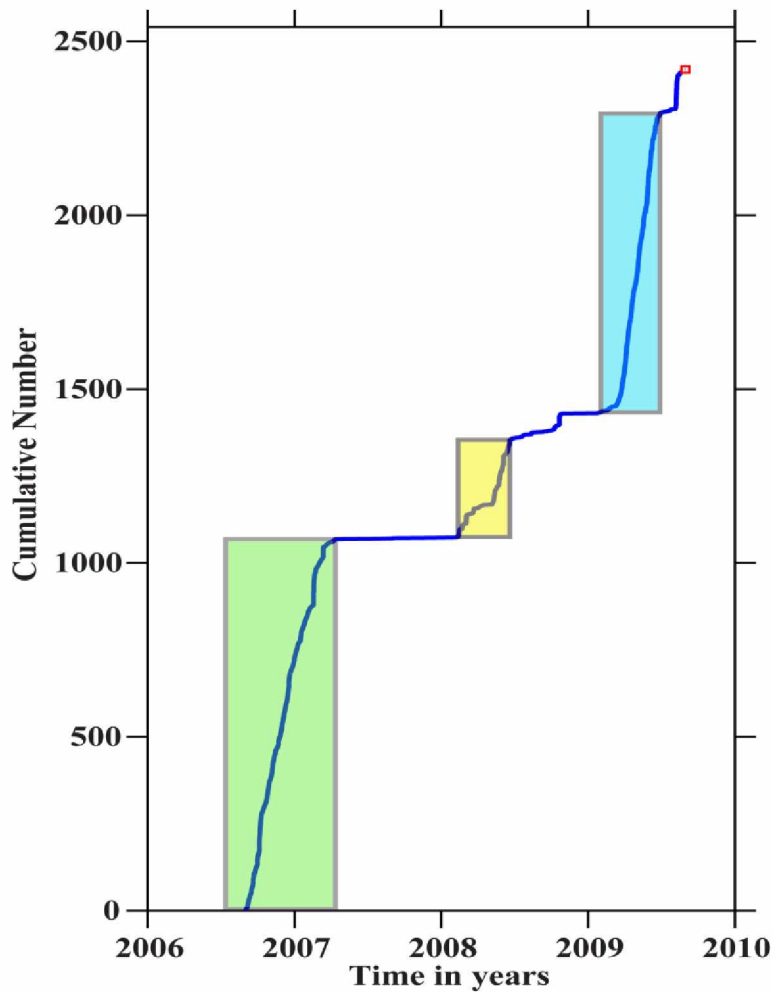
Figure 1.10 Cumulative deep seismicity beneath the KVG (2006-2009). The plot shows the cumulative seismicity with time – there are 3 noteworthy periods of deep seismicity on this plot: 2006-2007 (green box), 2008 (yellow box) and 2009 (blue box) each of which have distinct rates from each other.
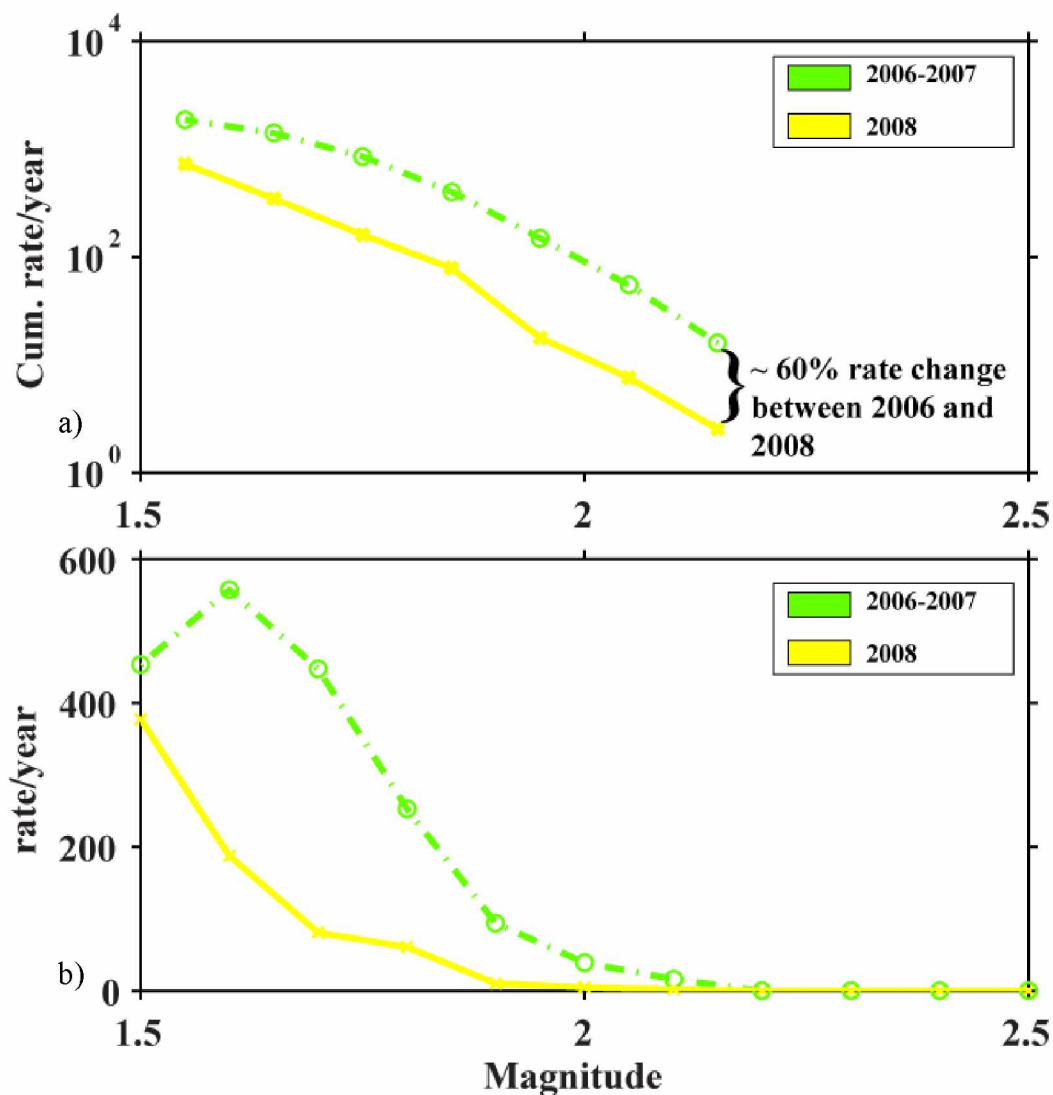
Figure 1.11 Seismicity rate comparisons between events in the period 2006-2007 and 2008. (a) The magnitudes from each energy class are added to those in the class above to create a plot of the cumulative rate of events/yr. There is an approximately 60% rate difference between the cumulative rate/year in 2008 and that in 2006-2007. (b) Same as in (a) except magnitudes are not added to the higher classes; there is a significant decrease in the number of small events recorded during 2008 compared to the 2006-2007 period.
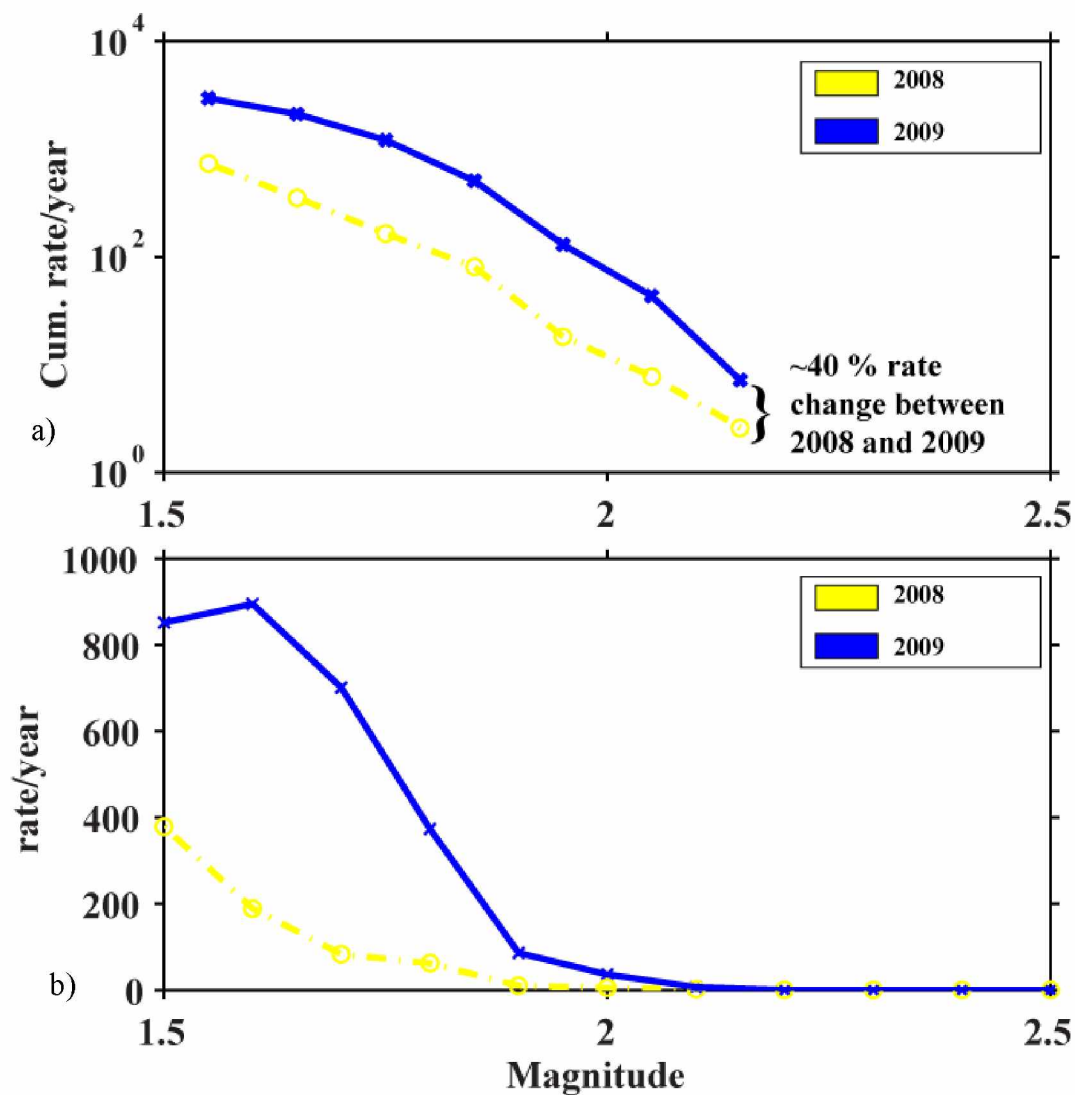
Figure 1.12 Seismicity rate comparisons between events in 2008 and in 2009. (a) The magnitudes from each energy class are added to those in the class above to create a plot of the cumulative rate of events/yr. There is an approximately 40% rate difference between the cumulative rate/year in 2008 and that in 2009. (b) Same as in (a) except magnitudes are not added to the higher classes; as in figure 1.11, the number of small events recorded in 2008 is much smaller than in 2009.
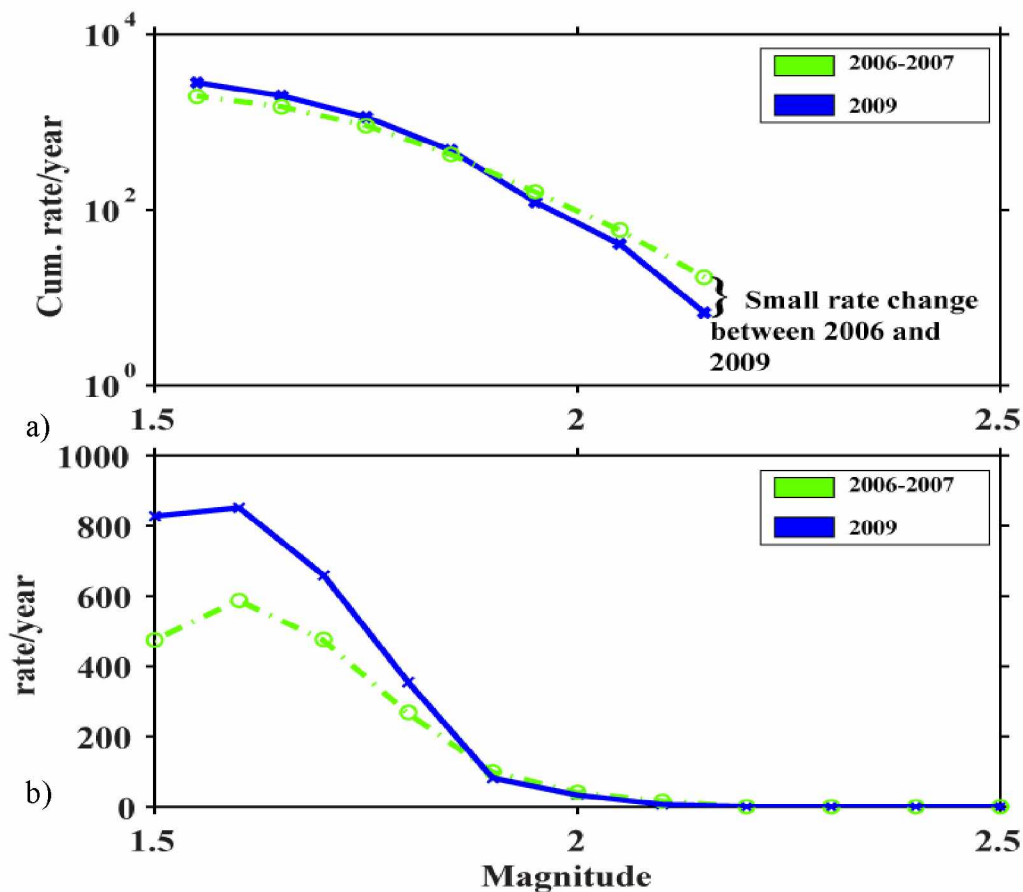
Figure 1.13 Seismicity rate comparisons between events in the period 2006-2007 and 2009. (a) Seismicity rates during the period 2006-2007 and 2009 show a small degree of variation from each other but are markedly different from that seen in 2008; in both these periods, a large number of smaller magnitude earthquakes are present. b) The seismicity rate/year is plotted against magnitude.

In the next section, the seismicity pattern is compared with the reduced displacement for the period 2006-2009 to investigate how closely the absence of recorded activity at these depths coincides with changes in the reduced displacement values. These changing values serve as a proxy for the changes in background noise levels which may be overshadowing the signals of interest.

1.5 *ASSESSING THE VALIDITY OF TEMPORAL SEISMICITY PATTERN*

Reduced displacement (D_r) is a measure of tremor amplitude which corrects for geometric spreading; that is, that given an event location, the expected amplitude of the signal at a particular station is calculated by factoring in the distance between the source and the station. The method was developed by Aki and Koyanagi (1981) for analog film records and is based on the equation:

$$D_r = \frac{A}{2\sqrt{2}} \cdot \frac{r}{M} \tag{1.4}$$

Where A is the peak-to-peak amplitude in nanometers, r is the distance from the source to the receiver in kilometers and M is the instrument magnification at the tremor frequency. A modified version of this founding principle developed by Fehler (1983) has been used in this study. This is based on surface waves as tremors are thought to be mainly generated in the upper part of the conduit as a result of fluid oscillation and comprised primarily of surface waves. If it is assumed that the waves which make up the tremor are comprised primarily of sine waves of a single dominant frequency, then the D_r can be calculated by the following equation.

$$\mathbf{D_r} = \mathbf{x}\sqrt{\frac{r\lambda}{2}} \tag{1.5}$$

Where x is the seismic displacement in nanometers, r is the distance from the source to the receiver and λ is the wavelength. λ and r have units of kilometers. Figure 1.14 shows the results when the reduced displacement calculated as described above is overlain on a time depth plot of KBGS catalog events. In this case the source is assumed to be located beneath Klyuchevskoy Volcano and PIRE stations BEZC (green symbols)

and BELO (blue symbols) were used to ensure that data were available for the entire period in question. A similar calculation was done assuming a source location beneath Bezymianny volcano with the only effect being a small decrease in the amplitudes. From this plot, it can be seen that the number of located deep events rapidly diminishes when a reduced displacement value of roughly 0.05 cm^2 is surpassed. These results support the idea that the disappearance of events may be caused by an overshadowing of waveforms by tremor and other surface processes such as rock falls. Higher reduced displacement values also correspond to periods where the number of shallow, locatable events shows a marked increase.
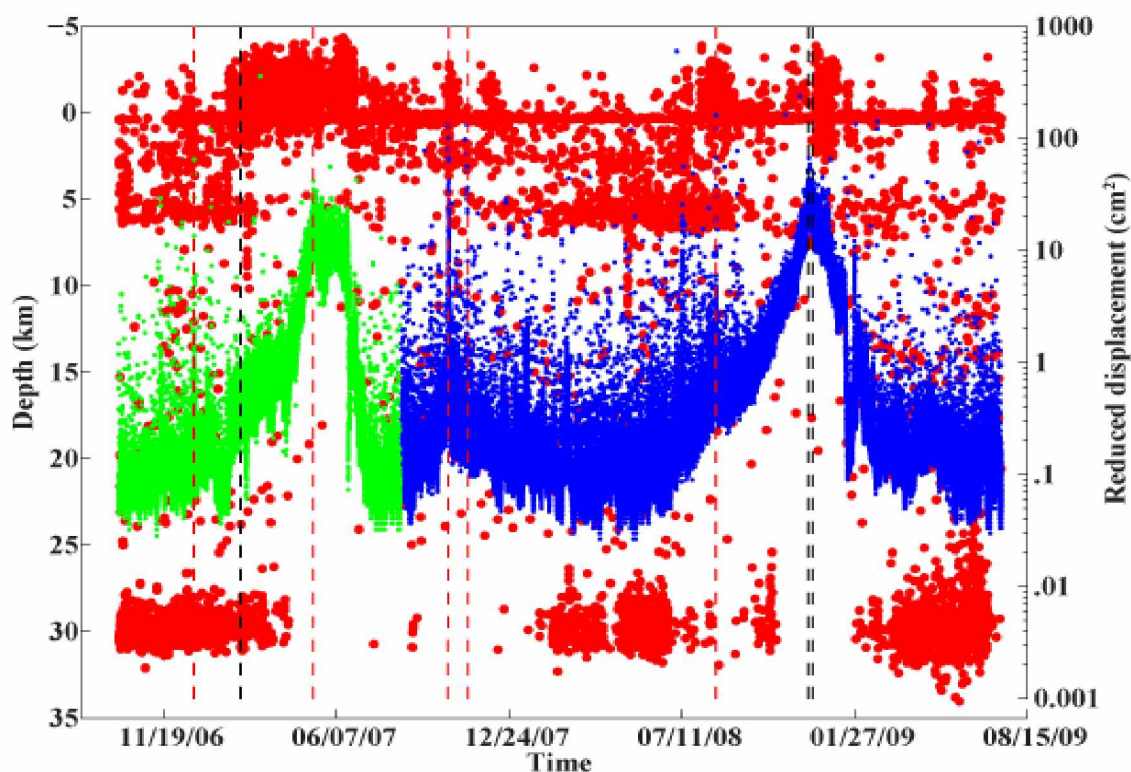
Figure 1.14 Plot of reduced displacement calculated on data from the KVG for the period 2006-2009 coupled with the time-depth plot of earthquake hypocenters for the same time interval. The green symbols shows the reduced displacement calculated for PIRE station BEZC while the blue ones show the same for station BELO; the red circles mark the overall seismicity beneath the KVG. Seismicity gaps tend to correlate with increase in reduced displacement values. Red dashed lines are explosive eruptions of Bezymianny volcano while black dashed lines mark explosive Klyuchevskoy eruptions.

The results are however in conflict with the results of other studies such as the master event cross correlation tests. For this test, a characteristic deep event was used as a master waveform in searching the continuous waveform data for other similar events during one of the "off" periods in 2008. No new events were found when this technique was applied to waveform data in this period. While the reduced displacement results shows that the signals of interest can be covered up by other signals during these lulls, the lack of new events in the master cross correlation search indicates that there may be no events present to be overshadowed. Given these conflicting results, this seismicity pattern warrants further investigation; this will be the primary focus of chapter 2.

Chapter 2 Exploring through the seismicity cloud to highlight fine scale structures beneath the Klyuchevskoy Volcano Group

2.1 *INTRODUCTION*

The chief purpose of this chapter is to illuminate any fine scale structures that may be hidden in the seismicity cloud. These structures may be a deep seated magma chamber, a dike which connects said chamber to the shallower system or a small source region which is repeatedly activated by a distinct mechanism. Many of the characteristics of deep seismicity support the idea that one or more of these features may be present in this region. As noted in the thesis introduction, a number of studies have reported the presence of a low velocity region at depths of ~ 30 km beneath the KVG. Low-velocity regions beneath volcanoes are often associated with magma chambers because the speed of seismic waves traveling through this molten mass is significantly retarded.

The corresponding absence of seismicity at depths of 30 km and the sparsity of activity at 5-7 km, where the shallow magma chamber is proposed to reside both beneath Bezymianny and Klyuchevskoy (Thelen et al., 2010), may be related to the transport of magma from the deep to shallow system. While in a normal continental setting the temperature generally increases with increasing depth, a reverse geothermal gradient has been proposed in the environs of a magmatic system (Blundy et al., 2006). As magma ascends in the conduit, polybaric crystallization leads to an increase in temperature; since crystallization increases as the pressure decreases, the temperature in the conduit should also increase as the magma reaches shallower levels. An increase in temperature would explain the absence of seismicity at the 5 km level where the magma enters the shallow

storage region. Higher temperatures are expected to increase the plasticity of the crust and so hinder brittle failure which is associated with most seismic events.

The similarity in the appearance of waveforms in this data set serves as a strong indication of the source events' occurrence in relatively close proximity to each other and to their being generated by the same source process. Typically, as the inter-event distance between two earthquakes increases, the seismic waves associated with them travel through increasingly different ray paths which will result in different waveform appearances at the same station.

To quantify which of these possibilities are most probable in this data set, three of the techniques used are discussed in this chapter. The first technique is detailed in section 2.2; this section focuses on the cross correlation analysis of a large subset of the data which allows for the classification of waveforms into distinct families. In so doing, it is possible to determine any spatial or temporal variations in DLP waveforms. The three sections which follow are devoted to issues related to the earthquake locations of the DLP events; in section 2.3, the second technique which looks at the standard locations is summarized while in sections 2.4 and 2.5, the double difference relocation technique is discussed.

2.2 *LONG LIVED SOURCE PROCESSES*

When two events occur in close proximity to each other and are generated by the same source mechanism, they produce similar waveforms on individual stations (Shearer, 1997). Waveform cross correlation provides a means of assessing the degree of similarity that these events share. This technique is commonly used to evaluate the existence of

clusters of repeating events, constrain the lifespan of individual sources and determine temporal changes in those sources which may be indicated by evolution of the waveforms which make up a given family. Cross correlation analysis of waveforms was performed using the correlation toolbox in Matlab (Buurman and West, 2010).

To investigate the behavior of deep events during one cycle of deep activity beneath the KVG, 1115 events occurring at depths greater than 15 km were extracted from the larger data set during the period 12/24/2007 to 12/31/2008. For each event, 30 second waveform segments were extracted from continuous waveform data on PIRE station BEZD using P wave arrival times on KBGS station CIR since arrival picks had not yet been added to the PIRE data. Though waveform data were unavailable for CIR, the fact that they were used in deriving the majority of the events in the KBGS catalog suggests that it is among the most reliable stations in that network. Likewise, station BEZD was chosen out of the PIRE stations due to its strong signal-to-noise ratio and the continuity of its data throughout the period under study.

In Matlab, these subsetted data were cropped to 15 seconds (5 seconds prior to the P wave arrival and 10 seconds afterwards) and a 4 pole Butterworth band pass filter applied between 1.5-10 Hz. Following this, each waveform was cross correlated against each of the other waveforms in the data set in a 6 second window (1 second prior to the P wave arrival and 5 seconds after) to quantify their relative similarities. The maximum correlation coefficient which was calculated in this step is plotted in figure 2.1. For each pair of waveforms, a value is assigned based on their cross correlation coefficient; that value is then mapped onto a given color with warmer colors denoting a higher correlation

value. The brown diagonal line on the plot represents the cross correlation coefficient

derived when a waveform is cross correlated with itself.
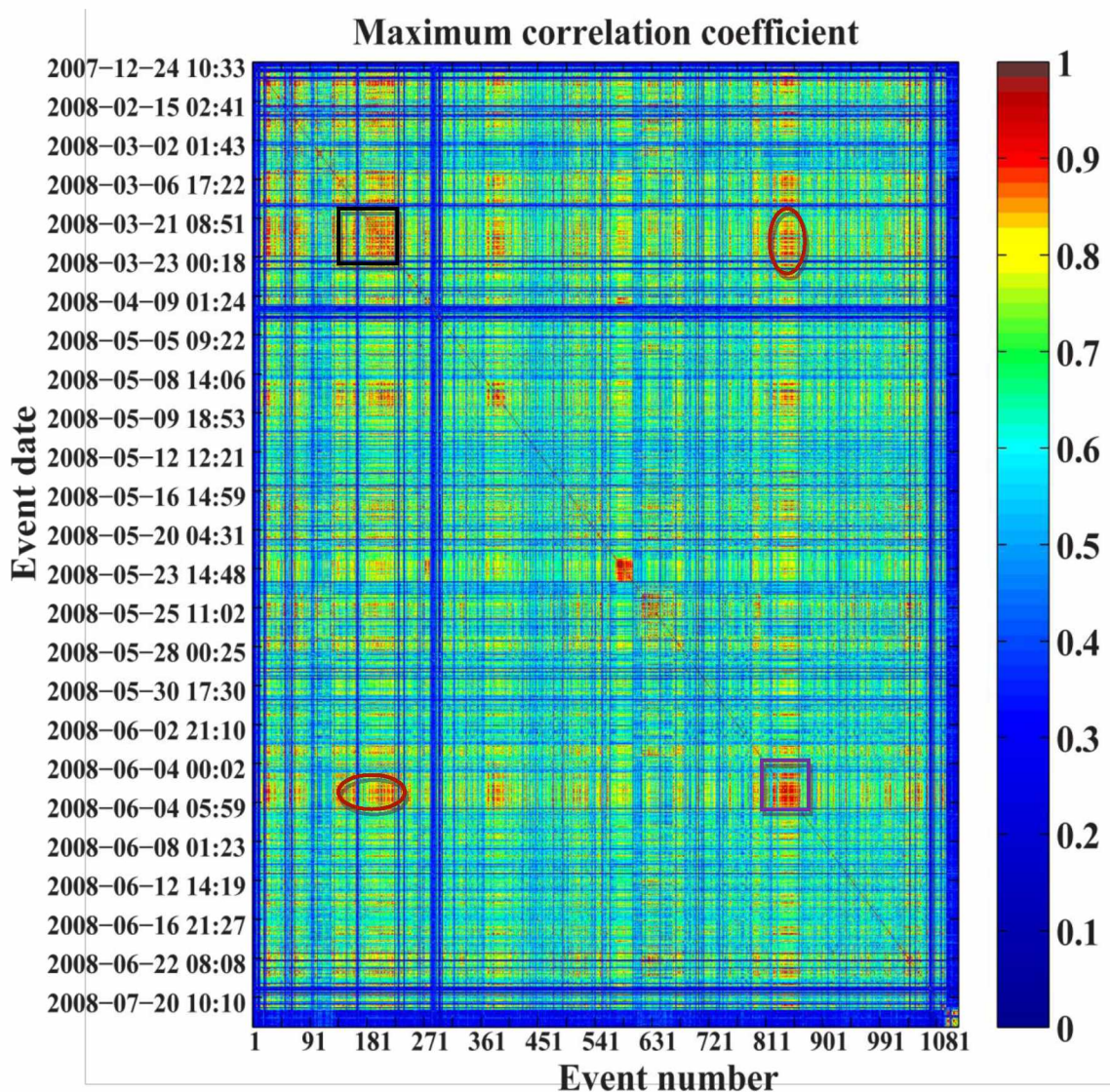
Figure 2.1 Plot of the maximum cross correlation matrix for 1115 events occurring beneath the KVG between 12/24/2007 and 12/31/2008. As indicated by the abundance of warmer colors (cross correlation 0.8 and above) in this plot, many of the events share a high degree of similarity. Events with high cross correlation values are highlighted in the black and purple boxes and the red ellipses. The lack of waveform evolution in this data set is highlighted on this figure; events which correlate well with each other early in the data (black box) also correlate well with others later in the set (purple box and red ellipses).

From the maximum cross correlation plot in figure 2.1, it is clear that a large number of the events in this period share many common features in their waveforms. Moreover, groups of events which may represent individual families can be seen in the squares of red such as the one highlighted above. The lack of waveform evolution in this data set can also be seen in figure 2.1; here events which correlate well with each other early in the data set (black box) correlate just as well with other events in later periods (purple box and red ellipses).

To better isolate these families, clusters of events with correlation coefficients of 0.80 were then extracted from the set. In figure 2.2, stacked waveforms for the 10 largest families along with a histogram of their periods of activity are shown. Each family spans several months and shares active periods. The largest family contained 339 members which is 10 times larger than the next largest family derived from the cross correlation analysis; all others families found by this method contained less than 50 events.
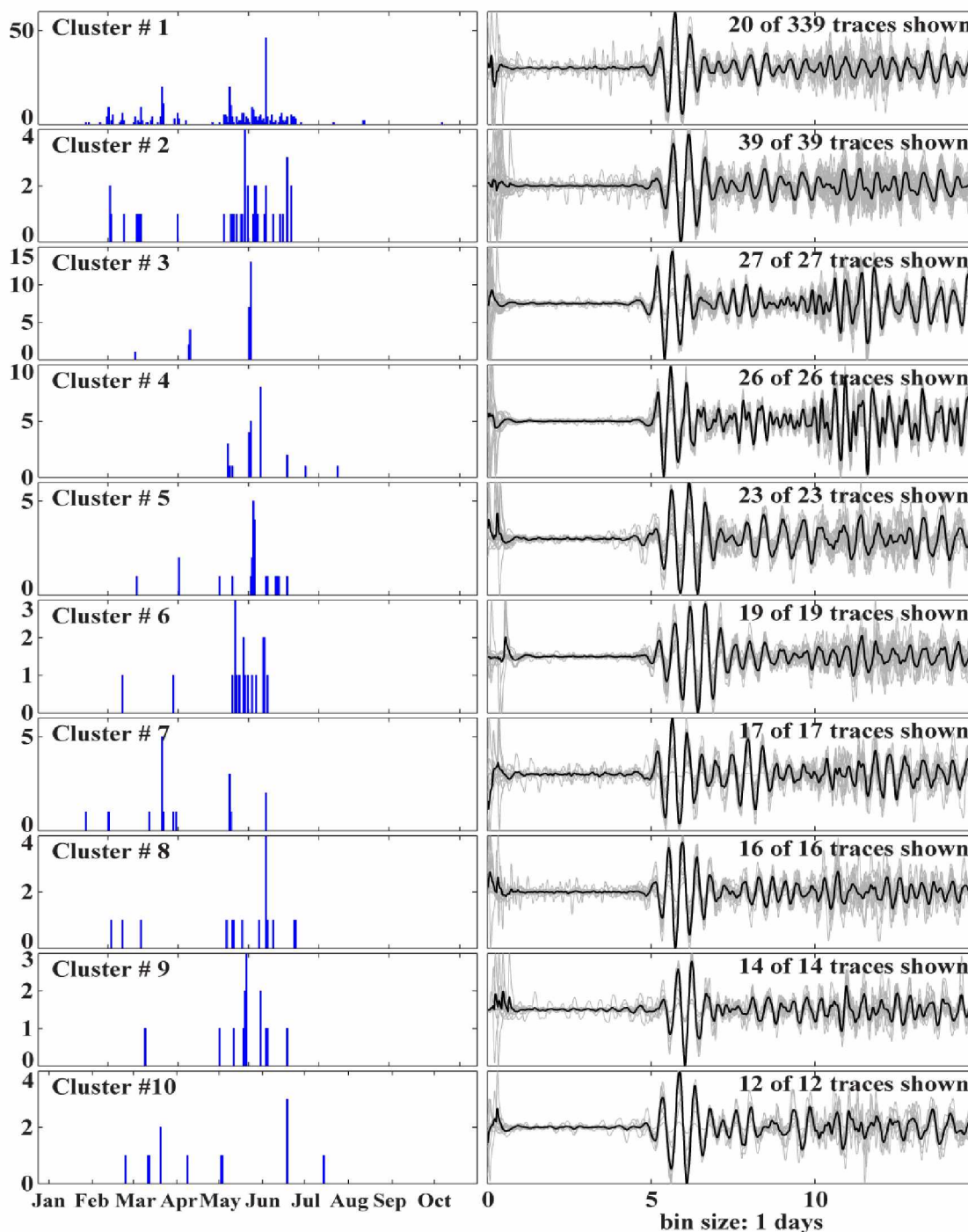
Figure 2.2 Occurrence plot of waveforms in the 10 largest clusters of events from 12/24/2007 to 12/31/2008. All families are long lived, lasting for several months. Also of note is the apparent waveform similarity between clusters and the fact that the largest cluster is at least 10 times the size of the other clusters. Vertical scales on the histograms on the left varies for most of the clusters.

To assess the behavior of waveforms within an individual family, the cross correlation process was repeated on each isolated cluster. For each cluster, the waveforms were cropped to 7 seconds–this includes the entire P wave and part of the S waves as well. The cross correlation is done primarily on the P waves because these signals are most coherent; coherence of waveforms is limited for the S wave portion, hence only the most coherent portion is used in the analysis. The waveforms were then normalized to equalize their amplitudes. To each cluster, a stacked waveform of the waveforms therein was generated and appended to the set; stacking accentuates the primary features of the waveforms while minimizing small perturbations. This stacked waveform was used as the master waveform against which all the other waveforms in the cluster were cross correlated against.

The interferogram from the largest cluster of events which was generated as part of the process detailed above is shown in figure 2.3. When each event is cross correlated against the master event in a 0.8 second time window moving along each waveform in increments of 0.2 seconds, the interference pattern of these waveforms are measured and used to create the diagram in figure 2.3. This diagram superimposes the value of the correlation coefficient between the master event and each waveform as a color over the part of the waveform to which it corresponds. To improve the visibility of cross correlation patterns, only every other waveform is plotted as the large number of waveforms overshadows the cross correlation patterns; also only the first and last event occurrence dates are shown. This family of events spans 10 months with peaks in activity occurring in May and June of 2008.

The change in the intensity of color for a given peak over time is an indication of source migration and/or changes in the source mechanism such as increasing size of the resonator in the case of an LP event. No such change is apparent with these waveforms indicating that the source location and mechanism remains relatively stable throughout the life span of each cluster.
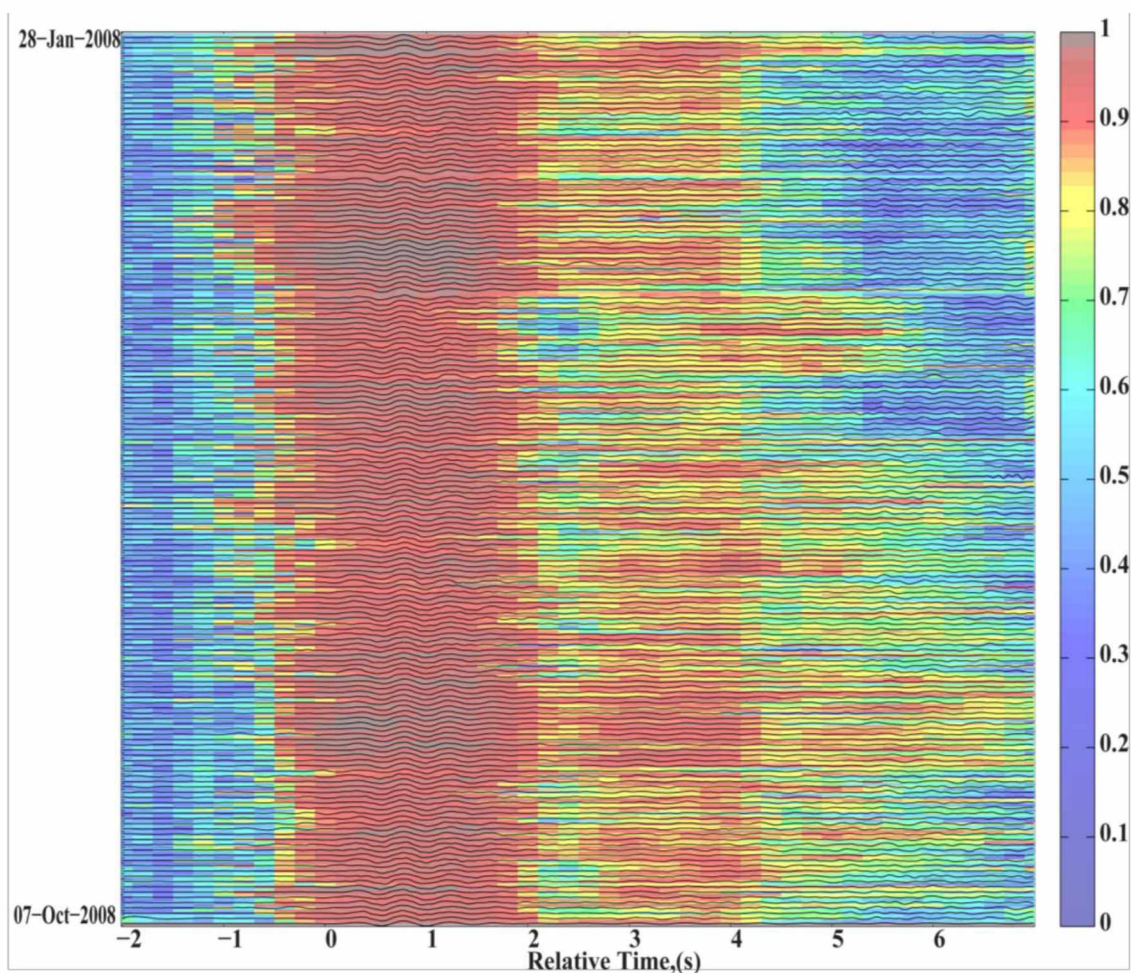
Figure 2.3 Interferogram for the largest cluster of events with a cross correlation coefficient of 0.80. Waveforms in this cluster span the period 01/30/2008-10/31/2008; very little variation is seen in the waveforms overtime - an indication that the source location and mechanism is relatively stable for long periods. The degree of correlation between waveforms on the S wave portion of the waveform tends to vary randomly.

The level of similarity shown between waveforms in each cluster does not correspond well with the spatial separation assigned to them in the analyst reviewed catalogs which were supplemented with this data set. The cloud of seismicity associated with this data set extends over several kilometers which is not in keeping with the idea that for waveforms to share such similarity, individual events must occur in relatively close confines to each other. In figure 2.4 an example of the location spread is shown using the original KBGS catalog locations for events in the five largest clusters from figure 2.2.
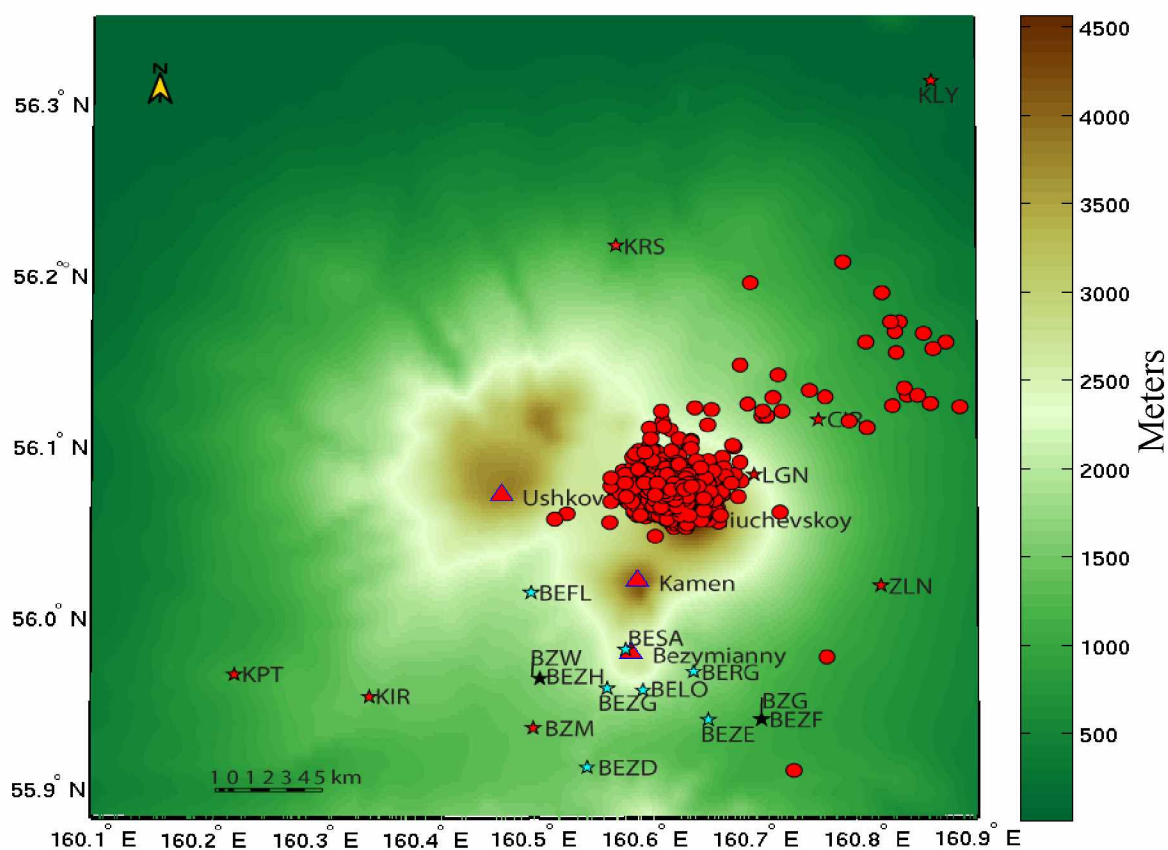
Figure 2.4. Map of original KBGS catalog deep events occurring from 12/24/2007 to 05/31/2008. The bulk of the seismicity is located in a 5 km wide cloud beneath Klyuchevskoy. Stations in red are KBGS stations within close proximity of the KVG, those in blue are PIRE stations (these are not used in the location of the mapped events) while those in black are collocated PIRE and KBGS stations.

While the bulk of the seismicity is within a 5 km wide cloud, the length of the minimum error axes reported by KBGS range from 5 to 19.5 km; the major error axes run between 6 and 34 kilometers and the depth error runs from 6 – 15 km. An attempt to improve upon these locations with new data available from the broadband sensors deployed on Bezymianny is discussed in the next section.

2.3 *IMPROVED EVENT LOCATIONS*

One of the chief goals of this deployment was to improve the locations of deep events beneath these volcanoes. The results of the cross correlation analysis conducted in section 2.2, made it clear that there were undoubtedly large errors associated with the existing catalog locations given the location spread between these highly similar events. Significant effort was therefore made to diminish this error and improve the locations by using the new data in this study. For this step, the Antelope location tools dbpick and dbloc2 (genloc) (Pavlis et al., 2004) were used.

Calculation of standard locations here is made utilizing the difference between S-P travel times as well as the P and S arrivals times for a given event at the different stations in the network. To improve the existing locations in the catalog, it was necessary to add pick arrivals to the new waveform data. Arrival times from the KBGS catalog were used to zero in on the desired events on the PIRE stations following which, arrival flags were added on waveforms bandpass filtered between 1-10 Hz to filter out some of the background noise which makes it difficult to assign picks. To these waveforms, P arrivals were added to the first prominent peak which could be distinguished above the

background noise on the vertical channels while S arrivals were added to the start of the next prominent packet of waves on the horizontal channels.

The low frequency content and emergent onset of the majority of these waveforms adds significant difficulty in pinpointing the exact arrival times for an event. Due to this fact, each arrival flag was assigned an error window based upon the region of time in which the arrival is thought to have occurred. Arrival times and pick errors assigned by this method are written to a database and available for event location through dbloc2. These errors are used as a weighting factor by the location algorithm and typically range from 0.5 – 1.5 seconds depending on the quality of the waveform.

Following assignment of arrival times in dbpick, dbloc2 was used to provide new locations for these events. This graphical user interface allows users to locate events and accepts as inputs the arrival times and station information from the database that is being worked on. This software package also interfaces with the dbpick GUI allowing users to change arrival times and pick errors during the event location process. In this way picks can be added or deleted, arrival times and error windows altered to achieve the best possible event location.

A common measure used to assess the error is the standard observation (sdobs) error value; this is a measure of the discrepancies in the arrival times of phases used to locate an event. The sdobs is calculated in the following way:

$$\frac{\sqrt{\Sigma t_r}}{f} \tag{2.1}$$

Where t_r are the time residuals for each phase and f is the number of degrees of freedom. The degree of freedom is defined by the number of defining observations – the

number of dimensions being solved for (in this case, 4 dimensions are being solved for, namely latitude, longitude, depth and origin time). The time residual is the difference between the observed and the predicted arrival times.

For the purpose of this study, picks were only added to waveforms which made up the 5 largest families (451 events total) indicated in figure 2.2. Only these families were considered because one of the key observations highlighted earlier was the existence of a large number of similar events in the data set and the need to investigate their behavior and probable sources. In an effort to determine how the station distribution affected the event locations, locations were calculated in 3 ways using three different subsets of picks. While the PIRE network is confined to a few kilometers around Bezymianny volcano, the KBGS network contains stations with a wider distribution but few within 1 kilometer of the volcanoes (see stations location map in figure 1.2). To look at the effect of this network geometry, the locations were estimated as:

- On a small subset of events occurring in early June 2008
  - Using only arrival times from the KBGS catalog
  - Using a combination of PIRE and KBGS catalog picks
- On the entire set of 451 events under study just using PIRE picks

The 1D velocity model shown in table 2.1 developed by Senyukov and Droznina (2009) for the KVG was used in the calculation of event locations.

Table 2.1 1D velocity model for the KVG used in event location.
This is model B from Senyukov and Droznina (2009) which has been used to calculate event locations beneath the KVG from 1999 to present. V_P and V_S are the P and S wave velocities respectively. Velocity layer 5 has variable velocity throughout hence the labels V_{P1}, V_{P2}, V_{S1}, and V_{S2}; all other layers have one constant velocity through the entire thickness of the layer.

Layer number	Vp (km/sec)	Vs (km/sec)	Bottom of layer (km)
1	2.95	1.71	0.0
2	2.9	1.61	1.0
3	3.5	1.94	2.0
4	4.3	2.49	4.5
5	$V_{P1} = 5.9$ $V_{P2} = 6.2$	$V_{S1} = 3.41$ $V_{S2} = 3.58$	9.5
6	6.3	3.64	21.0
7	6.8	3.93	31.0
8	7.7	4.45	40.0

The new locations which resulted for the entire set when using only PIRE station picks (yellow symbols) are shown in figure 2.5 along with original KBGS locations (red) for the same events. The event locations calculated on PIRE stations have depth errors up to 8.7 km while the sdobs values run from 0.0025 to 1.166 seconds. The major and minor axis of the error ellipses ranged from (0.5–38 km) and (0.3–16 km) respectively. Figure 2.6 shows the error ellipses for a small subset of these events occurring between 12/24/2007 and 06/01/2008. For all the methods mentioned above, the new locations were always to the south and west of the original KBGS locations by an average of about 5 kilometers. The newly derived locations did not show any dramatic improvement in the scatter contained in the original catalog, there was in fact an increase in the inter-event spread. To resolve this issue, the events were relocated using the hypoDD algorithm of Waldhauser and Ellsworth (2000).
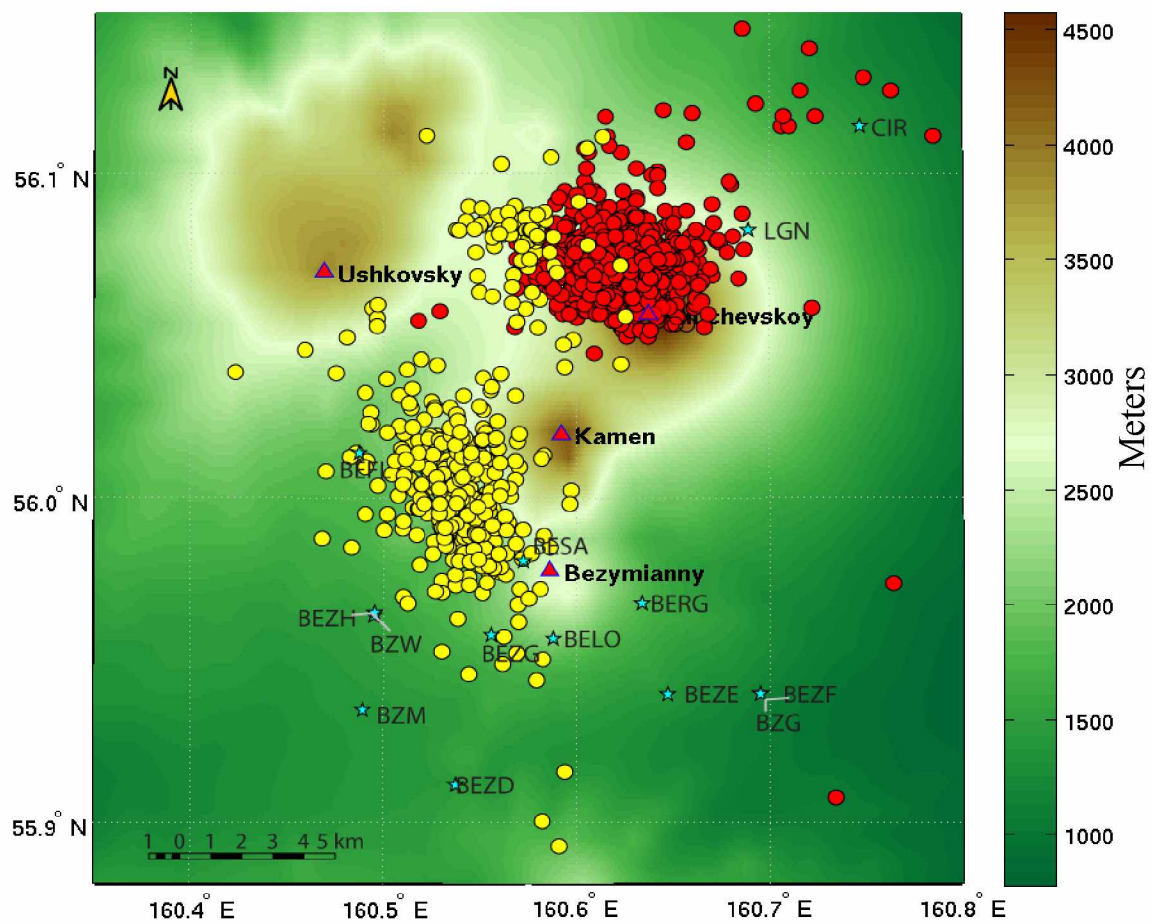
Figure 2.5 Comparative map of standard event locations calculated by KBGS (red symbols) and using the PIRE network (yellow symbols). Stations with three letter code names are KBGS stations in close proximity to the volcanoes while those with 4 letter code names are PIRE stations.
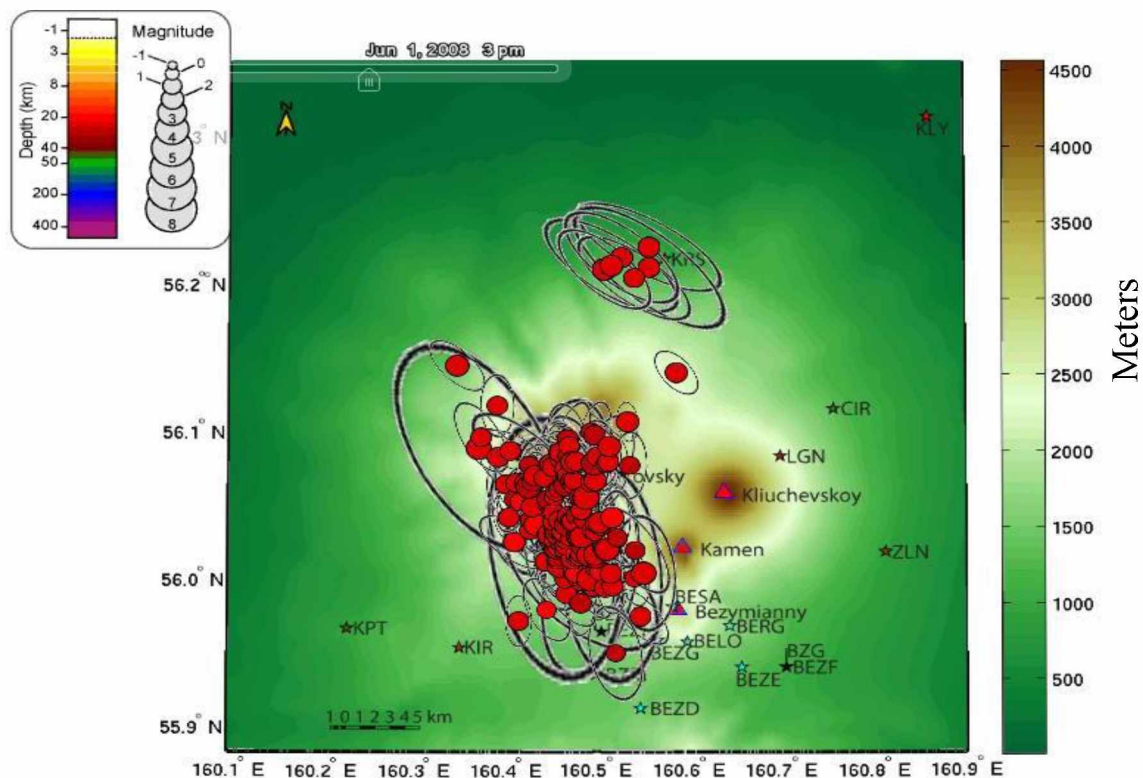
Figure 2.6 Map of event locations and their associated error ellipses for a subset of events located using only PIRE stations. Stations are as described in previous figures. The length of the minor and major axis of the error ellipse range from 0.3–16 km and 0.5–38 km respectively. Event size and color are a function of depth and magnitude respectively as indicated by the legend on the left. Time bar on the top of the map marks the date and time of the last event shown on the map.

2.4 *INITIAL EVENT RELOCATION USING THE HYPODD ALGORITHM*

The hypoDD algorithm is a joint hypocenter determination technique which provides a means for attaining relative event locations for a large number of earthquakes simultaneously. This technique is based on the theory that waveforms occurring in close proximity to each other will travel through almost identical ray paths given that the separation between them is small compared to the event to station distance or the length scale of the velocity heterogeneity (Waldhauser & Ellsworth, 2000). Based on this, the difference in travel times for two events at a given station can be attributed to their spatial offset since the difference in their ray paths is minimal. In this technique, cross

correlation data is used in combination with catalog travel time information, to derive highly accurate inter-event distance between members of a single family which can be determined to the accuracy of a few milliseconds. The locations of these families relative to other families or other single events are determined to an accuracy of the catalog travel time data.

The first attempt to use hypoDD on this data was done using all 451 waveforms selected in section 2.3. Absolute differential travel times were calculated for pairs of events for each station and phase using the arrival times added to the PIRE data. To calculate the differential time based on cross correlation analysis, the waveforms for each station and phase were loaded into Matlab and cross correlated in a 7 second window as described above. The differential times in this case are the adjustments necessary to ensure that each waveform is exactly aligned with its neighbor. When using the cross correlation data in hypoDD, only differential times from events which correlated with each other at 0.80 or better and with lag times less than 0.5 seconds were utilized. *A priori* weights are given to the cross correlation data based on the square of their coherency (a measure of how well correlated the waveforms are) while weights are given to catalog differential times based on the pick errors assigned in dbpick. These differential times along with the station information and catalog origin times served as the primary input for hypoDD. Origin times from the catalog are used as starting point in the first iteration, after which new origin times are calculated in subsequent iterations. To define clusters of similar events for the location process, the criteria in table 2.2 were

used. The largest cluster defined this way contained 168 members with all other events in

the catalog considered as singletons (events which do not belong to a cluster).

Table 2.2 hypoDD clustering settings.
MAXWGHT: the minimum catalog weight which is allowed – this is a hypoDD characterization based on the error window which is assigned in dbpick.
MAXDIST: the maximum separation allowed between event pairs and station
MAXSEP: defines the maximum distance allowed between event pairs
MAXNGH: maximum number of neighbors per event (neighbors are defined by MAXSEP).
MINLNK: minimum number of links between neighbors
MAXOBS: maximum number of links per pair saved.

MINWGHT	MAXDIST (km)	MAXSEP (km)	MAXNGH	MINLNK	MINOBS	MAXOBS
0	50	10	60	5	5	50

The example shown in table 2.3 below is of a hypoDD run using both cross

correlation and catalog data; for the 1st 5 iterations, greater weighting was given to

catalog data to pinpoint the absolute location of the clusters. Preferential weighting was

then shifted to cross correlation data in later iterations to refine the final locations. For the

location of these events, hypoDD was run in least squares (LSQR) mode; there were no

significant changes in event locations when a small subset of these events was located

using singular value decomposition (SVD), though there was a change in the mean error

obtained as the LSQR method tends to underestimate that value.

Table 2.3 An example of a typical hypoDD run using both cross correlation and catalog data.
NITER refers to the number of iterations; WTCCP, WTCCS, WTCTP, WTCTS refer to the weight given to the cross correlation and catalog P and S phases respectively. Terms WRCC, WRCT are the residual thresholds for the cross correlation and catalog data; WDCC and WDCC are the maximum inter-event separating in kilometers which will be permitted. DAMP indicates the damping value used when events are located in LSQR mode; a value of -9 means that that data was not used.

NITER	WTCCP	WTCCS	WRCC	WDCC	WTCTP	WTCTS	WRCT	WDCT	DAMP
5	0.01	0.05	-9	-9	1	0.5	-9	-9	5
5	0.01	0.5	-9	-9	0.001	0.005	8	8	5
10	1.00	0.5	8	5	0.001	0.005	7	5	10
5	1.00	0.5	6	3	0.001	0.005	4	5	10
5	1.00	0.5	6	2	0.001	0.005	4	5	15

For the events mapped in figure 2.7 clustering was not allowed as this threw out events which help constrain the relative locations of others and so increased the scatter as well as the location errors.
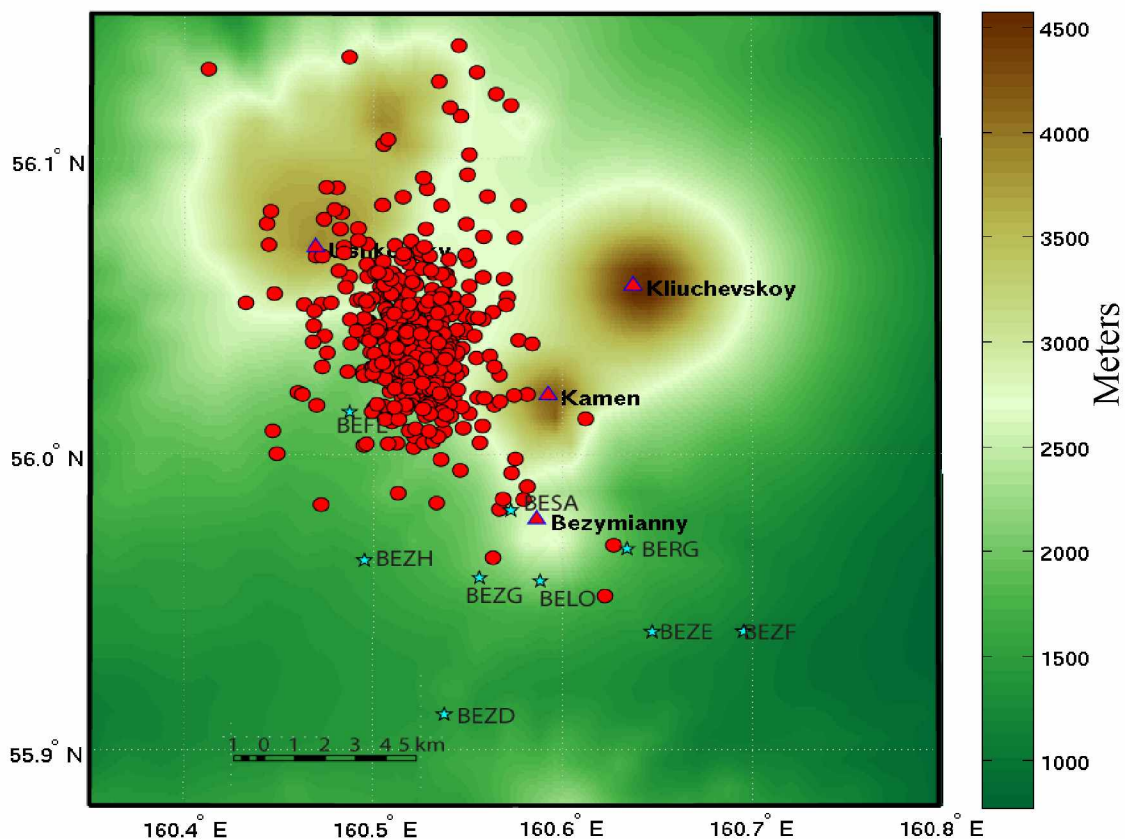
Figure 2.7 Map of hypoDD locations for the entire set of 451 events in section 2.3. While there was some reduction in the size of the cloud, there was not a significant improvement from the original PIRE event locations (see yellow markers in figure 2.5).

Although this was the most successful run, based on the reduction in errors and spatial spread from previous runs on this data set, the improvement in event locations over those originally calculated for the PIRE network was insignificant. While there was some collapsing and shifting of the seismicity cloud from the original locations, there was still a lot of scatter which was not in keeping with the similarity of the waveforms or the

generally small differential travel times obtained from the cross correlation analysis (0.001 to 0.500 seconds). A few factors may contribute to this fact such as presence of significant pick errors, clustering classification being more or less stringent than needed and a lack of homogeneity in the catalog. The homogeneity of the catalog refers to there being phase picks for every event on every channel that is used to generate a location as well as in the cross correlation data; an effort to streamline the procedure and by extension improve the locations is discussed in the next section.

2.5 SELECTING A NEW DATA SET FOR HYPODD ANALYSIS

In an effort to improve the spatial spread of the events, a new cross correlation analysis was conducted on the 451 events which were members of the five largest families in the cross correlation analysis done in section 2.3. As a starting point, waveforms from both the horizontal and vertical channels on PIRE station BEZD were cross correlated in a 23 second window which included the P and S waves as well as a large portion of the ensuing long-period coda. Following this, the data were perused and only waveforms with picks on both the horizontal and vertical channels were kept. Waveforms which correlated with a value of 0.75 or greater over this entire window were clustered into families and those families with 10 or more members were selected for further analysis. This resulted in 5 clusters with 14 to 35 members spanning the time period from 02/12/2008 to 06/24/2008 which will be referred to as multiplets 1 – 5, with multiplet 1 containing the largest number of events.

Table 2.3 gives the values required for a successful run for multiplet 1 in hypoDD; given the similarity of the events in this family, it was expected that both the

inter-event spatial and temporal separation which are defined by the WRCC, WDCC, WRCT and WDCT values should have been smaller, however, further reduction of these numbers produced large errors and resulted in the majority of the data being thrown out. The same was true for the other multiplets as well; therefore, while there was a reduction in the amount of scatter from the original locations, the cloud maintained a spatial spread of about 3.5 km on average which is much larger than expected for events which are so similar. Figure 2.8 offers a comparison of standard catalog locations using antelope (a) and those generated using hypoDD (b) for multiplet 1 events. Further steps which were taken to reduce this scatter are discussed below.
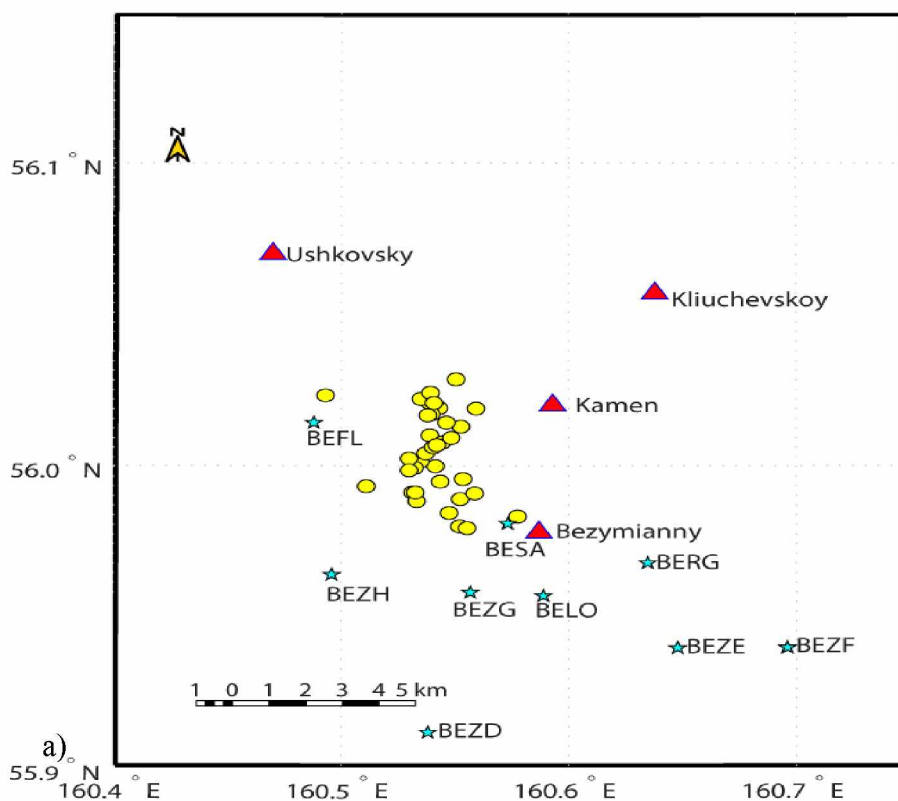
Figure 2.8. Comparison maps of standard and relative event locations. (a) Shows a map of event locations calculated using the Antelope programs. (b) Shows the same events relocated using the hypoDD algorithm. The events located with hypoDD have a maximum extent of 3.5 km as opposed to 5.2 km originally.

b)
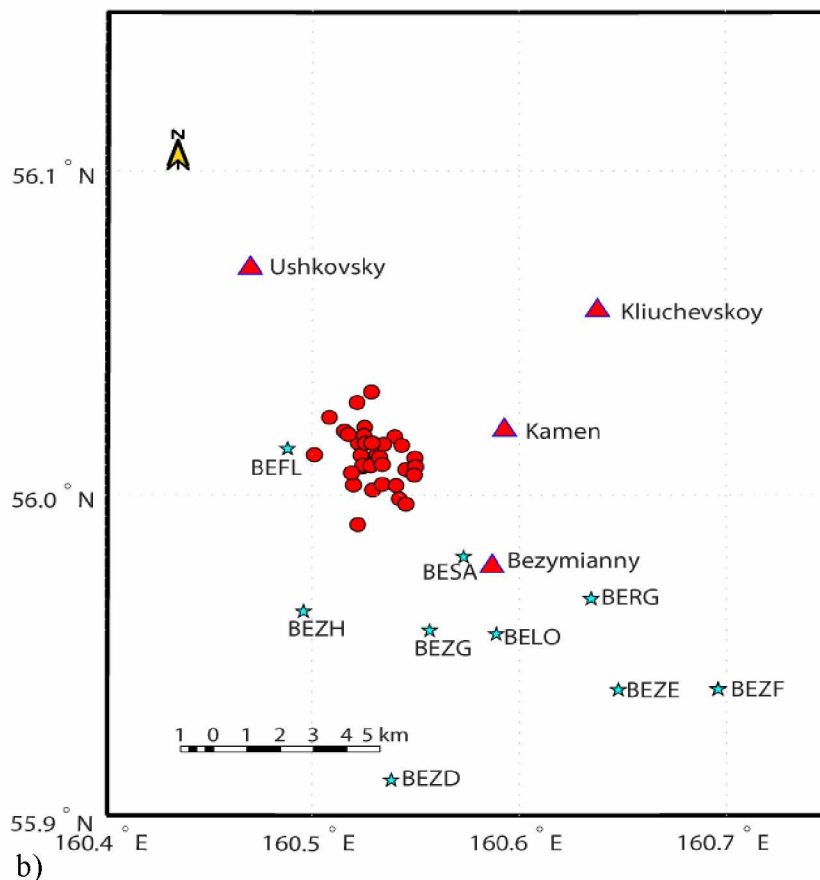
Figure 2.8 continued

   To reduce the spatial spread of the relocated multiplets, each phase pick was revised so that each pick was placed on the first prominent pick which could be clearly identified on all events for a particular station. Since most of the events have similar appearance both with each other on a given station and across other stations on the PIRE network, finding that common peak was relatively easy and introduced a degree of homogeneity to the data set which was not present before. Also, using this method rather than assigning the picks to the "first motion", minimizes the errors which are associated with trying to determine when an earthquake first arrives at a station for waveforms with emergent onsets.

The effect of this increased homogeneity in the catalog was seen when the events were once again cross correlated as described above. When clustering of events with cross correlation coefficients of 0.75 or greater was done, only 4 families of events with greater than 10 members were found. Families contained between 14–59 members; events which were originally clustered in multiplets 1 and 3 above were now merged into the largest family of 59 members. Figure 2.9 shows an occurrence plot for the 4 largest families derived in this phase.
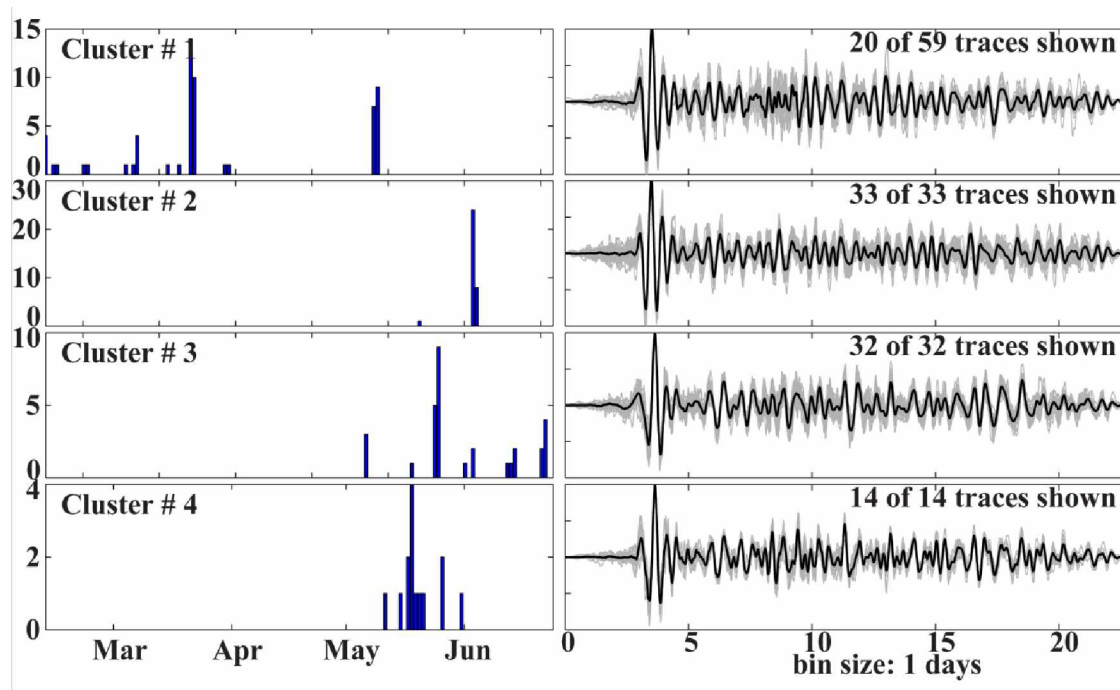
Figure 2.9 Occurrence plot for the 4 largest clusters when events are cross-correlated on the entire waveform for station BEZD

The improved homogeneity of the catalog did not, however, improve the locations considerably. Figure 2.10 shows a map of relative locations of all 4 multiplets. All multiplets have an extent which was greater than 3 km.
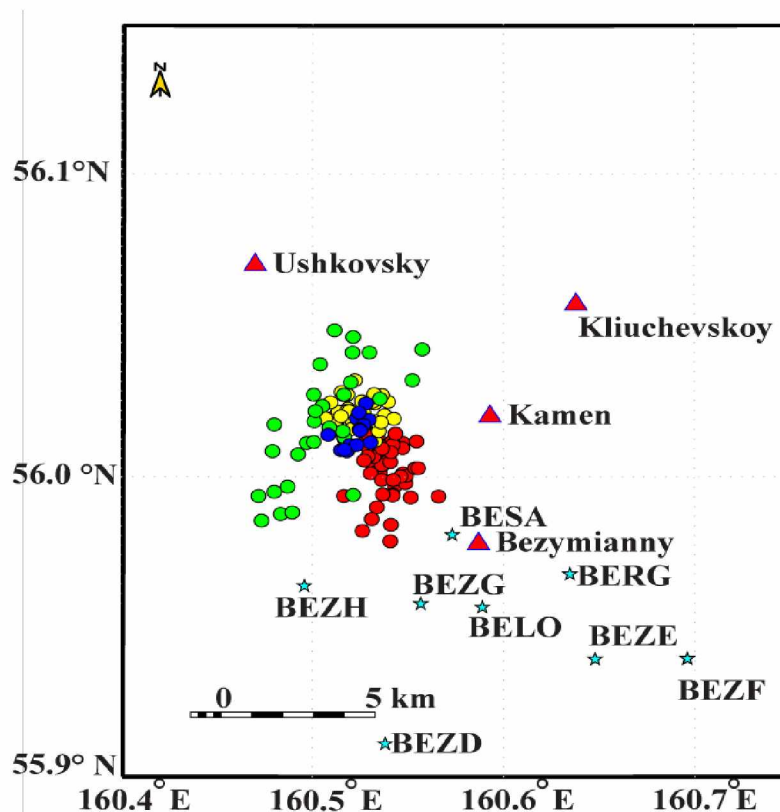
Figure 2.10 Map of hypoDD locations from multiplets 1-4 which are colored red, yellow, green and purple respectively. While multiplets 2 and 4 occur in relatively small clusters, multiplets 1 and 3 are spread across several kilometers.

2.5.1 The ultimate hypoDD run

Event locations are strongly influenced by the station distribution, and the homogeneity of the catalog and velocity model used in their calculations. Following the unsatisfactory results of the hypoDD runs mentioned above, an attempt was made to improve the homogeneity of the starting catalog. For each multiplet, the waveforms which made up the set were carefully inspected and one event chosen which had good waveforms and picks on both the vertical and horizontal channels for every station. Using this event on station BESA as the reference event, differential times were calculated for

all the other events and picks adjusted based on those times. A new catalog was created

based on those adjusted picks for all the stations, keeping the origin location and depth of

the reference event the same for all the events in the catalog. The steps mentioned above

to calculate the travel times and differential times for event pairs were repeated on this

new catalog. A schematic diagram for the pick adjusting process is shown in figure 2.11.
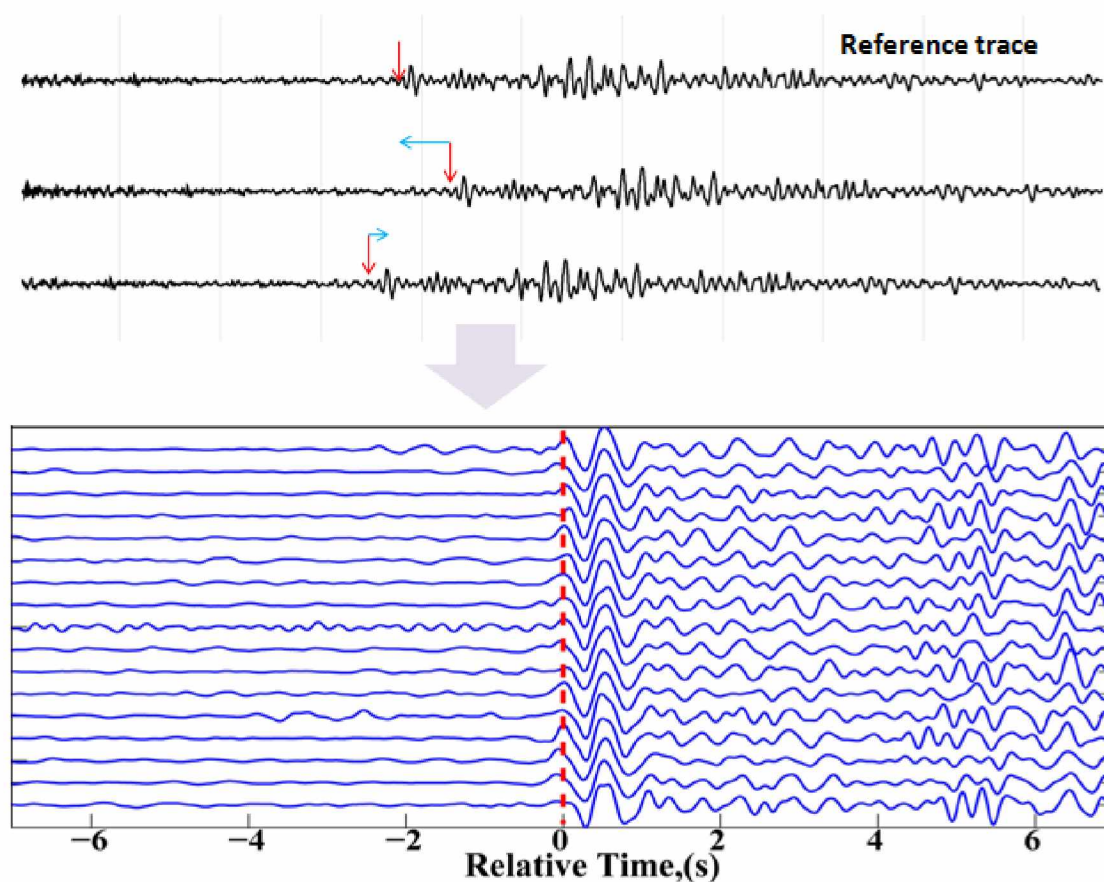
Figure 2.11 A schematic diagram of the pick adjustment procedure discussed in the text. The red arrows in the figure indicate the location of the arrival picks while the blue ones shows the direction in which the picks were shifted to account for the differential times. The bottom traces in blue are the results of the shifted picks with the red line indicating the pick location.

When hypoDD was run on these new catalogs, much more favorable results were

obtained. Each multiplet was now in a distinct cluster which spanned no more than 200 m

across when cross correlation and catalog data were used. Figure 2.12 shows maps of the

relocated events using just catalog data in (a) while b) shows those same events relocated using a combination of cross correlation and catalog data.
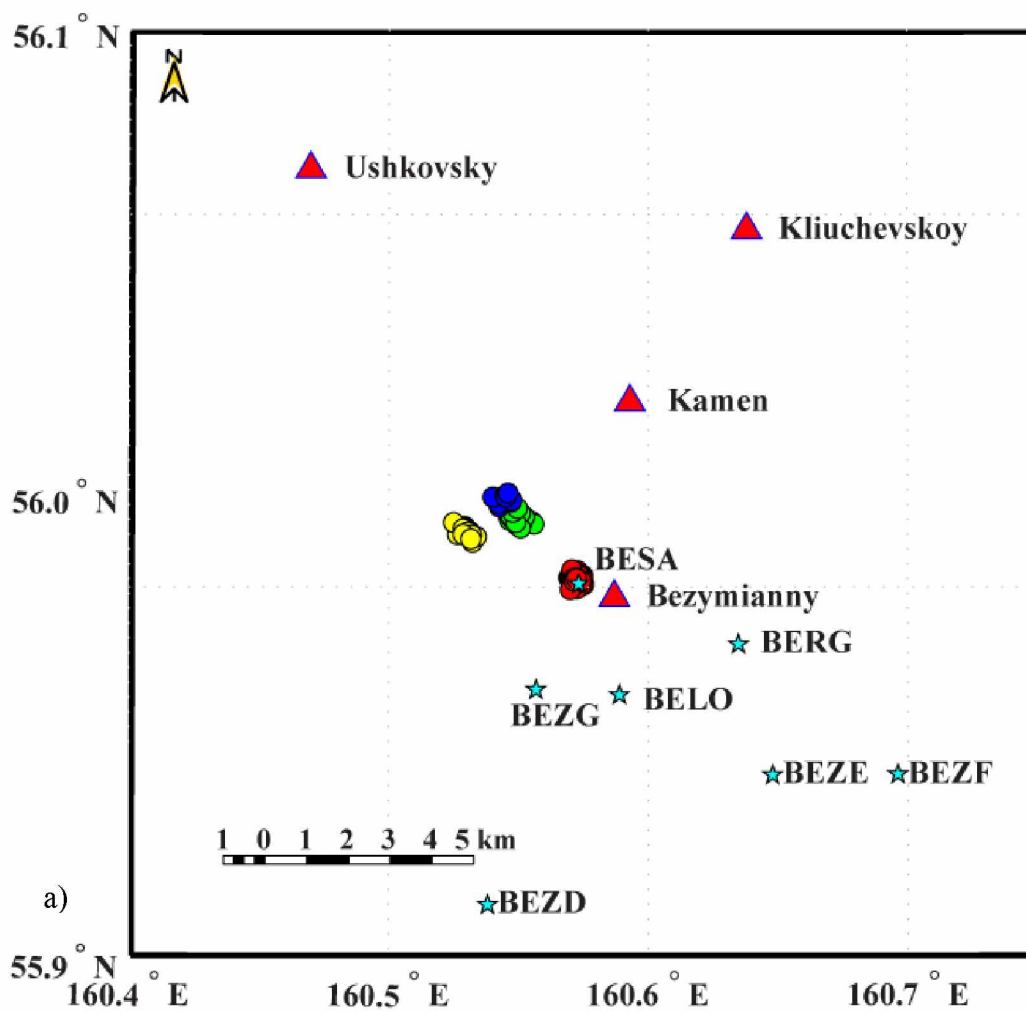
Figure 2.12 Map of relocated events from cross correlation based catalog. (a) Shows the locations calculated with just catalog data. In (b) those same event locations are calculated using cross correlation and catalog data. The different multiplets are colored as described in figure 2.10.
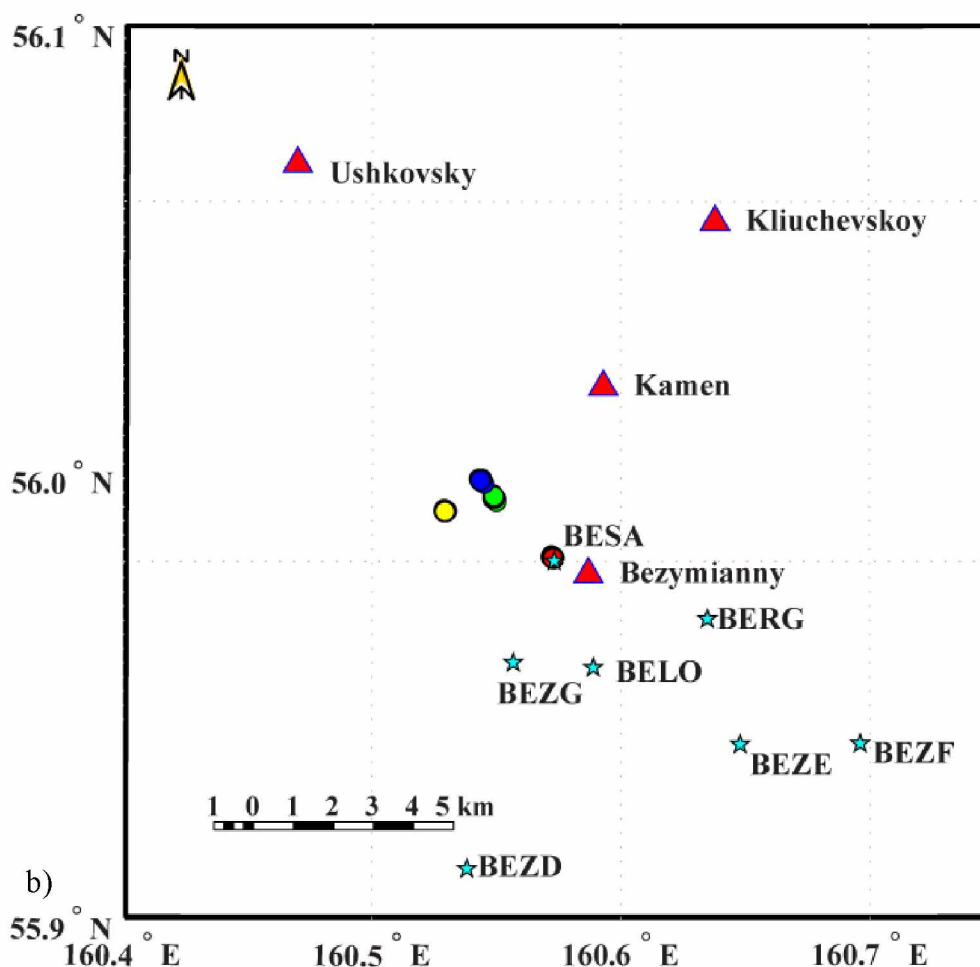
Figure 2.12 continued

As shown in the figure above, even when only the catalog based travel times are used, there is a significant collapse in the extent of the seismicity cloud from what was seen in previous examples. East-west, north-south and depth error ranges calculated using hypoDD and the length ranges of the minor and major error ellipse axis as well as depth error ranges calculated using the standard location routine in dbloc2 are detailed in table 2.4 below. Typical errors for the hypoDD relative locations are at most a few 10s of meters in all directions while the antelope errors are smallest in depth (a few 100s of meters) but extend across several kilometers along the minor and major error axes.

Table 2.4 Table of location errors calculated by hypoDD and Antelope for each of the multiplets

Family	hypoDD Errors (m)			Antelope Errors (km)		
	Depth	E-W	N-S	Depth	Minor axis	Major axis
1	2.9 – 9.9	5.7-19.4	5.5 – 16.4	0.25-0.48	6.59-7.02	8.89-9.61
2	4.1-10.9	4.4 – 15.3	2.5 – 9.7	0.53-0.74	7.44-8.65	10.19-10.6
3	6.8 – 18.6	6.8 – 19.9	5.5 – 13.1	0.43-0.47	7.40-7.60	10.38-10.7
4	4.7 – 17	11.0 – 23.4	9.3 – 21.2	0.42-0.47	7.27-7.44	9.79-10.04

The time depth plot for the cross correlation and catalog based relocations shown in figure 2.13 shows no change in the location of the multiplets in time; even when the activity of a particular multiplet ceases for a while, it once again resumes in the same relative location.

The 3D plot of all the multiplets shown in figure 2.14 offers a view of the orientation of the multiplets in space both relative to the volcanoes and to the stations used in the location calculations. All multiplets have relatively similar shapes and have their greatest extent in the vertical dimension; an expanded view of event locations shown in figure 2.14 (a) for each multiplet is shown in figures 2.15 to 2.18. An apparent alignment of the clusters with the stations used to calculate their locations is seen in figures 2.12 (a) and to some extent, in the expanded views provided by figures 2.15 to 2.18. It is therefore debatable as to whether the shape of the clusters is real or an artifact of the station distribution.
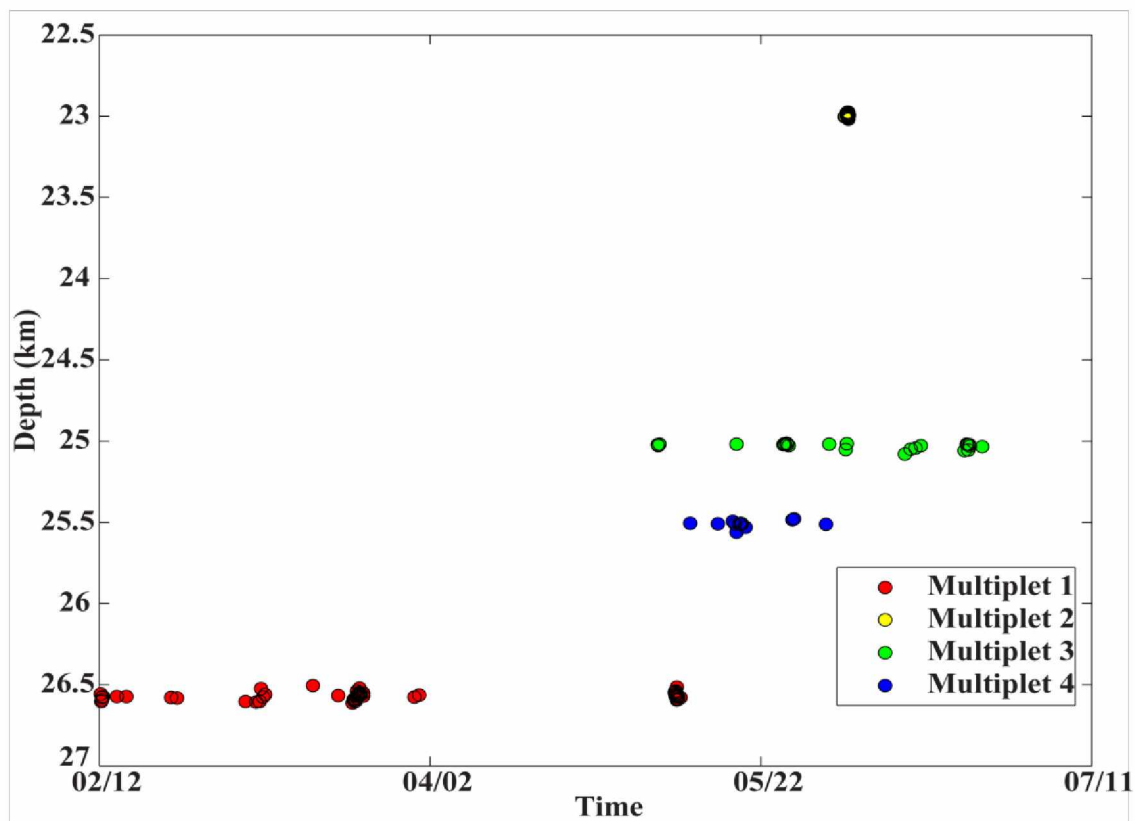
Figure 2.13 Time depth plot for all the multiplets in this study. A few multiplets exhibit the pulsating pattern which was seen in the more long term plot of figure 1.4 - this is best seen in the case of multiplets 1 and 3.
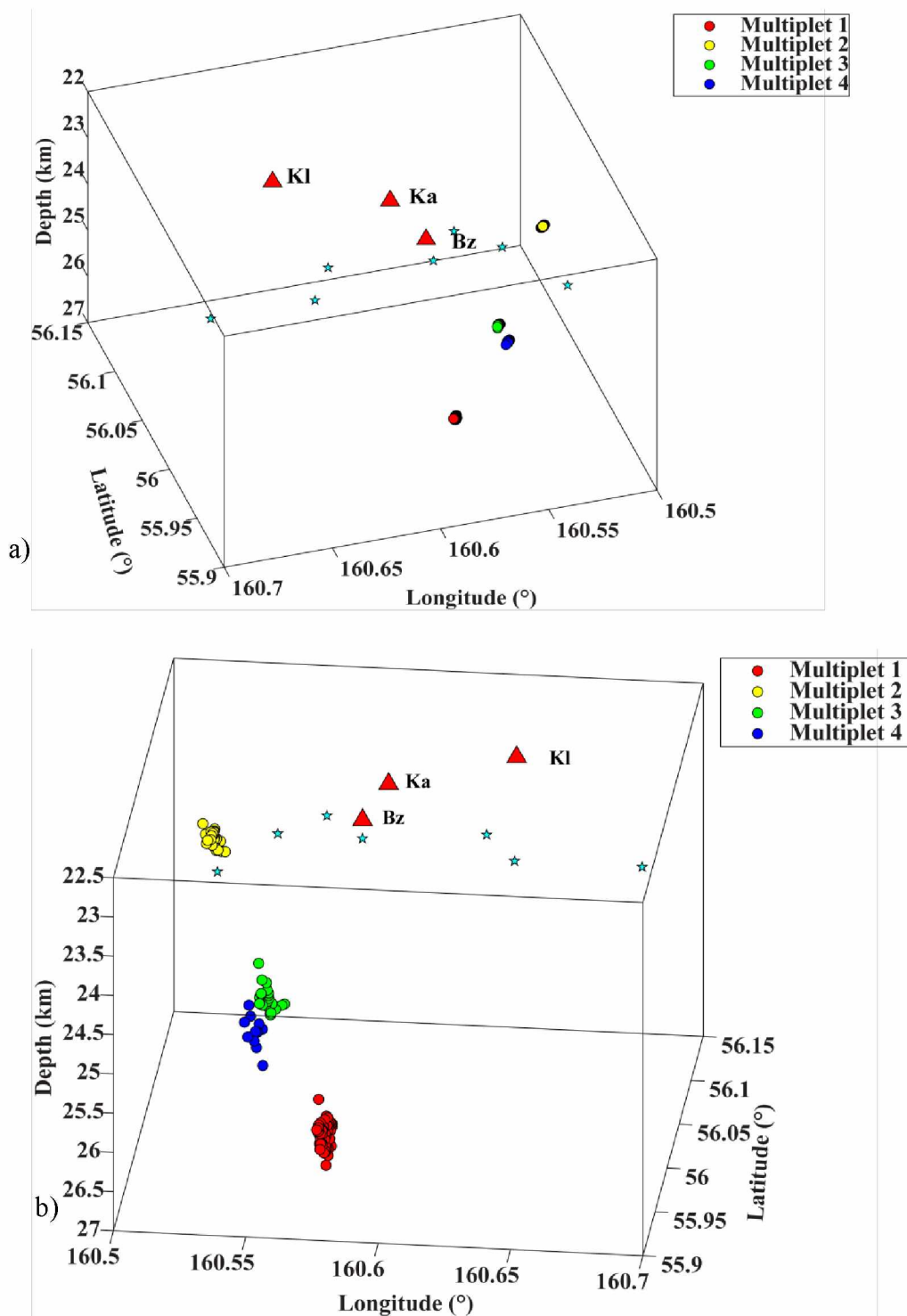
Figure 2.14 3D plots of new multiplet locations (a) locations using cross correlation and catalog data and (b) locations using just catalog data. Stars indicate station locations while the triangles labeled Bz, Ka and Kl show the locations of Bezymianny, Kamen and Klyuchevskoy respectively.
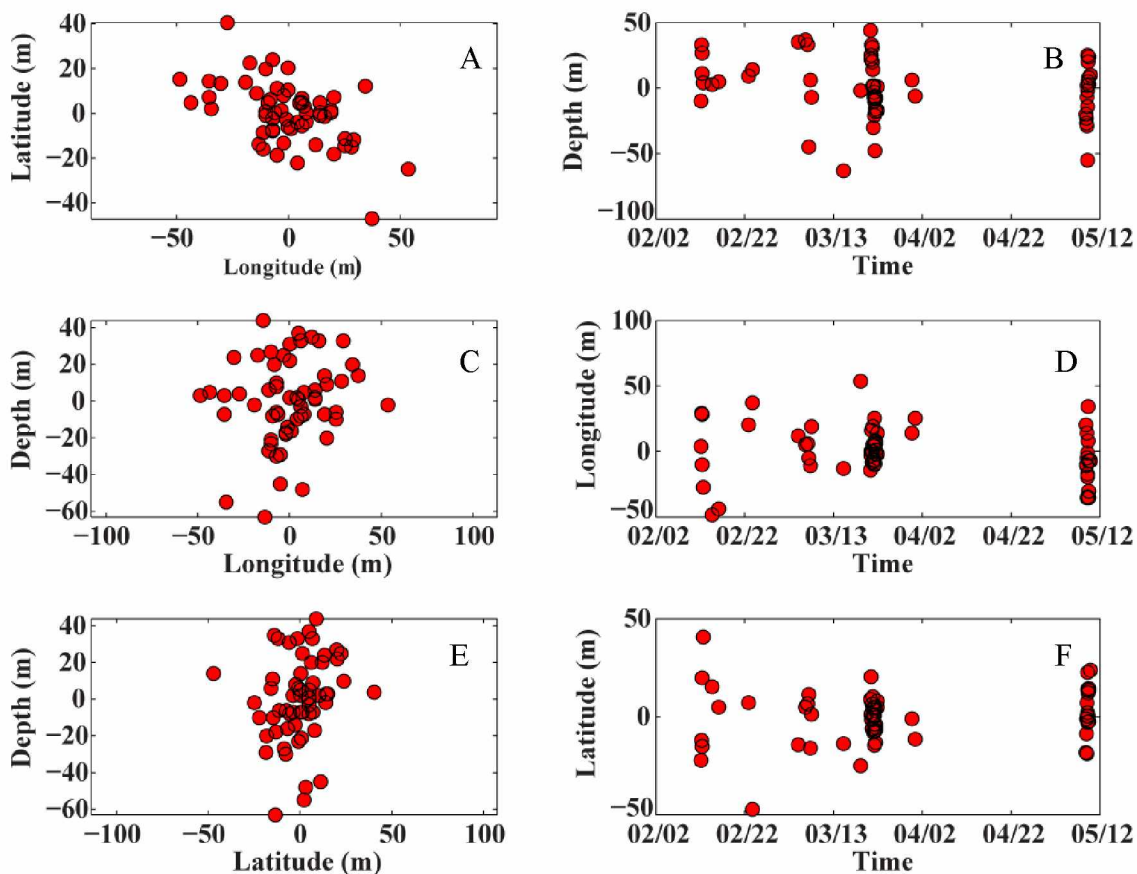
Figure 2.15 Location plots for multiplet 1. A) Map view of the events in this multiplet; maximum extent is in the longitudinal direction (~ 100 m). B) Time-Depth plot; this plot shows no real temporal changes in the event depth. Events are scattered in depth during the entire lifespan of the multiplet. C) Longitude-Depth plot; cloud is diffuse with no real pattern that can be discerned. D) Time-Longitude plot; from this plot, no temporal changes with longitude can be seen. E) Latitude-Depth plot-the bulk of the events in this cluster are within a 50 m latitudinal spread; maximum extent is in depth (~ 100 m). F) Time-Latitude plot—there is no latitudinal variations with time. Events are plotted relative to the center of the cluster.
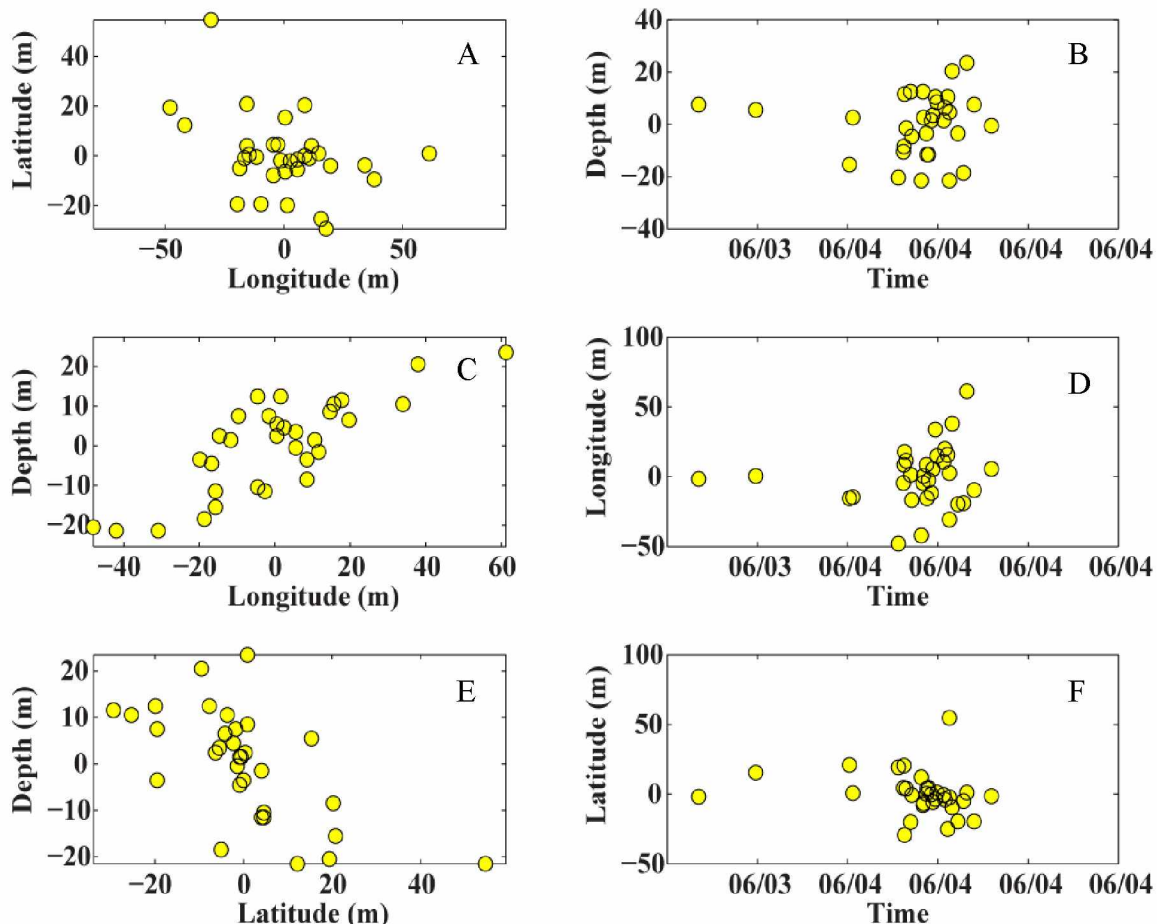
Figure 2.16 Location plots for multiplet 2. A) Map view of the events in this multiplet; maximum extent is in the longitudinal direction (~ 100 m); the majority of the events occur at the same latitude.. B) Time-Depth plot; this plot shows no real temporal changes in the event depth. Events are scattered in depth during the entire lifespan of the multiplet. C) Longitude-Depth plot; variation of longitude with depth is visible in this plot. D) Time-Longitude plot—a shift in longitude with time is visible in this plot particularly towards the end of its lifespan. E) Latitude-Depth plot -events in this cluster show a slight change in latitude with depth; maximum extent is in depth (~ 100 m). F) Time-Latitude plot— temporal variation in latitude visible here; variations occurs towards the end as was the case in D. Events are plotted relative to the center of the cluster.

Figure 2.17 Location plots for multiplet 3. A) Map view of the events in this multiplet; the bulk of the cluster has the similar extents in both latitude and longitude (~60 m). B) Time-Depth plot; events in this cluster are initially concentrated in a 20 m depth slice but eventually become more scattered with time. C) Longitude-Depth plot; the majority of the events in this cluster tend to be located at the same depth; variations in this depth locations comes with greater longitudinal distances. D) Time-Longitude plot—a shift in longitude with time is visible in this plot particularly towards the end of its lifespan. E) Latitude-Depth plot—the majority of events in this cluster tend to be confined to a small depth slice of about 20 m although there is some scatter present in the plot. F) Time-Latitude plot—temporal variation in latitude variations occurs towards the end as was the cases in D. Events are plotted relative to the center of the cluster.

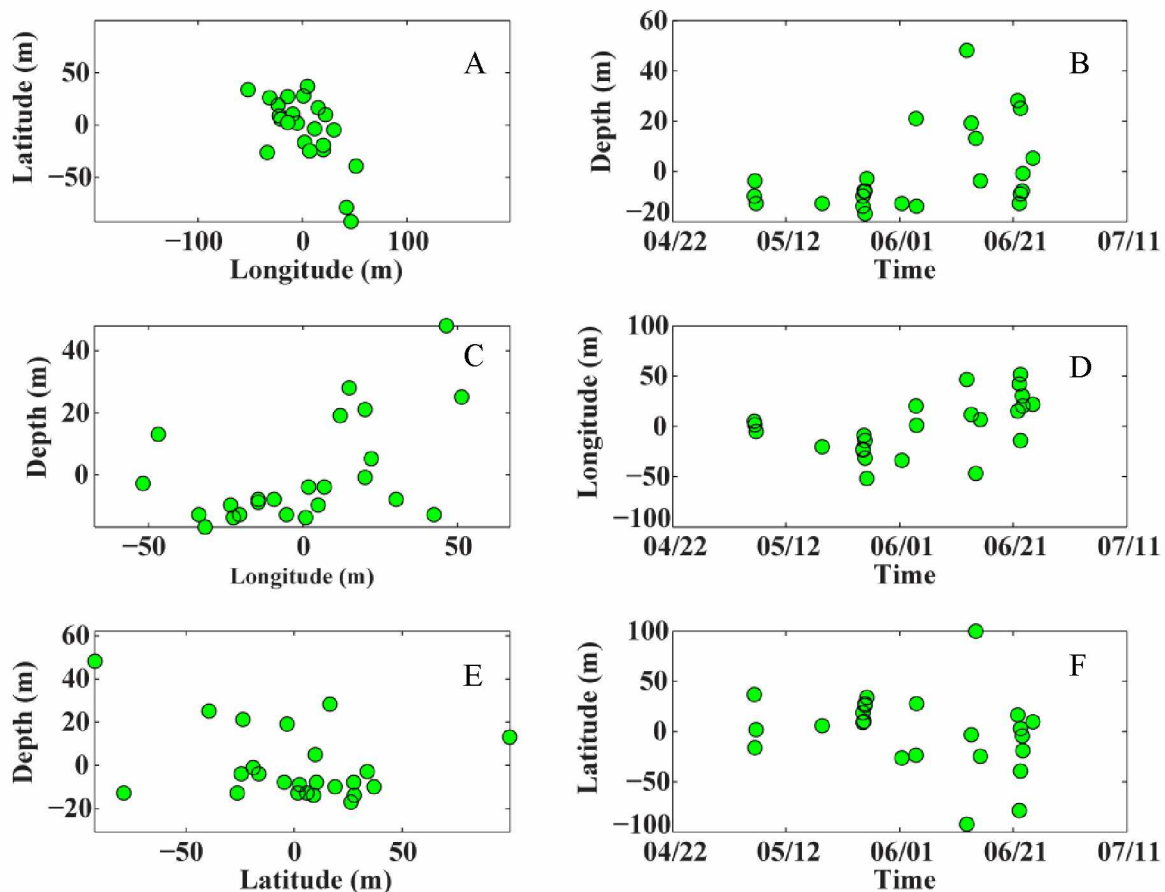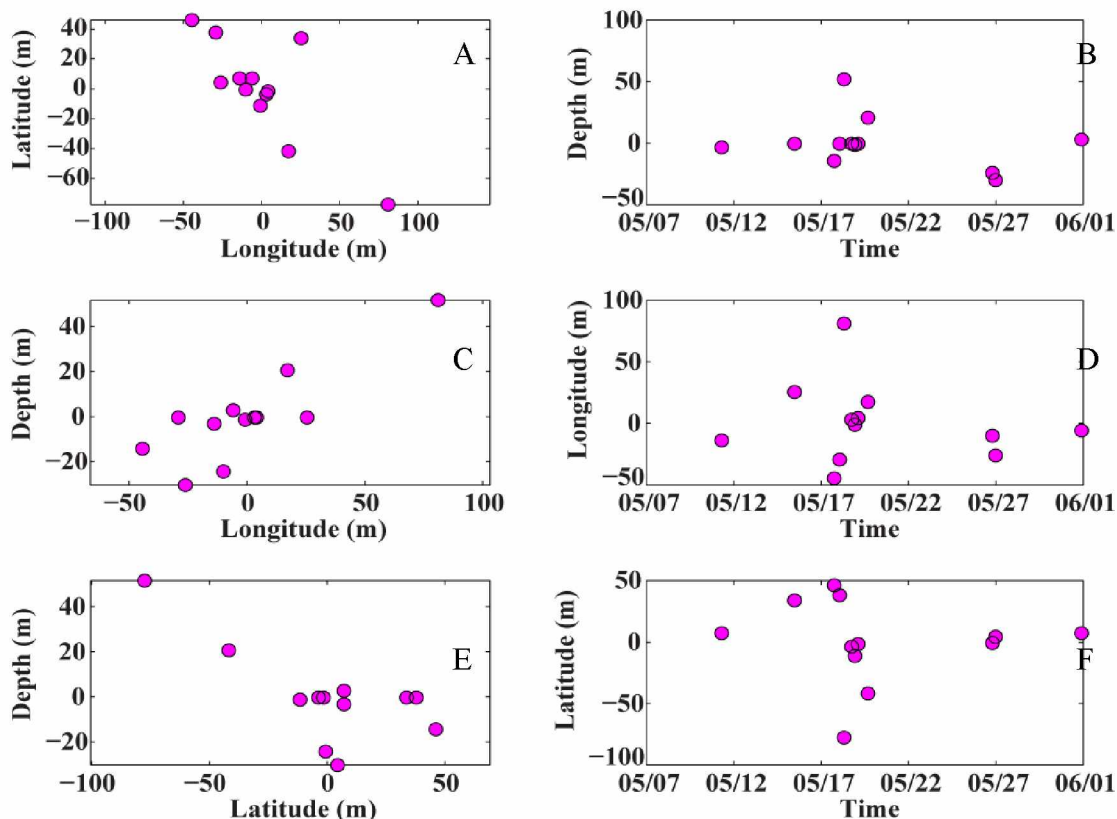Figure 2.18 Location plots for multiplet 4. A) Map view of the events in this multiplet. Events in this family have similar extents both in latitude and longitude; with the exception of one event, they can be placed in an 80x80 m region. B) Time-Depth plot; this plot shows no real temporal changes in the event depth. Most events occur at the same depth during the entire lifespan of the multiplet. C) Longitude-Depth plot; variation of longitude with depth is visible in this plot—longitudinal distances increases as depth increases. D) Time-Longitude plot—there is no temporal variation in longitude for this multiplet. E) Latitude-Depth plot-most of the events here occur at a set depth and within 20 meters of each other. F) Time-Latitude plot—there is no temporal variations in latitude seen in this multiplet. Events are plotted relative to the center of the cluster.

From the figures 2.15 to 2.18 it can be seen that most of the clusters map out features which are roughly 100 m in each direction. There is no real time-depth variation in any of the plots above; events in each cluster tend to occur at varied depths throughout their period of activity. A study of earthquakes due to brittle failure by Hill (1976) showed that an M_L 2 earthquake corresponds to a rupture area of 85 m; this value is generally in keeping with the dimensions shown for the multiplets and the earthquake magnitudes shown for these events in figure 1.8 b.

Chapter 3 Analysis of Mount Spurr data

3.1 *INTRODUCTION*

The second dataset in this study comes from Mount Spurr, Alaska, a 3,374 m andesitic stratovolcano which began forming before 255,000 yrs ago (Nye & Turner, 1990). Sometime within the last 58,000 yrs but prior to the Holocene, ancestral Mount Spurr underwent a sector collapse and lateral blast. In the caldera breach, the proto-Crater Peak, site of all historic eruptions to date, was formed. Eruptive activity continued at the main summit and on Crater Peak intermittently for the next few thousand years until about 5200 yrs ago when activity stopped at the main summit vent. During their coeval stage, these two vents produced significantly different magmas, a more silicic andesite at the summit vent and a basaltic-andesite at the satellite cone, Crater's Peak (Nye & Turner, 1990).

The difference in eruptive discharge seen at the different vents of Mount Spurr is similar to the behavior of Klyuchevskoy and Bezymianny which are located about 10 km from each other. Bezymianny erupts primarily basaltic-andesites while Klyuchevskoy's chief product is a high magnesian calc-alkaline basalt. These similarities in eruptive behavior and their abundance of deep seismicity make these volcanoes prime targets for a comparative study.

3.2 *THE DATA*

Beginning in early July 2004, the formation of an ice cauldron in the main summit, coupled with an elevation in deep seismicity rates, raised concern levels at the

Alaska Volcano Observatory (AVO). Increased activity, both surficially - debris flows as long as 1000 m, increased SO_2 emissions and the expanding ice cauldron (which served as an indication of increase heat flux) (Coombs et al., 2006), along with the increased deep seismicity, lead to an augmentation of the existing network on the volcano.

During the summer of 2005, AVO deployed a set of 12 broadband, three-component campaign seismometers in an effort to improve the locations of deep events and to gain research quality data in the event of an eruption. Figure 3.1 shows a map of station distribution during summer, 2005; stations labeled SP01-SP12 are the campaign stations.
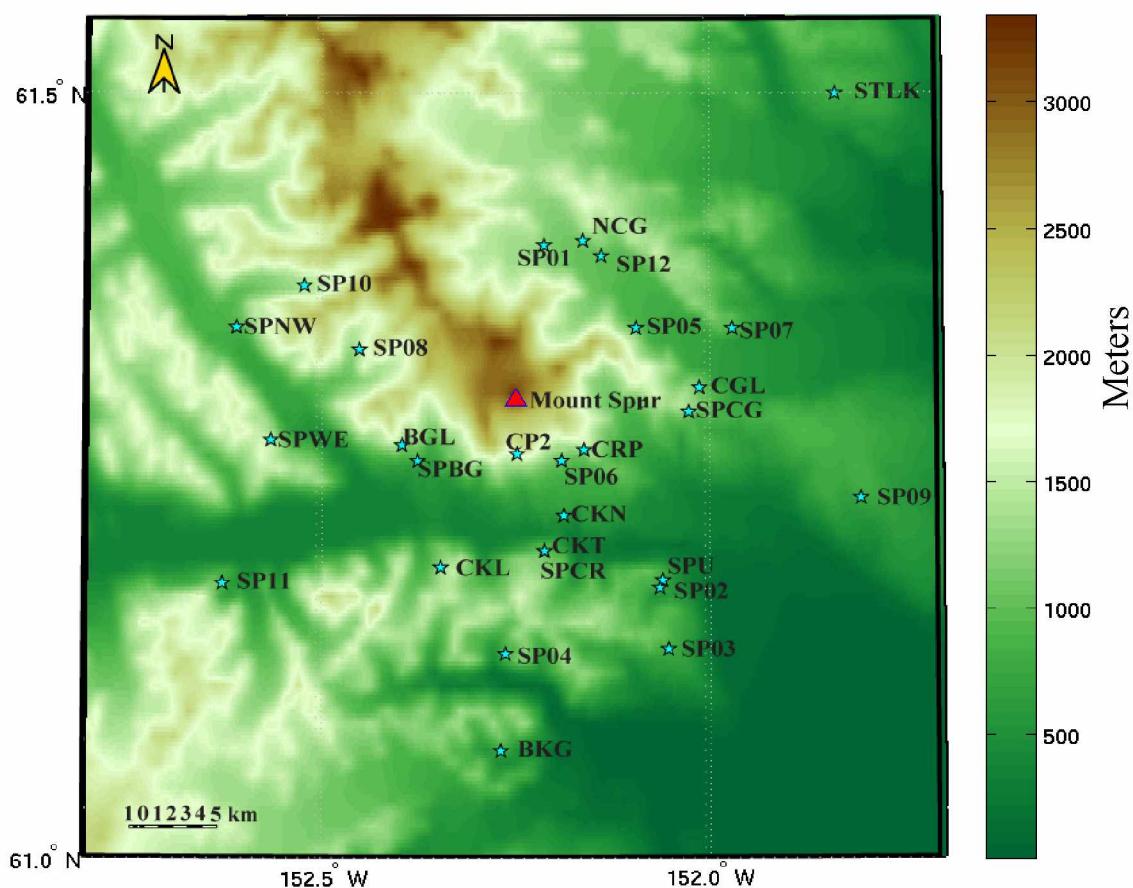
Figure 3.1 Map of Station distribution on and around Mount Spurr in summer 2005. Stations labeled SP01-SP12 are campaign broadband sensors deployed for 4 months from 06/01/2005 to 10/01/2005

Data from this deployment, which lasted 4 months, along with continuous waveform data from telemetered stations in operation at that time and a catalog of origin times, location and arrival times has been compiled. In this chapter a comparison of this compiled data alongside that from the 1992 eruption of Crater Peak as well as that from the first data set is presented.

3.3 *CHARACTERIZATION OF DEEP SEISMICITY BENEATH MOUNT SPURR*

Deep seismicity beneath Mount Spurr does not occur continuously but tends to be concentrated at two specific intervals. The first period of heightened activity is associated with the 1992-1993 eruption of Crater Peak while the second is associated with the 2004-2006 unrest episode. This pattern is best seen in the time depth plot shown in figure 3.2 below. It should be noted that these periods of heightened activity followed the eruptions in 1992 as well as the first manifestations of unrest during the 2004-2006 episode.
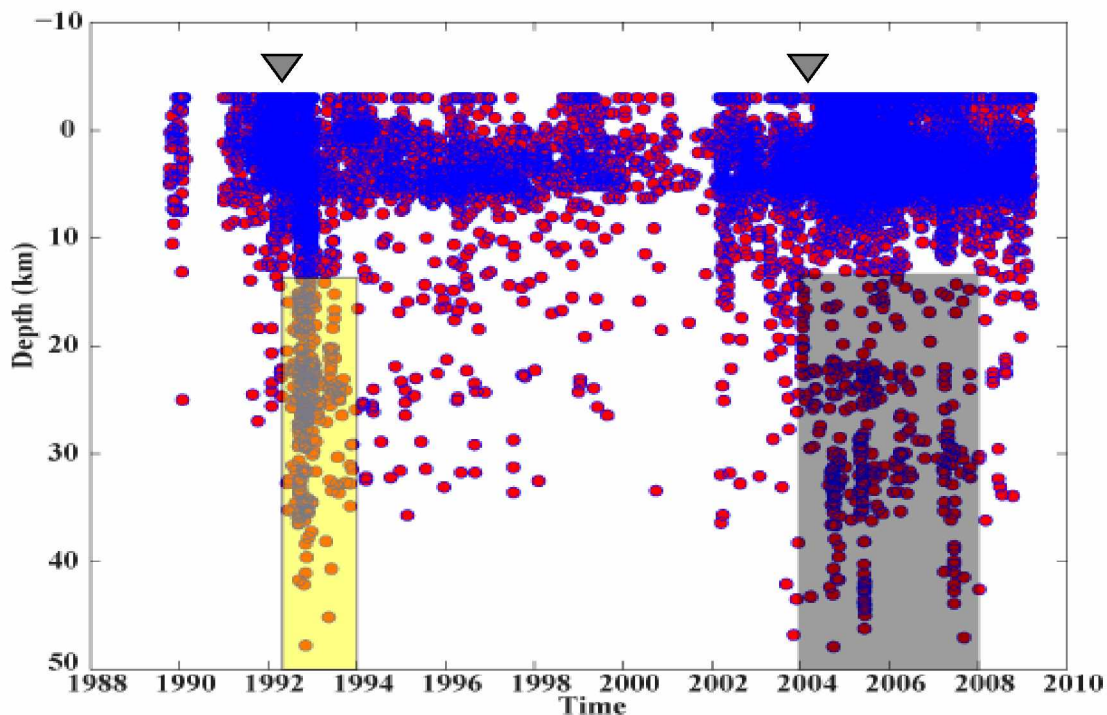
Figure 3.2 Overall seismicity beneath Mount Spurr — note that the bulk of deep seismicity is associated with the 1992 eruption **of Crater's Peak** and the 2004-2006 period of unrest. The purple triangles mark the 1992 eruption and the onset of surficial expression of the 2004-2006 unrest. The shaded regions highlight two periods of heightened deep seismicity.

The cumulative seismicity rates for the two periods of heightened deep seismic activity highlighted in figures 3.2 is shown in figure 3.3. This plot shows a slight variation in the seismicity rates between the two periods in question. The graphs shown in figure 3.4 provide a more detailed look at this comparison. Though the difference is slight, there is still a noticeable change in the rate of seismic activity with the 2004-2006 period of unrest when compared with that associated with the 1992 eruption of Crater's Peak. The 1992-1994 period is marked by a greater number of smaller events than the 2004-2006 period.
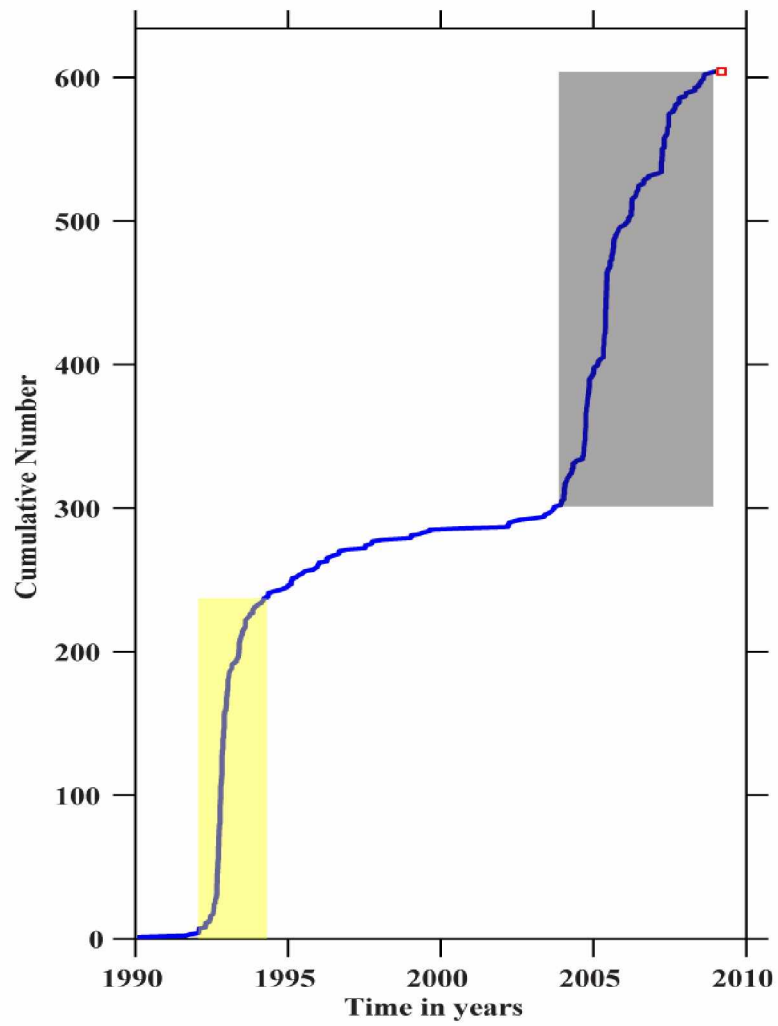
Figure 3.3 Cumulative seismicity plot for deep events beneath Mount Spurr. The shaded regions in the plot highlight periods of elevated deep seismicity rates from 1992-1994 and 2004-2008.
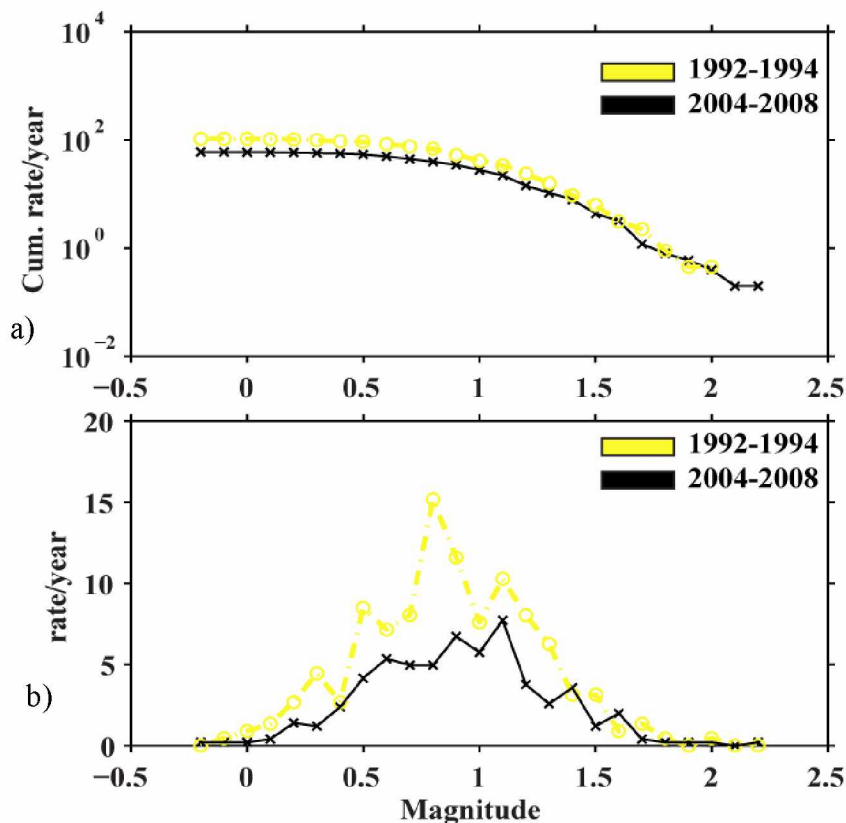
Figure 3.4 Comparison plot of the deep seismicity rates at Mount Spurr from 1992-1994 (yellow trend lines) and from 2004-2008 (black trend lines). (a) Shows the cumulative rate/year versus magnitude. (b) The rate/year versus magnitude is shown. While the rate change is small, there is still a notable difference in the rate of activity during these two periods. Elevated seismic rates in the 1992-1994 period are accompanied by a greater number of small events than was recorded during the 2004-2008 period.

3.3.1 Event types in the Mount Spurr dataset

Within the Spurr deep dataset, there is a high degree of variability both in the event classes present and in the appearance of individual events within those classes. Though long-period events still make up a significant component of the catalog, the Spurr dataset contains high-frequency and hybrid events as well. High-frequency events are traditionally associated with shear slip on a fault surface and commonly have a broadband spectral signal with peak frequency in the 5-10 Hz range. Hybrid events combine properties of LP and HF waveforms and are marked by a high-frequency onset

followed by an extended low-frequency coda. An example of each event type occurring beneath Mount Spurr is shown in figure 3.5. The variability in the Mount Spurr catalog is unlike the case with the KVG catalog in which waveforms are dominantly long-period events of similar appearance.
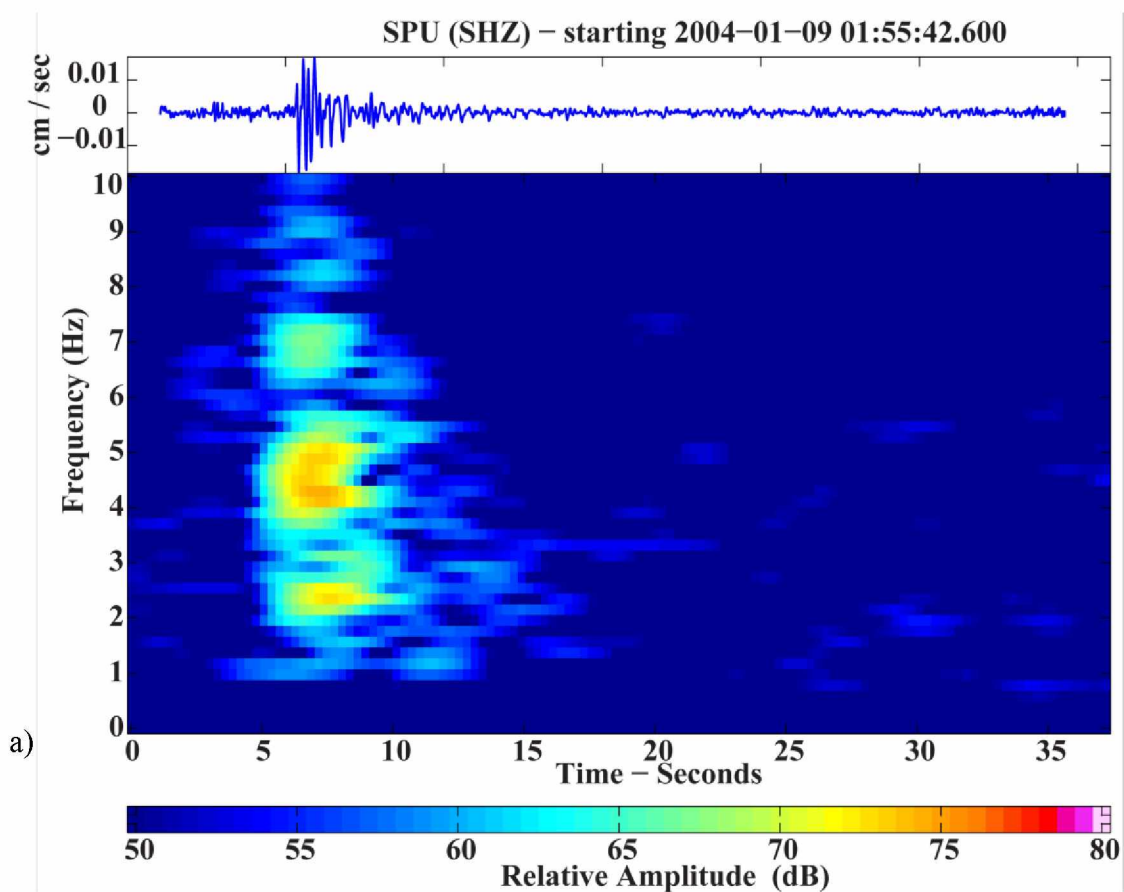
Figure 3.5 Spectrograms of different types of deep events recorded beneath Mount Spurr along with corresponding waveform. (a) Spectrogram of a deep high-frequency event located at 22 km beneath sea level. This event has a broadband energy signal. (b) This hybrid event, located at 48 km is characterized by the broadband nature of the onset, peak energy at about 2.5 and 8 Hz and the extended low frequency coda following the P and S waves. (c) A DLP event located at 22 km with strong spectral peak at about 2 Hz; energy above this is very diffuse.

SPU (SHZ) − starting 12−Jun−2005 22:34:41.780

b)

SPU (SHZ) − starting 25−Aug−2005 14:28:02.779

c)
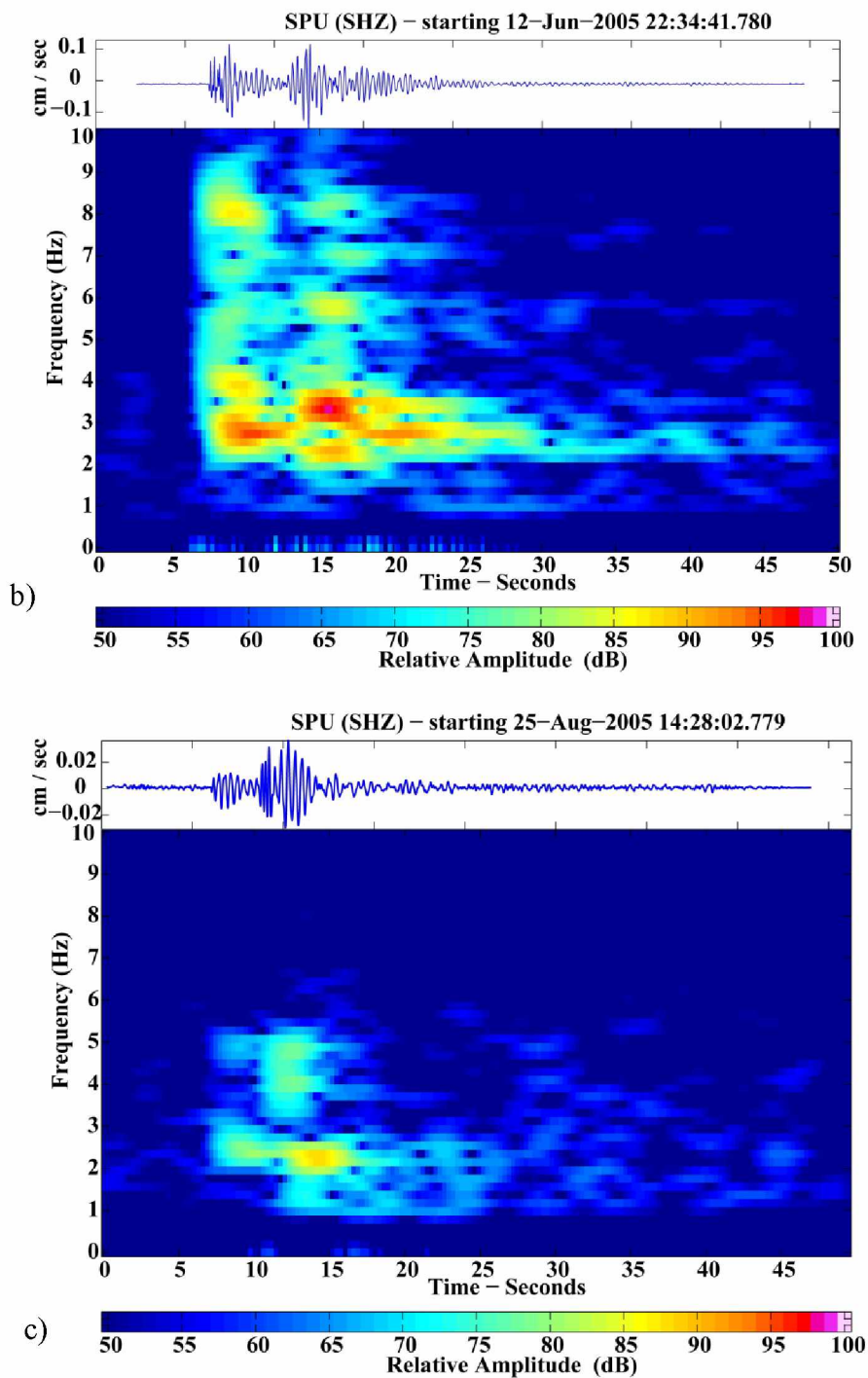
Figure 3.5 continued

The presence of these waveforms with high-frequency contents at the same depths

as the long-period events adds credence to long-period waveforms seen here being the

genuine result of some distinct source processes rather than a function of attenuation or other path effects. Both the long-period and the high-frequency event shown in figure 3.5 above occurred at a depth of about 22 km while the hybrid event has a depth of 48 km.

3.3.2 Event Amplitudes and Magnitudes

Deep events beneath Mount Spurr tend to be relatively small with magnitudes running from 0 to 2 M_L. Figure 3.6 shows a histogram of magnitude distribution beneath Mount Spurr both for the 1992-1994 eruptive period and the 2004-2005 unrest period; as previously noted, there was a greater abundance of small events during the 1992 Crater Peak eruption than during the 2004-2006 period of unrest.
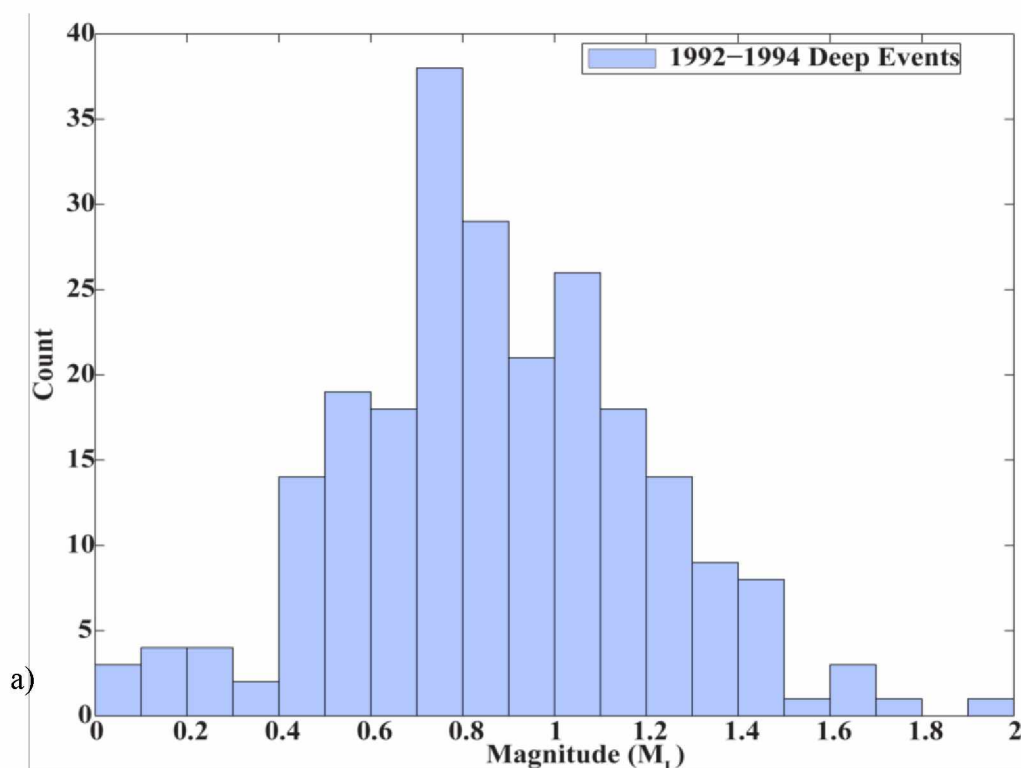
Figure 3.6 Plot of magnitude distributions of events beneath Mount Spurr. (a) Magnitude distribution for deep events occurring during and after the 1992 eruption of Crater's Peak. (b) Magnitude distribution for deep events during the 2004-2006 period of unrest.
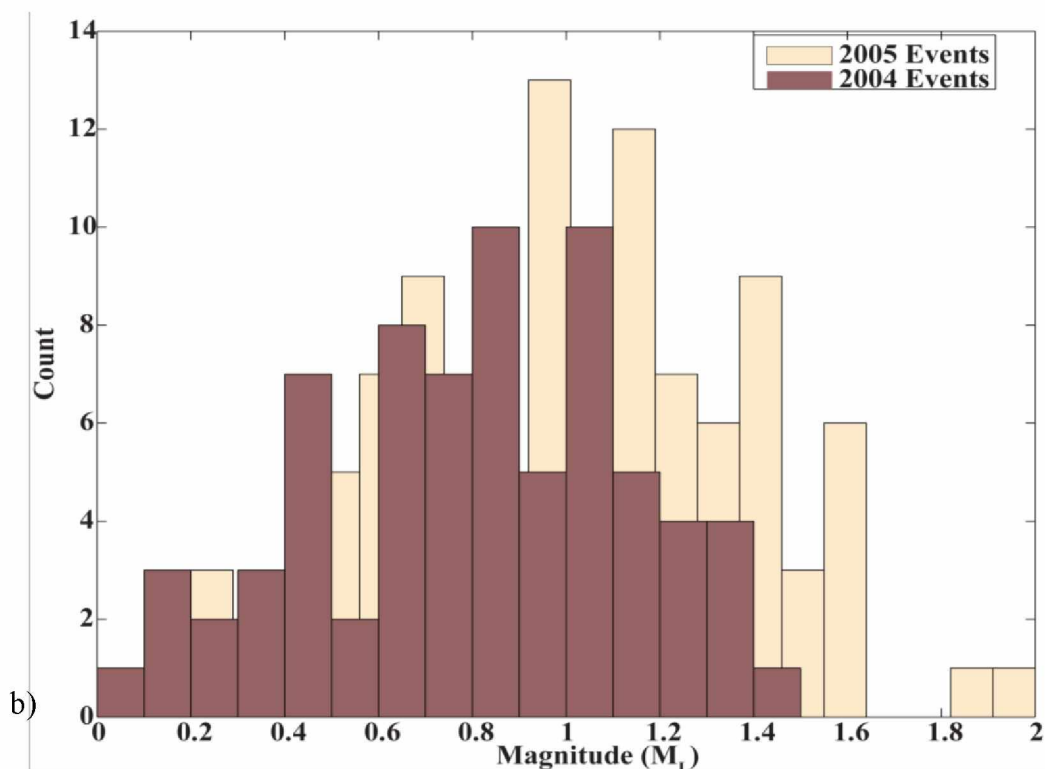
Figure 3.6 continued

Event magnitudes at Spurr run between 0.3 and 0.5 units less than those recorded beneath the KVG. As mentioned in section 1.3.3, many factors influence the estimated magnitudes, however, this occurrence may be explained by the difference in magnitude calculation algorithms used. When the plot in figure 3.7 is compared with figure 1.3 in section 1.3.1, it can be seen that the scaling of amplitude with distance at both sets of volcanoes follow similar patterns. In both cases, most of the events occurring at distances greater than 20 km from the station do not produce ground displacement amplitudes greater than 20 nm.
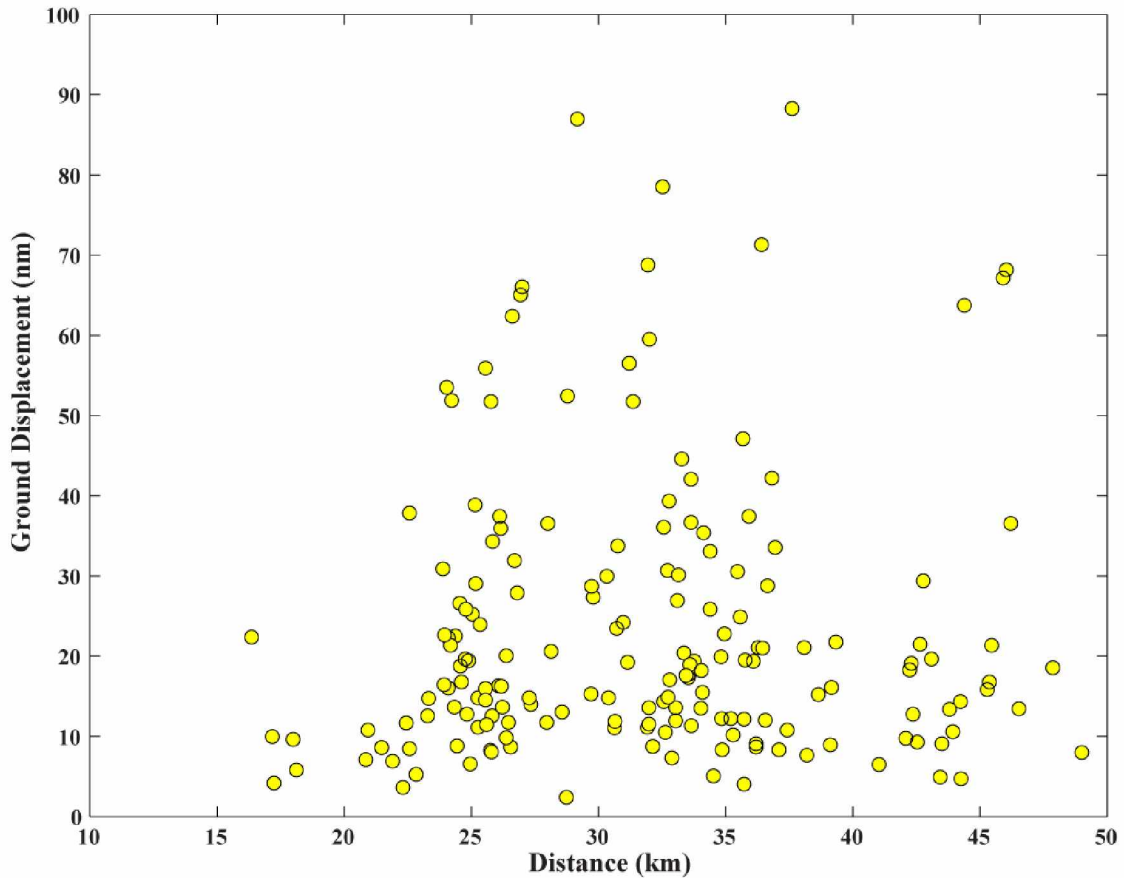
Figure 3.7 Amplitude distribution plot for events at Mount Spurr from 2004 – 2005 recorded on station SPU. Greater than 50 % of the events in this plot produce ground displacements of less than 20 nm.

3.4 FOCAL MECHANISMS

The ability to derive valid focal mechanisms on these types of events is made difficult by their emergent nature. In determining a focal mechanism, the first P wave motion at each station is documented. An upward first motion represents a compression as the ground moves away from the event and towards the station. A downward first motion represents a dilatation; in this case the ground moves away from the station. Several challenges were presented when attempting to calculate focal mechanisms for the deep events in these datasets:

- Data recorded on the Mount Spurr network is often noisy so waveforms lack the coherence necessary to make a definitive judgment of first motion.

- Station distribution on good events is often inadequate to cover the entire focal sphere. This is particularly the case for the PIRE network since the azimuthal coverage of stations is limited.

- Raw broadband data in the KVG data set is dominated by a long period signal between 0.5 – 1 Hz. Therefore no focal mechanisms were determined for this data set.

A graphical representation of an earthquake's focal mechanism is usually provided by a "beachball diagram". This diagram is created manually using a lower hemisphere equal area stereographic projection such as the one shown in figure 3.8. Using the event and station locations, the event to station azimuth and the take off angle is calculated for each station. The azimuth is the direction in which the ray travels from the earthquake focus to the station while the take off angle is the angle that the ray makes with the vertical as it leaves the earthquake. Take off angles are usually estimated from the distances between the event and stations using tables such as table 8.1 in Lay and Wallace (1995).

Once the azimuths and take off angles have been calculated for each station, that information is plotted on the stereonet. This is done by first marking the azimuth by counting the degrees from north along the outer edge of the stereonet. The take off angles are plotted by counting the degrees from the center of the stereonet outwards. Compressions are plotted as solid circles while dilatations are plotted as open circles.

After all the data has been added to the stereonet, it is rotated to find the best fit great circle which separates the dilatations from the compressions. This line represents one of the possible fault planes for that particular earthquake. The second possible fault plane is at 90° from this first plane. The diagram is then shaded in so that regions which contain only dilatations are colored white while those that contain compressions are colored black. A schematic of this process is shown in figure 3.8 below.
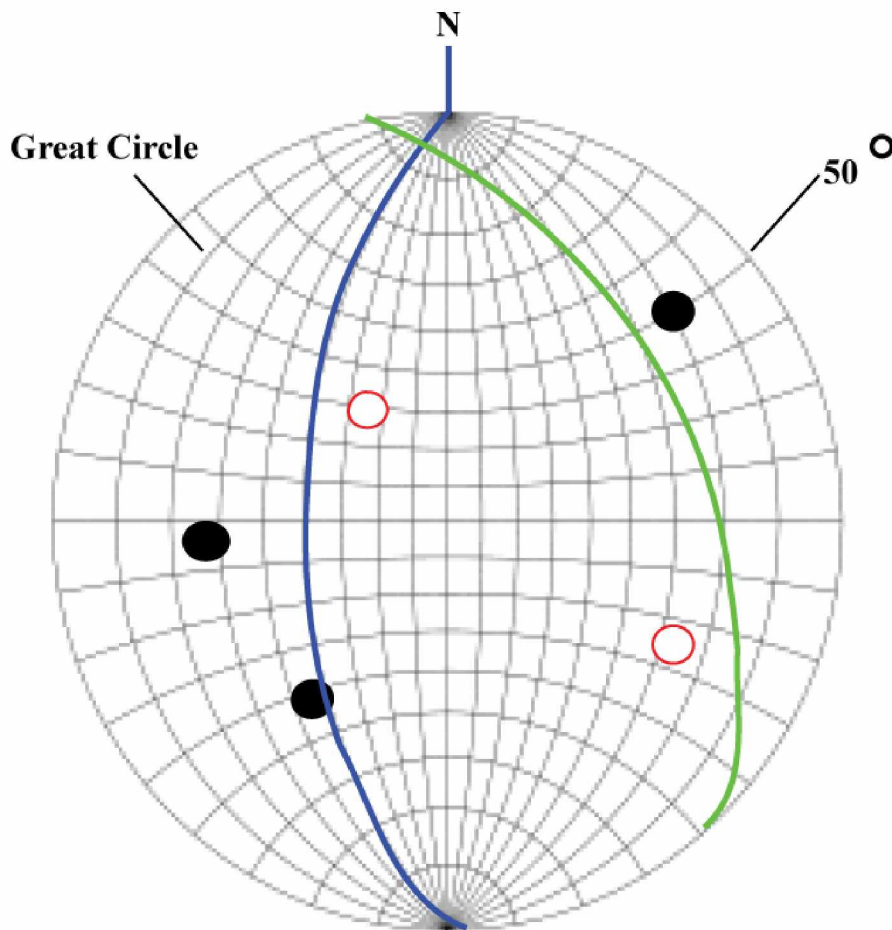
Figure 3.8 A schematic focal mechanism diagram. The azimuth for the station is plotted by counting the degrees from north (50° indicated on the plot) while the take off angle is found by counting the degrees from the center of the stereonet. The first fault plane (blue) is found by finding the great circle which best separates the dilatations from the compressions. The second plane is plotted 90 degrees from the first.

As a result of the difficulties highlighted above, determination of focal mechanisms was only possible on one of the events in these two large data sets. This mechanism corresponds to a deep hybrid event with a catalog depth of 29.7 km occurring beneath Mount Spurr on September 30th 2004. This mechanism is shown in figure 3.9; such a focal sphere is produced by normal faulting on one of two possible faults, the first with a strike, dip and slip of 22°, 60° and -36° respectively. The second possible plane defined by this diagram has a strike, dip and slip of 320°, 40° and -50° respectively.
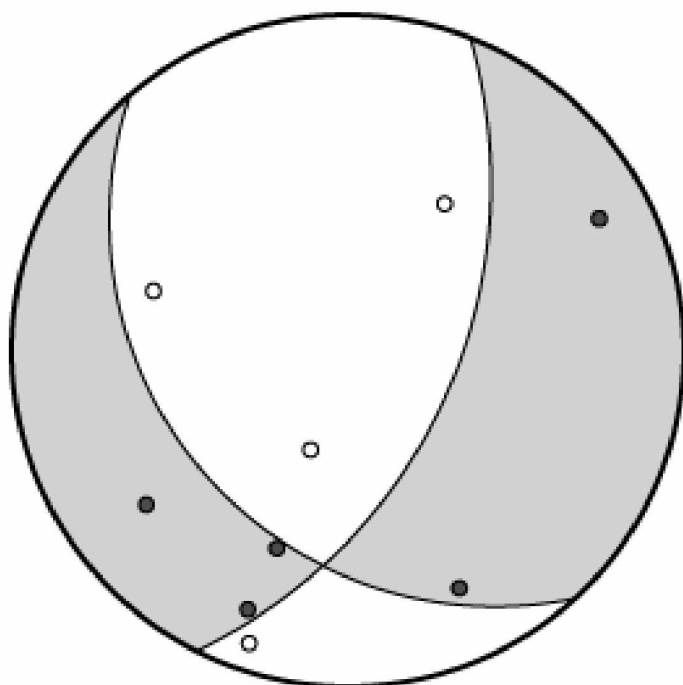
Figure 3.9 Lower hemisphere focal mechanism for a deep hybrid event beneath Mount Spurr occurring on 09/30/2004. Such a mechanism is produced by normal faulting. Regions in grey with black circles represent compression while white region with open circles represent dilatations.

Should this event prove to be representative of the other events occurring at these depths beneath Mount Spurr, there are important implications which can be drawn about processes here. The fault plane solutions represented by the focal mechanism above support either extension in the east-west direction or fracturing along a north-south

striking dike. As pointed out in the thesis introduction, magma ascent is purported to take place in a locally extensile setting. Hence, both of these faulting mechanisms would facilitate magma transport beneath the volcano. The focal mechanism above therefore provides insights into the possible magma propagation direction beneath Mount Spurr should it prove to be representative of the other mechanisms at these depths.

3.5 *THE SEARCH FOR MULTIPLETS WITHIN THE SPURR DATA SET*

A similar cross correlation study to that done in section 2.2 was conducted on the Mount Spurr data set using permanent short period station SPU. The main aim of this analysis was to glean whether or not there were any repeating events between the deep events occurring during the 2004-2006 period of unrest and those which accompanied the 1992 eruption of Crater Peak. To achieve this, waveform data recorded on SPU for deep events occurring in 1992-1994 were added to that from deep events recorded during the unrest period. This data set contained 373 events with catalog depths greater than 15 km. When events with a cross correlation coefficient of 0.7 were selected in a procedure similar to what was detailed in section 2.2 for the PIRE data, the largest cluster found contained only 17 members. Members of this cluster, however, contained events from 1992-1994 as well as three others occurring between 2004 and 2005. An interferogram of this cluster is shown in figure 3.10.
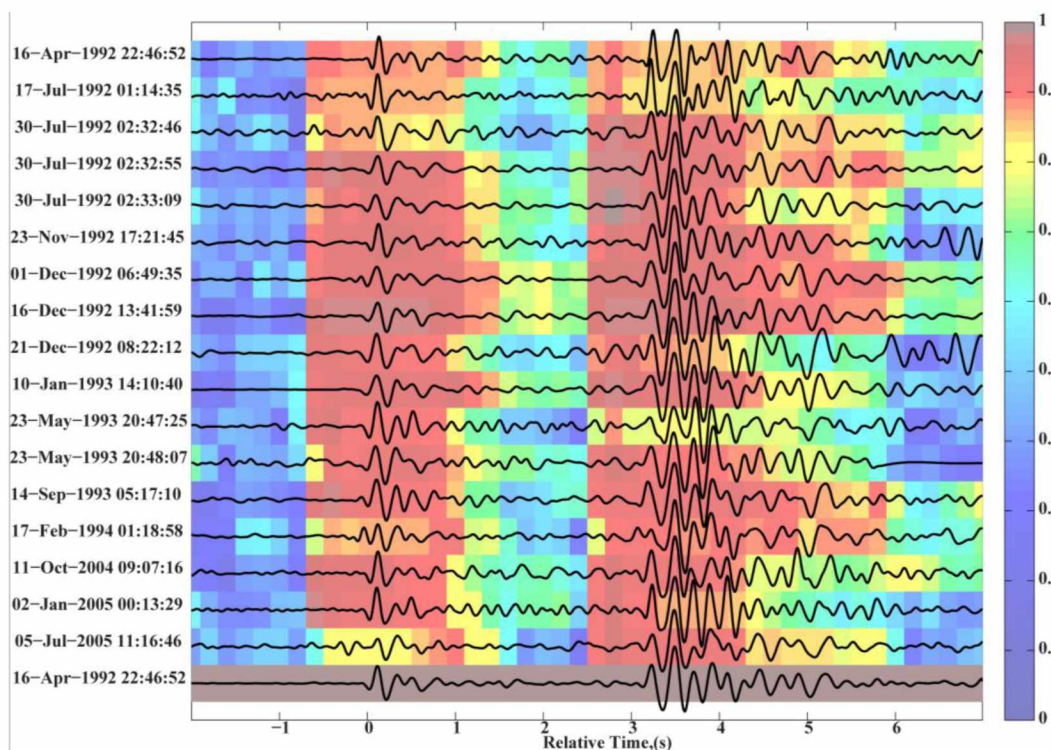
Figure 3.10 Interferogram for largest cluster of events with cross correlation coefficient of 0.70 occurring beneath Mount Spurr. Events in this cluster occur during 1992-1993 and between 2004 and 2005.

The events which occur in 2004/2005 show as high a degree of correlation with the master event as do the ones which occur earlier. Such similarity of events across such a long time scale, which has rarely if ever been demonstrated, lends credence to the idea of a long lived source region being reactivated by the injection of new magma. Few processes which are responsible for generating seismic signals could produce similar signals across long time spans as their very nature leads to the destruction of the structures on which they act. Injection of magma into a preexisting crack system would likely generate high-frequency and hybrid events as the system is reopened. Following this reactivation, the long-period events which are associated with the magma migration would remain relatively unchanged from previously observed. This is because the length

and location of the cracks would remain relatively unchanged so there would be little alteration of the ray paths or the source process which were associated with the earlier signals.

3.6 *REEVALUATING LOCATIONS AT MOUNT SPURR FOR EVENTS OCCURRING DURING THE SUMMER OF 2005*

In the Mount Spurr data set, continuous waveform data from permanent telemetered stations were supplemented with data from campaign broadband sensors. Data from the permanent installations also included AVO catalog information such as P and S wave arrival times as well as origin locations and times. As a starting point in adding picks to the campaign data, a subset of this data was used to narrow down times when deep events occurred. P and S arrival picks were added to the vertical and horizontal channels of the campaign stations respectively. A scan of the waveform data recorded on these instruments did not show many deep events which were missed during analysts review of the permanent data. Following the addition of these new arrival picks, new event locations were calculated using dbloc2. The 4 layer 1D velocity model used to calculate these locations is shown in table 3.1.

Table 3.1 1D velocity model for Mount Spurr used in calculating event locations (Dixon et al., 2008). Here Vp represents the P wave velocity while Vs represents the S wave velocity.

Layer number	Vp (km/sec)	Top of layer (km)	Vp/Vs
1	5.1	-3.00	1.81
2	5.5	-2.00	1.81
3	6.3	5.25	1.74
4	7.2	27.25	1.78

The sdobs (see section 2.3 pg 39 for definition) for the recalculated locations in this small data set ranged between 0.14 and 2.31 while the depth errors ran from 0.08 to

3.32 km. A cross sectional view of the event locations is shown in figure 3.11. Plot A shows the original catalog locations calculated by AVO analysts. In B, recalculated locations for a few of these events are shown while C shows the altered cross section when the original event locations in A are replaced by the locations for the corresponding events shown in B.
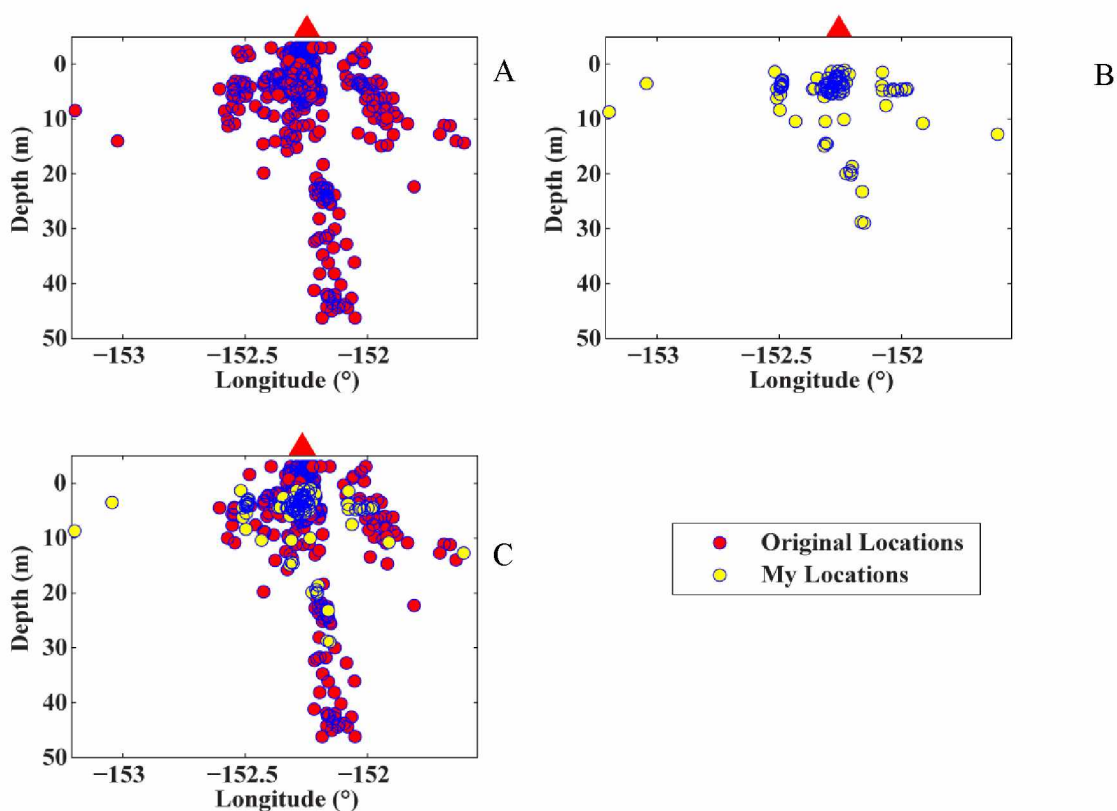
Figure 3.11 Cross sectional plots of seismicity beneath Mount Spurr. A) Longitudinal cross sectional view of original AVO catalog locations. B) New locations calculated using data from the campaign stations for a subset of the events in plot A. C) The location plot in A altered by switching the original locations with those calculated in plot B. The red triangles denote the location of Mount Spurr.

The addition of the new picks to the existing catalog did not improve the event locations for this data set. When compared to event locations by AVO analyst, dbloc2 locations were generally shallower (2-10 km) but there was no significant refining of the spatial extent.

CONCLUSION

The pulsing pattern of deep seismicity beneath both of the volcanic regions under study is a notable feature of these data sets which has rarely been shown elsewhere. Deep seismicity occurs not on a continuous basis but in large clusters which may last for several weeks to months before activity goes into hiatus. Within these clusters, a large number of events share a high degree of similarity in amplitudes, frequencies and general appearance on visual inspection. In the KVG data set, which is comprised mainly of low frequency events, this similarity between waveforms exists not only on a particular station but between stations across the PIRE network.

Quantification of this similarity, through waveform cross correlation analysis of data from the PIRE and Mount Spurr seismic networks, grouped many of these events into distinct families with life spans lasting several months. In the Mount Spurr data set, such a family was found with members occurring both following the 1992 eruption of Crater Peak and during the 2004-2006 episode of unrest. Such longevity of families points towards events being generated by a relatively non-destructive source which even after a hiatus of several years can continue to produce similar events. The generation of high-frequency earthquakes is related to brittle rock failure; such a process would result in the destruction of the source and is therefore not expected to produce repeated waveforms. Long-period earthquakes on the other hand, are attributed to fluid oscillation in a resonating crack; such a process does not generally result in the destruction of the source region. The fact that the events beneath Mount Spurr spans more than a decade indicate that the source region remains relatively stable and adds another line of evidence

that the long-period nature of the signals are related to the source and not path effects such as attenuation.

Finally, high precision earthquake relocation showed these families to be located in small pockets with a maximum extent of about 100 meters in all three dimensions. In multiplets 1 and 2, the events tend to locate in an indistinct cloud; however, for multiplets 3 and 4 the bulk of the events define a body with its greatest extent in latitude and longitude with small variations in depth. There is no strong temporal depth variation within any of the clusters; in multiplets 1 and 3 there are periods where activity is strong for 1-2 days followed by relative quiescence. The event clusters have locations between 22 and 27 km beneath sea level.

Annen et al. (2006) proposed a model for the generation of silicic magmas detailed the formation of a hot zone in the deep crust as a result of the release of heat by crystallizing sills. These sills are repeatedly emplaced at depths ranging from 20-30 kilometers and slowly evolve as they crystallize. A few of the bodies found in this study have been shown to have mainly a horizontal extent and may therefore be the seismic expression of small portions of these proposed sills. They may also highlight the seismicity which is associated with the melt segregation process as materials escape from these sills. A second model for deep magmatic processes discussed earlier was based on laboratory experiments by Connolly et al. (1997) who among others have shown that fluid induced hydrofracturing as a result of pressure building due to increasing melt content is possible at these depths.

When the intrinsic strength of the rock is surpassed, a system of randomly oriented cracks forms; this allows melt to flow out of their regions of generation and ascend into the shallower crust. The relocation results of multiplets 2-4 show a preferred alignment of these events which serves as an indicator of the stress and homogeneity states at depth. Dikes and sills tend to propagate in the direction of the most compressive stress and open in the direction of the least. Crack orientation is also an indicator of the degree of homogeneity of a medium; in a homogeneous medium, cracks tend to be more randomly oriented than in a heterogeneous one where material properties play a role in determining fracture paths.

This phenomenon is most likely the case with the Mount Spurr data set where an abundance of high-frequency and hybrid earthquakes are found in addition to deep long period events. Propagation of cracks due to fluid overpressure would lead to the generation of high-frequency events at the crack tip as rocks are fractured. Hybrid events would occur in close proximity to this advancing crack as the jerking motion of the opening mode fracturing sets the fluid oscillating. Long-period earthquakes would occur within the crack itself as the crack resonates while the fluid moves through it. A schematic of the probable earthquake generation mechanisms is shown in the figure C.1 below.

The final model addresses the cyclical pattern of melt segregation related to the generation of silicic melts–this process does not occur continuously but as alternating periods of melt segregation and matrix relaxation (Vigneresse, 2004). During each segregation cycle, only a small percentage of melt escapes from its generation zone

before that activity halts. The number of cycles is dependent on the availability of heat for additional melting. Vigneresse (2004) showed that compaction alone is not enough to drive melt segregation on the time scales necessary for eruptions. Given the similarities in the cyclic nature of deep seismic activity at both sets of volcanoes in this study and the expected cyclic pattern of melt segregation, it is likely that the deep events seen here are a manifestation of the melt segregation process.

1) Melt, denoted by red regions here, accumulates at multigrain (multi colored shapes) triple or quadruple junctions; μm scale

2) Fluid overpressure builds up as melt content increases. This leads to the creation of randomly oriented cracks due to hydrofracturing; meters to km scale

3) Fracturing of rocks at the crack tip produces high frequency earthquakes while the oscillation of the fluid caused by the crack propagation generates hybrid earthquakes.

4) Oscillation of fluids within the crack system leads to the generation of LP events.

Figure C.1 Schematic diagram of phenomenon related to the generation of deep events. Melt accumulated at grain boundaries eventually causes an increase in the fluid pressure which eventually leads to the generation of randomly oriented cracks. High-frequency events occur at the crack tip as rocks are broken; hybrids occur in close proximity to the advancing crack and long-period events, within the crack system. In the above figure, melt is shown in red while grains are shown as the multicolored shapes.

This pattern at arc volcanoes becomes more readily apparent when it is compared with the deep seismic behavior seen at Kilauea, a hot spot volcano. At Kilauea, which has been in a continuous state of effusive eruption since 1983 (Wolfe et al., 2004), events at depths greater than 13 kilometers tend to occur more continuously. Compare figure C.2 below with figures 1.10 and 3.3 above. If the assumption that deep seismicity at arc volcanoes is a manifestation of the segregation process is correct, then a probable relationship between eruptive cycles of arc volcanoes and deep seismicity can be surmised.
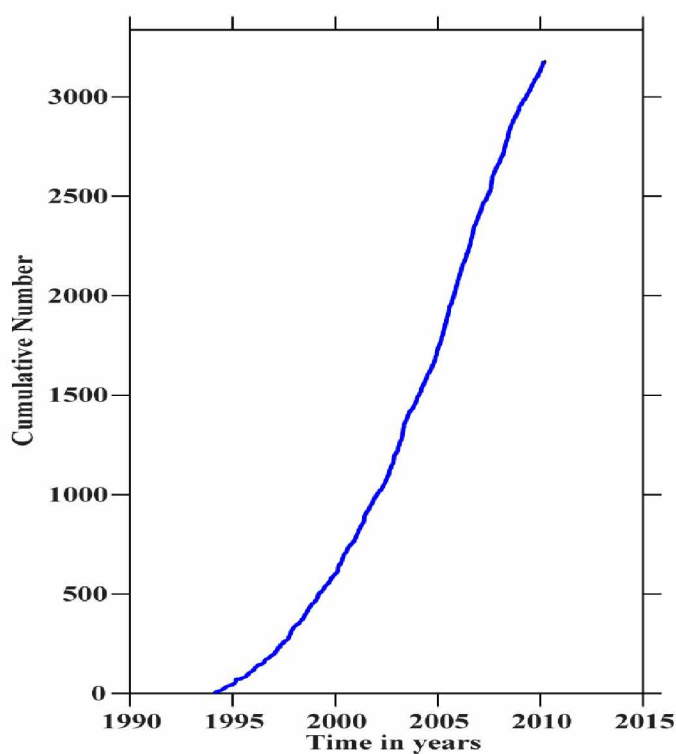

Figure C.2 Cumulative deep seismicity beneath Kilauea volcano from 1994-2010. Deep seismic events beneath Kilauea show no cyclic pattern as seen at the other volcanoes in this study. Instead, events have been occurring continuously over the last several years. Data courtesy of the Hawaiian Volcano Observatory.

While Vigneresse proposes a component of shear stress as an additional driving force for melt segregation, an alternate mechanism based on the patterns of seismicity which has been noted at the volcanoes in question as well as Mount Redoubt, Alaska is offered here. From the plot of seismicity in figure 3.2, it can be seen that the eruptions/unrest episodes at Mount Spurr are not preceded by large clusters of deep events nor do most of them occur during periods of heightened deep seismicity. The bulk of deep seismicity instead follows the eruptions; such a phenomenon was also seen at Mount Redoubt both associated with the 1989-1990 eruption sequence (Power et al., 1994) and following the 2009 eruption as well (see figure C.3).
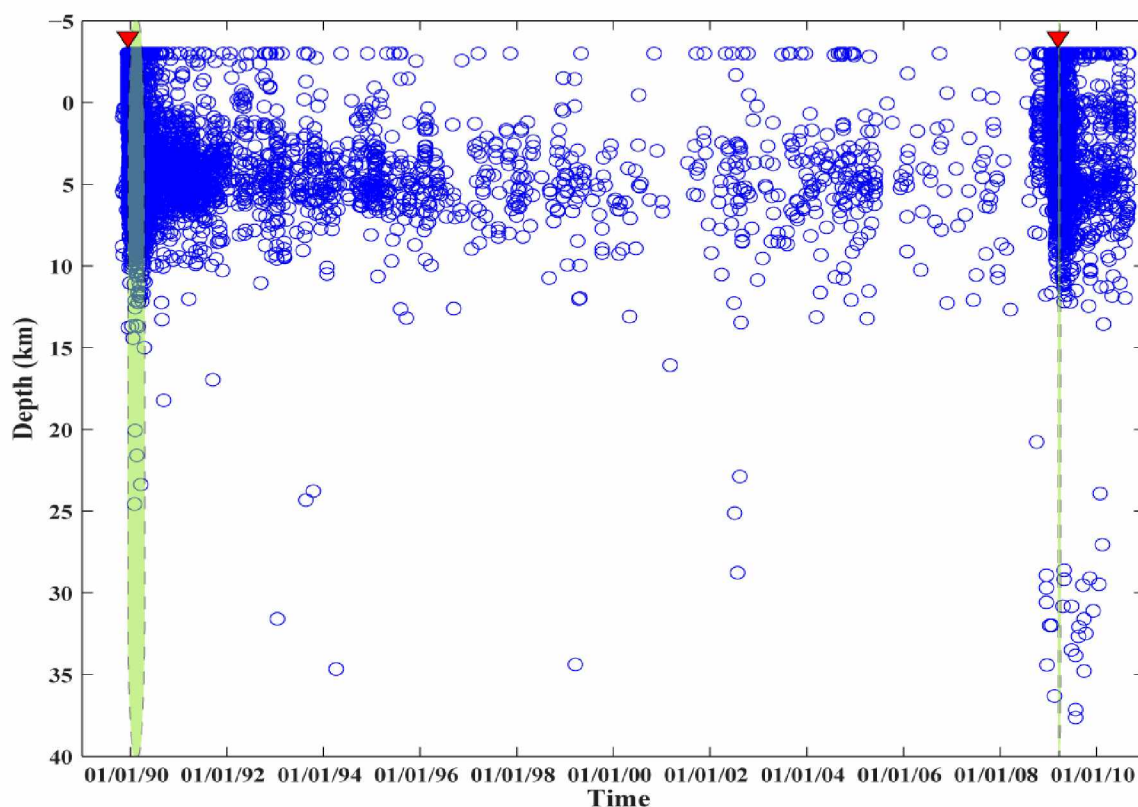

Figure C.3 Time-depth plot of seismicity within 10 km of Mount Redoubt, AK. Beneath this volcano, there are a sparse number of deep events the majority of which occur after the onset of explosive activity. Red triangles demark the onset of explosive eruptions in 1989 and 2009. Shaded region highlights the period of explosive activity during both eruptions.

During the 2004–2006 unrest episode at the summit vent of Mount Spurr, surface activity such as the generation of the ice cauldron and the increase in gas emission rates preceded the increase in deep seismic activity.

In this proposed mechanism, melt segregation at depth occurs as a result of pressure decreases induced by the removal of material from the shallow storage region during eruptions. During the periods between eruptions, movement of magma from the generation sites in the deep crust is controlled by deformational processes such as compaction and/or horizontal shear. The result of magma removal from the shallow system induces a change in the pressure regime of the magma transport akin to the draw down effect of pumping water in an aquifer. Progressive removal of material leads to deeper depths being exploited and allows for denser material to rise. The effect of this is new pulses of more mafic magma leaving their site of generation and traveling up through the crust to recharge the shallow magma chamber. Through this process, it is possible to move magma on time scales which are more in keeping with other lines of evidence offered by different studies in the regions of interest rather than the tens of thousands of years proposed by traditional melt segregation models (Annen et al., 2006). A schematic model for this process is shown in figure C.4.
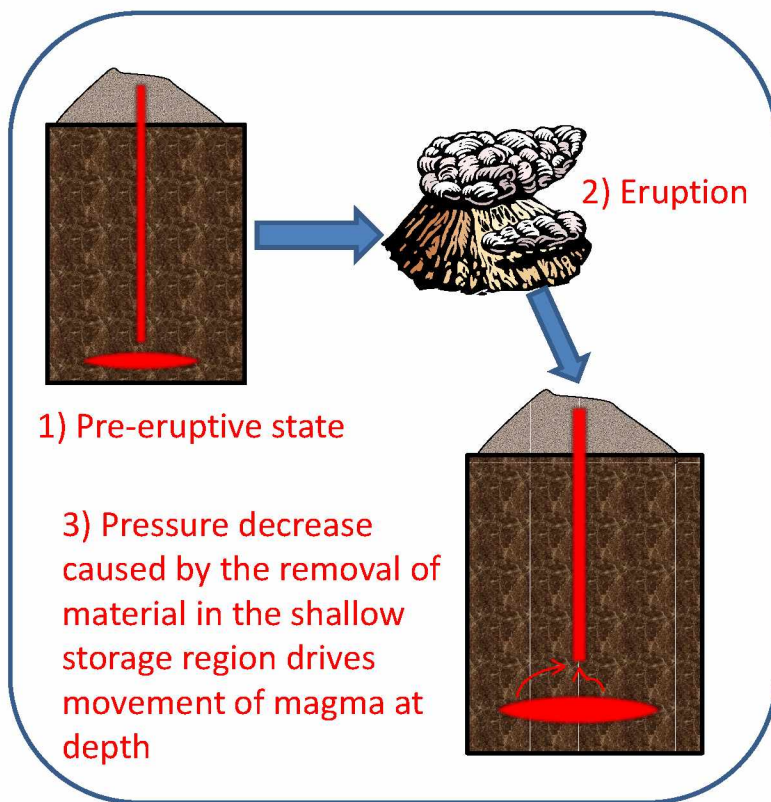
Figure C.4 A Schematic model for magma migration due to pressure variations. Prior to the removal of material during eruption, melt segregation occurs on time scales predicted by compaction and horizontal shear stress models. However, the removal of material during an eruption leads to a pressure decrease which induces flow from the deep storage events and the generation of deep seismic events.

For instance, analysis of plagioclase crystals from lavas erupted at Bezymianny volcano shows that while the crystal cores share a geochemical signature with those from the cataclysmic 1956 eruption, the rims show evidence for magma reheating by the injection of new mafic melt (Shcherbakov et al., in review). This recharge happens prior to each eruption of the volcano which occurs roughly twice per year. Geochemical analyses of lavas also show evidence of an increasing mafic trend. Geodetic surveys conducted as part of the PIRE project find no evidence of inflation prior to any of the eruptions at Bezymianny Volcano. Instead what is seen is a long term and long period

subsidence signal which, if of volcanic origin, reflects a tapping into a magma source in the deep crust (Freymueller, J, personal communication, 2009).

In other studies on deep seismicity, there has seldom been any positive correlation between deep seismic events and the onset of eruptive activity. In cases where a correlation has been made, a degree of ambiguity is also present. For example, one monochromatic event was recorded beneath Izu-Ooshima volcano in Japan about 1 year before its 1986 eruption (Ukawa and Ohtake, 1987). During the 1991 eruption of Mount Pinatubo in the Philippines, deep seismic events were found to correlate well with shallow activity (White, 1996). However, at the time that the volcano became instrumented, a vigorous swarm of shallow volcano tectonic (VT) events was already in progress as well as strong phreatic and fumarolic activity. This activity preceded the onset of deep seismicity by roughly one month beneath this volcano. Similarly, the 1989 unrest episode at Mammoth Mountain, CA, featured an intense swarm of shallow VT and LP events occurring several months before the onset of deep seismicity (Hill and Prejean, 2005).

Given the evidence provided by several different lines of study, it is therefore likely that the occurrence of deep seismic events beneath arc volcanoes reflects the processes associated with melt accumulation, segregation and ascent. Removal of material during eruptions provide an additional force which speeds up the process of melt segregation and introduces newer more mafic magma into the shallow storage region.

REFERENCES

Aki, K., and Koyanagi, R. (1981). Deep volcanic tremor and magma ascent mechanism under Kilauea, Hawaii. *Journal of Geophysical Research*, *86* (B8), 7095-7109.

Annen, C., Blundy, J., and Sparks, R. (2006). The genesis of intermediate and silicic magmas in deep crustal hot zones. *Journal of Petrology*, *47* (3), 505-539.

Blundy, J., Cashman, K., and Humphreys, M. (2006). Magma heating by decompression driven crystallization beneath andesite volcanoes. *Nature*, *443*, 76-80.

Buurman, H., and West, M. (2010). Seismic precursors to volcanic explosions during the 2006 eruption of Augustine Volcano. *In Press*.

Chouet, B. (1996). Long-period volcano seismicity: its source and use in eruption forecasting. *Nature*, *380*, 309-315.

Connolly, J., Holness, M., Rubie, D., and Rushmer, T. (1997). Reaction-induced microcracking: an experimental investigation of a mechanism for enchancing anatectic melt extraction. *Geology*, *25*, 591-594.

Coombs, M. L., Neal, C. A., Wessels, R. L., and McGimsey, R. G. (2006). Geothermal Disruption of Summit Glaciers at Mount Spurr Volcano, 2004-6: An Unusual Manifestation of Volcanic Unrest. *U.S. Geological Survey Professional Paper* (1732-B).

Davaille, A., and Lees, J. M. (2004). Thermal modeling of subducted plates: tear and hotspot at the Kamchatka corner. *Earth and Planetary Science Letters*, *226*, 293-304.

Dixon, J., Stihler, S., and Power, J. (2008). Catalog of earthquake hypocenters at Alaskan volcanoes: January 1 through December 31, 2007. *U.S. Geological Survey Data Series*, 73.

Fedatov, S., Zharinov, N., and Gontovaya, L. (2010). The Magmatic System of the Klyuchevskaya Group of Volcanoes. *Journal of Volcanology and Seismology*, *4* (1), 1-33.

Fehler, M. (1983). Observation of Volcanic Tremor at Mount St Helens Volcano. *Journal of Geophysical Research*, *88*, 3476-3484.

Gorelchick, V., and Storcheus, A. (2001). Deep long-period earthquakes beneath Klyuchevskoi volcano. In *Geodynamics and volcanism of the Kuril-Kamchatka*

island system (p. 428). Petropavlovsk-Kamchatsky, Kamchatka, Russia: IVGiG FEB RAs.

Hasegawa, A., Yamamoto, A., Zhao, D., Hori, S., and Horiuchi, A. (1993). Deep structure of arc volcanoes as inferred from seismic observations. *Philosophical Transactions: Physical Sciences and Engineering*, *342* (1663), 167-178.

Hill, D. (1976). Physical constraints on sounds generated by very small earthquakes. *EHRP Conference I, Abnormal animal behaviour prior to earthquakes*. NEHRP.

Hill, D., and Prejean, S. (2005). Magmatic unrest beneath Mammoth Mountain, California. *Journal of Volcanology and Geothermal Research*, *146*, 257-283.

Khubunaya, S., Gontovaya, L., Sobolev, A., and Nizkous, I. (2007). Magma Chambers beneath the Klyuchevskoy Volcanic Group. *Journal of Volcanology and Seismology*, *1* (2), 98-118.

Lay, T., and Wallace, T. (1995). *Modern Global Seismology*. San Diego, CA: Academic Press.

Lees, J., Symons, N., Chubarova, O., Gorelchik, V., and Ozerov, A. (2007). Tomographic Images of Kliuchevskoi Volcano P-wave Velocity. In J. Eichelberger, E. Gordeev, M. Kasahara, P. Izbekov, and J. M. Lees (Eds.), *Volcanism and Subduction: The Kamchatka Region* (pp. 293-302). Washington, D.C.: American Geophysical Union.

Levin, V., Shapiro, N., Park, J., and Ritzwoller, M. (2002). Seismic evidence for catastrophic slab loss beneath Kamchatka. *Letters to Nature*, *418*, 763-766.

Manea, V., and Manea, M. (2007). Thermal models beneath Kamchatka and the Pacific plate rejuvenation from a mantle plume impact. In J. Eichelberger, P. Izbekov, N. Ruppert, E. Gordeev, and J. Lees (Eds.), *Volcanism and Tectonics of the Kamchatka peninsula and adjacent arcs* (pp. 77-89). Washington, D.C.: AGU Monographs.

Miller, S., van der Zee, W., Olgaard, D., and Connolly, J. (2003). A fluid pressure feedback model of dehydration reactions: experiments, modelling and application to subduction zones. *Tectonophysics*, *370*, 241-251.

Mogi, K. (1962). Magnitude-Frequency Relation for Elastic Shocks Accompanying Fractures of Various Materials and Some Related Problems in Earthquakes. *Bulletin of the Earthquake Research Institute*, *40*, 831-853.

Neuberg, J., Luckett, R., Baptie, B., and Olsen, K. (2000). Models of tremor and low-frequency earthquake swarms on Montserrat. *Journal of Volcanology and Geothermal Research*, *101*, 83-104.

Nikulkin, A., Levin, V., Shuler, A., and West, M. (2010). Tectonic anomaly beneath the Klyuchevskoy Group: detached oceanic lithosphere? *In Press*.

Nye, C. J., and Turner, J. R. (1990). Petrology, geochemisty, and age of the Spurr volcanic complex, eastern Aleutian arc. *Bulletin of Volcanology*, *52*, 205-226.

Ohmi, S., Hirose, I., and Mori, J. (2004). Deep low-frequency earthquakes near the downward extension of the seismogenic fault of the 2000 Western Tottori earthquake. *Earth Planets Space*, *56*, 1185-1189.

Pavlis, G., Vernon, F., Harvey, D., and Quinlan, D. (2004). The generalized earthquake location (GENLOC) package: an earthquake location library. *Computers & Geosciences*, *30*, 1079-1091.

Portnyagin, M., Hoernle, K., Avdeiko, G., Hauff, F., Werner, R., Bindeman, I., et al. (2005). Transition from arc to oceanic magmatism at the Kamchatka-Aleutian junction. *Geology*, *33*(1), 25-28.

Power, J., Lahr, J., Page, R., and Chouet, B. (1994). Seismic evolution of the 1989-1990 eruption sequence of Redoubt. *Jouynal of Volcanology and Geothermal Research*, *62*(1-4), 69-94.

Power, J., Stihler, S., White, R., and Moran, S. (2004). Observations of deep long-period (DLP) seismic events beneath Aleutian arc volcanoes; 1989-2002. *Journal of Volcanology and Geothermal Research*, *134*, 243-266.

Scholz, C. (1968). The Frequency-Magnitude Relation of Microfractures in Rock and its Relation to Earthquakes. *Bulletin of the Seismological Society of America*, *58*(1), 399-415.

Senyukov, S., and Droznina, S. (2009). Preliminary 1-D velocity model of Bezymianny Volcano (Kamchatka, Russia), USA-PIRE project. *JKASP Conference*. Fairbanks, AK.

Senyukov, S., Drozinina, S. Y., Nuzhdina, I., Garbuzova, V., and Kozhevnikova, T. (2009). Studies in the activity of Klyuchevskoy Volcano by remote sensing Techniques between January 1, 2001 and July 31, 2005. *Journal of Volcanology and Seismology*, *3*(3), 191-199.

Shcherbakov, V., Plechov, P. Y., Izbekov, P., and Shipman, J. (In review). Plagioclase zoning as an indicator of magma processes at Bezymianny Volcanao Kamchatka. *Contributions to Mineralogy and Pertrology*.

Shearer, P. M. (1997). Improving local earthquake location using the L1 norm and waveform cross correlation: Application to the Whittier Narrows, California, aftershock sequence. *Journal of Geophysical Research*, *102* (B4), 8269-8283.

Thelen, W., West, M., and Senyukov, S. (2010). Seismic characterization of the fall 2007 eruptive sequence at Bezymianny Volcano, Russia. *Journal of Volcanology and Geothermal Research*, *194* (4), 201-213.

Ukawa, M., and Ohtake, M. (1987). A Monochromatic Earthquake Suggesting Deep-Seated Magmatic Activity Beneath the Izu-Ooshima Volcano, Japan. *Journal of Geophysical Research*, *92* (B12), 12,649 - 12,663.

Vigneresse, J. (1995). Control of granite emplacement by regional deformation. *Tectonophysics*, *249*, 173-186.

Vigneresse, J. (2004). Toward a new paradigm for granite generation. *Transactions of the Royal Society of Edinburgh: Earth Sciences*, *95*, 11-22.

Waldhauser, F., and Ellsworth, W. (2000). A Double-Difference Earthquake Location Algorithm: Method and Application to the Northern Hayward Fault, California. *Bullletin of the Seismological Society of America*, 1353-1368.

White, R. (1996). Precursory Deep Long-Period Earthquakes at Mount Pinatubo: Spatio-Temporal Link to a Basalt Trigger. In C. Newhall, and R. Punongbayan (Eds.), *FIRE and MUD: Eruptions and Lahars of Mount Pinatubo, Philippines.* Seattle: University of Washington Press.

Wiemer, S., and McNutt, S. (1997). Variations in the frequency-magnitude distribution with depth in two volcanic areas: Mount St. Helens, Washington, and Mt. Spurr, Alaska. *Geophysical Research Letters*, *24* (2), 189-192.

Wolfe, C., Okubo, P., Nettles, M., Ekstrom, G., and Shearer, P. (2004). Characteristics of deep (13 km) Hawaiian earthquakes and Hawaiian earthquakes west of 155.5 W. *Geochemistry Geophysics Geosystems*, *5* (4), 1-28.